Title	Many-variable variational Monte-Carlo study of unconventional superconductivity in multiband systems
Author(s)	加藤, 大智
Citation	大阪大学, 2020, 博士論文
Version Type	VoR
URL	https://doi.org/10.18910/76366
rights	
Note	

Doctoral Thesis

Many-variable variational Monte-Carlo study of unconventional superconductivity in multiband systems

Department of Physics, Osaka University

Daichi Kato

February 25, 2020

Contents

1 Introduction

1.1 Superconductivity

Superconductors exhibit zero resistivity and magnetic field shielding below the superconducting critical temperature T_c. Superconductors can be applied to electric wires and superconducting maglevs, power storage devices, and so on. However, industrial applications are restricted within narrow limits due to the low T_c compared with room temperature. For example, the cuprates have the highest T_c of 133 K at ambient pressure [1] (see Fig. 1.1). Hence high-temperature superconductivity and its mechanism have been studied intensively for long years.

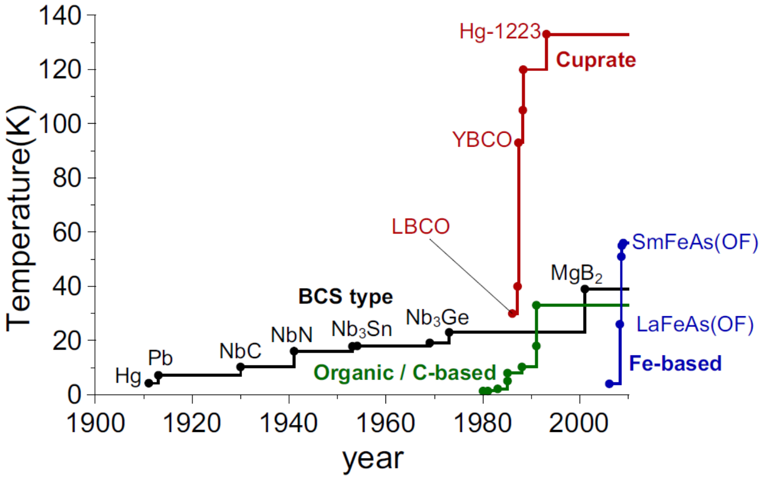

Fig. 1.1: A timeline of the superconducting transition temperature of major families of superconductors at ambient pressure. Black points indicate the conventional BCS-type superconductors, red the cuprates, blue the iron-based, and green the organic. This figure is taken from Ref. [2].

The BCS theory revealed the following mechanism of superconductivity [3]:

1. Two electron forms one boson, called Cooper pair, due to an attractive interaction between electrons mediated by phonons.
2. The condensation of Cooper pairs causes superconductivity at low temperature.

Further, the pairing glue has the energy and momentum dependence in general.From the BCS theory, T_c of the phonon-mediated s-wave (BCS-type) pairing is given by

$$k_B T_c = 1.13\omega_D \exp(-1/\lambda), \tag{1.1.1}$$

where ω_D denotes the Debye frequency which determines the energy window of phonon frequencies near the Fermi energy E_F ($|\omega - E_F| \leq \omega_D$). λ is the electron-phonon coupling. This T_c formula tells us that as the electron-phonon coupling λ increases, T_c increases rapidly. However, T_c is suppressed by strong renormalization as follows [4]:

$$\lambda \to \lambda/(1+\lambda). \tag{1.1.2}$$

Therefore, the upper limit of T_c of BCS-type superconductors had been estimated to be about 10% of the Debye temperature, i.e. about 10 K. In the occurrence of superconductivity in general, there is a trade-off relation between strong pairing interactions and weak renormalization: Strong pairing interaction, which itself enhances pairing, usually increases renormalization simultaneously, giving rise to suppression of T_c. Quite recently, the energy dependence of the pairing glue and renormalization effect has been considered to be key factors for enhancing T_c (see section 3).

Amazingly, the BCS-type superconductivity above 200 K has been discovered in several hydrides under high pressure [5–7]. The possibility of high-temperature conventional superconductivity in hydrides has been pointed out since early days after the proposal of the BCS theory. As is shown in Eq. (1.1.1), the T_c is proportional to the Debye frequency, which can be proportional to the inverse of the square of mass. Thus, metallic hydrides under high pressure are expected to exhibit extremely high T_c [8]. It is notable that these discoveries have been motivated by first-principles calculations of the pressure dependency of crystal structures and T_c [9,10]. First-principles calculations can filter out the case for the weak electron-phonon coupling λ, where T_c should be low even when the Debye frequency is very high. In this way, the combination of the experiment and theory can make a breakthrough in the research of superconductivity. If the same is possible in purely electronic systems, room-temperature superconductors can be discovered even at ambient pressure since the energy scale of bare electrons ($\sim$ 1 eV) is much larger than the room temperature. To achieve this, we have to reveal the mechanism of the non-BCS type (unconventional) superconductivity.

1.2 Spin-fluctuation mediated superconductivity

The spin-fluctuation mediated pairing is one of leading candidates for the mechanism of high-temperature superconductivity; namely, cuprates [11] and iron-based superconductors [12]. Around a magnetic phase transition, such as paramagnetic (PM) phase to antiferromagnetic (AFM) or ferromagnetic (FM), spin density wave (SDW) phases, there are no long-range spin orders but spin fluctuations, which can mediate the pairing similarly to phonons (e.g. Refs. [13, 14]). The Fermi surface nesting is crucial for the occurrence of spin-fluctuation mediated superconductivity (see section 2.5). The Fermi surface nesting means that two pieces of Fermi surfaces are connected with each other via a certain wave vector (nesting vector $\boldsymbol{Q}$).

Next, we briefly review the basic properties of the high-temperature superconductors and show the possible spin-fluctuation mediated pairing in these materials.

1.3 Cuprates

The basic properties of cuprates are as follows:

1. The mother compounds are antiferromagnetic (AFM) Mott insulators, which is the insulating state caused by the strong correlation effect (see section 2.2).
2. By carrier doping, cuprates exhibit $d_{x^2-y^2}$-wave spin-singlet superconductivity.
3. Cuprates possess a layered crystal structure composed of a stacking of blocking layers and conduction (superconducting) layers, quasi-two-dimensional $\mathrm{CuO_2}$ planes.
4. Carriers are doped from blocking layers to conduction layers.
5. The role of phonons for pairings should not be so crucial as much as that in the BCS theory.
6. In the low-doping region close to the Mott phase, a finite-energy gap is observed even above T_{c}, which is called the pseudogap.

Cuprates are approximated as two-dimensional systems with strongly hybridizing Cu-$3d$ and O-$2p$ orbitals. In hole-doped cuprates, the Cu ions are surrounded by an octahedron of oxygens as in a perovskite structure. On the other hand, in electron-doped cuprates, apical oxygens are absent. Due to the crystal field effect, Cu-$3d$ orbitals are split into two-fold degenerate e_g orbitals $(d_{x^2-y^2}, d_{z^2})$ and three-fold degenerate t_{2g} orbitals (d_{xy}, d_{yz}, d_{zx}). In most of cuprates, the perovskite structure is briefly extended in the interlayer direction, so that the $d_{x^2-y^2}$ energy level is higher than that of d_{z^2}. In the mother compounds, Cu ion possesses nine $3d$ electrons and the $d_{x^2-y^2}$ orbital is nearly half-filled. The band near the Fermi level and Fermi surface are mainly originating from the $d_{x^2-y^2}$ orbitals (see Fig. 1.3).

As is shown in Fig. 1.2, mother compounds of the cuprates are AFM Mott insulators, so that the strong AFM correlation persists even in the carrier doped superconducting states. In addition, according to a t-J model, which is the model of correlated electron systems in the limit of strong correlation, the pairing can arise from the superexchange interaction. There are no qualitative differences between these two hypotheses since both of them describes the pairing glue made from the AFM fluctuation of spin degrees of freedom.

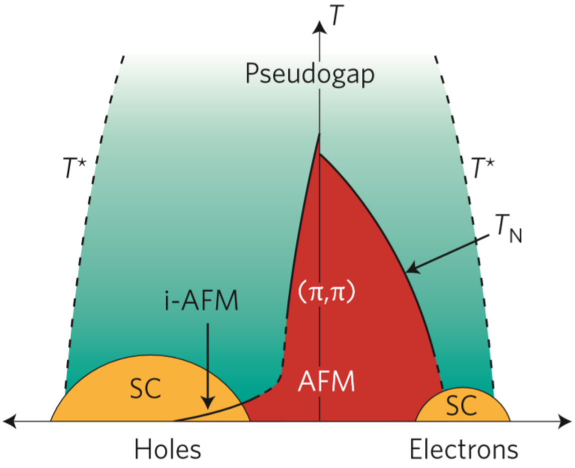

Fig. 1.2: Schematic phase diagram of the cuprates on electron- or hole- doping. This figure is taken from Ref. [15].

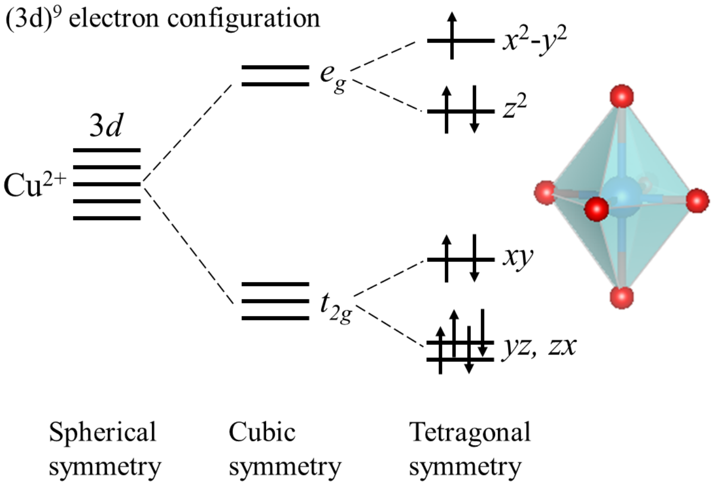

Fig. 1.3: Jahn-Teller effect on CuO_6 in the cuprates and perovskite structure. To plot the crystal structure, the VESTA software [16] is used throughout the present thesis.

1.4 Iron-based superconductors

The basic properties of iron-based superconductors are as follows:

1. The mother compounds are AFM metallic (SDW) state.
2. By carrier doping, iron-based superconductors exhibit spin-singlet superconductivity.

3. Iron-based superconductors possess a layered crystal structure composed of a stacking of blocking layers and conduction (superconducting) layers, quasi-two-dimensional Fe-Anion layers.

4. Carriers are doped from blocking layers to conduction layers.

5. The role of phonons for pairings should not be so crucial as much as that in the BCS theory.

The basic properties are very similar to those of cuprates. The iron-based superconductors are approximated as strongly correlated two-dimensional electron systems with Fe-$3d$ orbitals [17]. Due to the crystal field effect, Fe-$3d$ orbitals are split into two-fold degenerate e_g orbitals $(d_{x^2-y^2}, d_{z^2})$ and three-fold degenerate t_{2g} orbitals (d_{xy}, d_{yz}, d_{zx}). The energy levels of e_g and t_{2g} orbitals are opposite to those of cuprates since anions are located at the center of the square of Fe ions (see Fig. 1.5). In the mother compounds, Fe ion possesses six $3d$ electrons. The band near the Fermi level and Fermi surface are mainly originating from the d_{xy}, d_{yz}, d_{zx} orbitals. In addition, the slightly three-dimensionality of the bands is attributed to the d_{z^2} orbital (see Fig. 1.6).

The iron-based superconductors are multi-orbital systems with spin-orbital interplay. In the low-doping region, the SDW phase appears, and the tetragonal-to-orthorhombic structural transition takes place at a temperature above the Néel temperature T_N (see Fig. 1.4). In the orthorhombic phase, the discrete lattice rotational symmetry is broken by the orbital nematic order by making the symmetry between the x and y directions in the iron plane non-equivalent. By carrier doping, the superconducting phase is realized near the SDW and nematic phases. Additional superconducting domes in very high hole- or electron- doping region have also been reported.

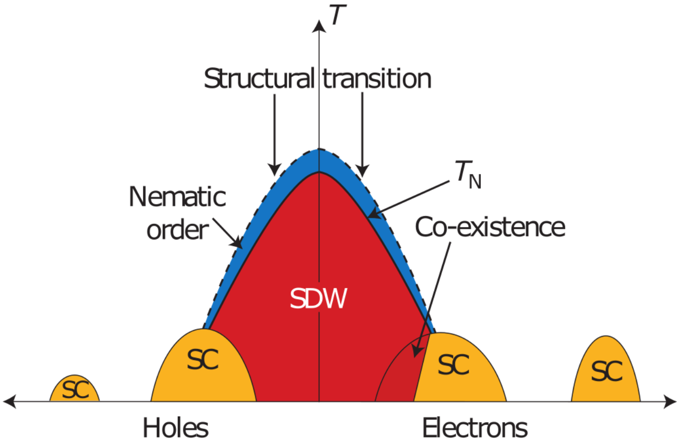

Fig. 1.4: Schematic phase diagram of the iron-based superconductors on electron- or hole- doping. This figure is taken from Ref. [15].

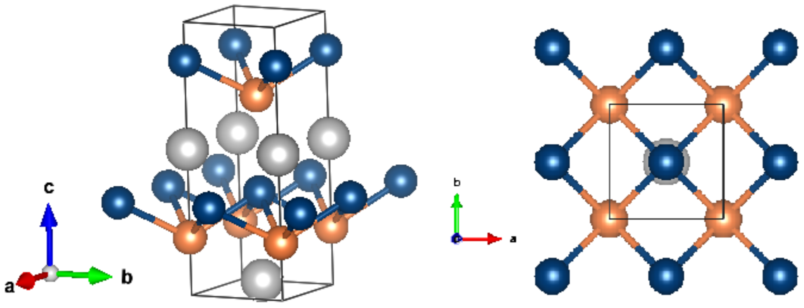

Fig. 1.5: Lattice structure of LiFeAs. Orange and blue, gray balls denote Fe and As, Li ions, respectively.

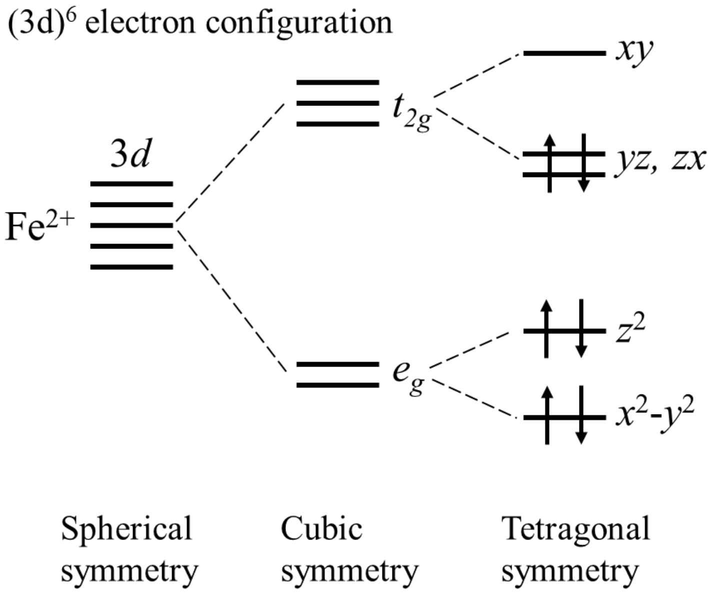

Fig. 1.6: Jahn-Teller effect on the Fe-Anion layers in the iron-based superconductors.

1.5 Superconductors with incipient bands

In the early days of the study of the iron-based superconductors, it was considered that the nesting between the electron and hole Fermi surfaces, combined with Hubbard U, induces the spin-fluctuation mediated pairing [17–22]. However, the spin-fluctuation theory is challenged by discoveries of (heavily) electron-doped iron-based superconductors with a relatively high $T_{\rm c}$ where hole-like bands are away from, but still close to the Fermi level leaving the only electron Fermi surface as shown in Fig. 1.8 [23–34]. Naively, removing hole Fermi surfaces should destroy the spin-fluctuation-mediated pairing and suppress $T_{\rm c}$ rapidly. After the observations, a role of "incipient bands", which do not intersect, but sit close to the Fermi level, have received much attention (see Figs. 1.7 and 1.8). Various authors have suggested that the spin-fluctuation scattering of pairs between an electron Fermi surface and an incipient hole band can induce pairing [18,31,33,35–40]. We will come back to this topic in section 3.

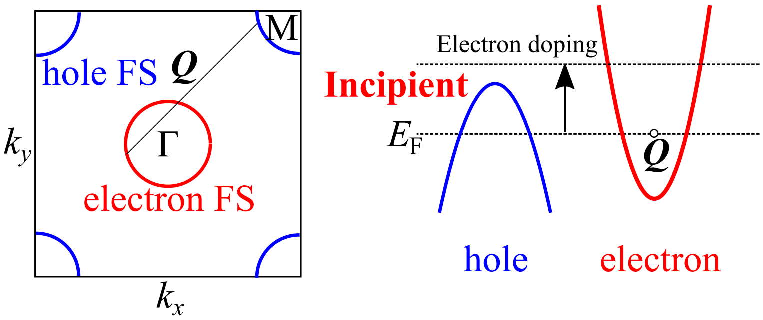

Fig. 1.7: Typical Fermi surface and band structure of iron-based superconductors with an incipient band. The arrow denotes the nesting vector $\boldsymbol{Q} = (\pi, 0)$.

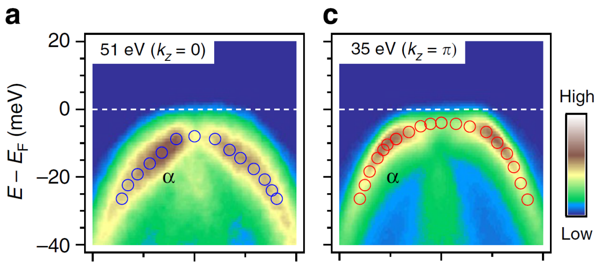

Fig. 1.8: Band dispersion of a band at $k_z = 0$ and π in LiFe$_{0.97}$Co$_{0.03}$As. (a,c) show the ARPES intensity plots of LiFe$_{0.97}$Co$_{0.03}$As at 51 eV ($k_z = 0$) and 35 eV ($k_z = p$), respectively. The data are recorded at 20 K with linearly polarized light to enhance the a band. This figure is taken from Ref. [31].

2 Basic concepts on the theory of superconductivity

In this section, we explain the basic concepts on the theory of superconductivity. Firstly, we derive the BCS wave function and the $T_{\rm c}$ formula by relying on the BCS theory. Secondary, we introduce the way to study strongly correlated electron systems, such as high-temperature superconductors. Thirdly, we briefly explain a perturbation theory, which describes the possible pairing mechanism of those unconventional superconductors.

2.1 BCS theory

The BCS theory revealed the wave functions which describe superconducting ground states incorporating non-perturbative many-body effects. To derive the BCS wave function, we consider the reduced Hamiltonian for many electron systems [3, 41]

$$\hat{H}_{\rm red} = \sum_{\boldsymbol{k}} \sum_{1} \xi_1(\boldsymbol{k}) c^\dagger_{\boldsymbol{k},1} c_{\boldsymbol{k},1} + \sum_{\boldsymbol{k},\boldsymbol{k}'} \sum_{1,2,3,4} V_{1,2;3,4}(\boldsymbol{k},\boldsymbol{k}') c^\dagger_{-\boldsymbol{k},1} c^\dagger_{\boldsymbol{k},2} c_{\boldsymbol{k}',3} c_{-\boldsymbol{k}',4}, \tag{2.1.1}$$

Here $c^\dagger_{\boldsymbol{k}m}/c_{\boldsymbol{k}m}$ creates/annihilates a fermion with momentum $\boldsymbol{k}$ and index $m(=1,2,3,4)$, which denotes an internal degree of freedom, such as spin and orbital. $\xi_1(\boldsymbol{k})$ is the band energy measured relative to the chemical potential μ and the operator $\hat{V}$ is a general effective electron-electron interaction. The quantity $V_{1,2;3,4}(\boldsymbol{k},\boldsymbol{k}')$ denotes the matrix element

$$V_{1,2;3,4}(\boldsymbol{k},\boldsymbol{k}') \equiv \langle -\boldsymbol{k},1;\boldsymbol{k},2|\hat{V}|-\boldsymbol{k}',4;\boldsymbol{k}',3\rangle = \langle 0|c_{\boldsymbol{k},2}c_{-\boldsymbol{k},1}\hat{V}c^\dagger_{-\boldsymbol{k}',4}c^\dagger_{\boldsymbol{k}',3}|0\rangle, \tag{2.1.2}$$

From the anti-commutation relation of fermions, the following symmetries are given by

$$V_{1,2;3,4}(\boldsymbol{k},\boldsymbol{k}') = -V_{2,1;3,4}(-\boldsymbol{k},\boldsymbol{k}') = -V_{1,2;4,3}(-\boldsymbol{k},-\boldsymbol{k}') = V_{3,4;1,2}(\boldsymbol{k},\boldsymbol{k}'). \tag{2.1.3}$$

Let us consider the superconducting state in the single orbital system without the external field ($\xi_\uparrow(\boldsymbol{k}) = \xi_\downarrow(\boldsymbol{k}) = \xi(\boldsymbol{k})$). The reduced Hamiltonian (Eq. (2.1.1)) is then rewritten as

$$\hat{H}_{\rm red} = \sum_{\sigma} \sum_{\boldsymbol{k}} \xi(\boldsymbol{k}) c^\dagger_{\boldsymbol{k}\sigma} c_{\boldsymbol{k}\sigma} + \sum_{\sigma_1,\sigma_2,\sigma_3,\sigma_4} \sum_{\boldsymbol{k},\boldsymbol{k}'} V_{\sigma_1,\sigma_2;\sigma_3,\sigma_4}(\boldsymbol{k},\boldsymbol{k}') c^\dagger_{-\boldsymbol{k}\sigma_1} c^\dagger_{\boldsymbol{k}\sigma_2} c_{\boldsymbol{k}'\sigma_3} c_{-\boldsymbol{k}'\sigma_4}. \tag{2.1.4}$$

To proceed, we perform the usual mean-field decoupling of the quartic term:

$$\begin{aligned} c^\dagger_{-\boldsymbol{k}\sigma_1} c^\dagger_{\boldsymbol{k}\sigma_2} c_{\boldsymbol{k}'\sigma_3} c_{-\boldsymbol{k}'\sigma_4} \approx \langle c^\dagger_{-\boldsymbol{k}\sigma_1} c^\dagger_{\boldsymbol{k}\sigma_2}\rangle c_{\boldsymbol{k}'\sigma_3} c_{-\boldsymbol{k}'\sigma_4} + \langle c_{\boldsymbol{k}'\sigma_3} c_{-\boldsymbol{k}'\sigma_4}\rangle c^\dagger_{-\boldsymbol{k}\sigma_1} c^\dagger_{\boldsymbol{k}\sigma_2} \\ + \langle c^\dagger_{-\boldsymbol{k}\sigma_1} c^\dagger_{\boldsymbol{k}\sigma_2}\rangle \langle c_{\boldsymbol{k}'\sigma_3} c_{-\boldsymbol{k}'\sigma_4}\rangle. \end{aligned} \tag{2.1.5}$$

where $\sigma_i (i = 1, 2, 3, 4)$ denote spins of electrons. The nonzero $\langle c^\dagger_{-\boldsymbol{k}\sigma_1} c^\dagger_{\boldsymbol{k}\sigma_2} \rangle$ corresponds to one Cooper pair in the superconducting state. Then, we define the gap function:

$$\Delta_{\sigma_1,\sigma_2}(\boldsymbol{k}) = -\sum_{\sigma_3,\sigma_4} \sum_{\boldsymbol{k}'} V_{\sigma_2,\sigma_1;\sigma_3,\sigma_4}(\boldsymbol{k}, \boldsymbol{k}') \langle c_{\boldsymbol{k}'\sigma_3} c_{-\boldsymbol{k}'\sigma_4} \rangle. \tag{2.1.6}$$

Using Eq. (2.1.3), the Hermitian conjugate is given by

$$\Delta^*_{\sigma_1,\sigma_2}(-\boldsymbol{k}) = \sum_{\sigma_3,\sigma_4} \sum_{\boldsymbol{k}'} V_{\sigma_3,\sigma_4;\sigma_2,\sigma_1}(\boldsymbol{k}, \boldsymbol{k}') \langle c^\dagger_{-\boldsymbol{k}'\sigma_3} c^\dagger_{\boldsymbol{k}'\sigma_4} \rangle. \tag{2.1.7}$$

By definition, the gap function has the symmetry

$$\Delta_{\sigma_2,\sigma_1}(-\boldsymbol{k}) = -\Delta_{\sigma_1,\sigma_2}(\boldsymbol{k}). \tag{2.1.8}$$

Eqs. (2.1.5) and (2.1.6), (2.1.7), (2.1.4), (2.1.3) yield the BCS Hamiltonian:

$$\hat{H}_{\mathrm{BCS}} = \sum_\sigma \sum_{\boldsymbol{k}} \xi(\boldsymbol{k}) c^\dagger_{\boldsymbol{k}\sigma} c_{\boldsymbol{k}\sigma} + \sum_{\sigma_1,\sigma_2} \sum_{\boldsymbol{k}} \left(\Delta_{\sigma_1,\sigma_2}(\boldsymbol{k}) c^\dagger_{\boldsymbol{k}\sigma_1} c^\dagger_{-\boldsymbol{k}\sigma_2} - \Delta^*_{\sigma_1,\sigma_2}(-\boldsymbol{k}) c_{-\boldsymbol{k}\sigma_1} c_{\boldsymbol{k}\sigma_2} \right). \tag{2.1.9}$$

Here we omitted one term containing only the mean field but no operators, since it gives only a contribution to the ground state energy. Using Eq. (2.1.8), the Hamiltonian matrix is given by

$$\begin{aligned} \hat{H}_{\mathrm{BCS}} = \sum_{\boldsymbol{k}} & \left(c^\dagger_{\boldsymbol{k}\uparrow}, c^\dagger_{\boldsymbol{k}\downarrow}, c_{-\boldsymbol{k}\uparrow}, c_{-\boldsymbol{k}\downarrow} \right) \\ & \times \begin{pmatrix} \xi(\boldsymbol{k}) & 0 & \Delta_{\uparrow\uparrow}(\boldsymbol{k}) & \Delta_{\uparrow\downarrow}(\boldsymbol{k}) \\ 0 & \xi(\boldsymbol{k}) & \Delta_{\downarrow\uparrow}(\boldsymbol{k}) & \Delta_{\downarrow\downarrow}(\boldsymbol{k}) \\ \Delta^*_{\uparrow\uparrow}(\boldsymbol{k}) & \Delta^*_{\downarrow\uparrow}(\boldsymbol{k}) & -\xi(-\boldsymbol{k}) & 0 \\ \Delta^*_{\uparrow\downarrow}(\boldsymbol{k}) & \Delta^*_{\downarrow\downarrow}(\boldsymbol{k}) & 0 & -\xi(-\boldsymbol{k}) \end{pmatrix} \begin{pmatrix} c_{\boldsymbol{k}\uparrow} \\ c_{\boldsymbol{k}\downarrow} \\ c^\dagger_{-\boldsymbol{k}\uparrow} \\ c^\dagger_{-\boldsymbol{k}\downarrow} \end{pmatrix}. \end{aligned} \tag{2.1.10}$$

This effective one-particle Hamiltonian can be easily diagonalized using a unitary Bogoliubov-Valatin transformation,

$$c_{\boldsymbol{k}\sigma} = \sum_{\sigma'} \left(u_{\boldsymbol{k}\sigma\sigma'} \gamma_{\boldsymbol{k}\sigma'} + v_{\boldsymbol{k}\sigma\sigma'} \gamma^\dagger_{-\boldsymbol{k}\sigma'} \right). \tag{2.1.11}$$

The new operators $\gamma^{(\dagger)}_{\boldsymbol{k}\sigma}$ satisfy the anti-communication relations of fermions and generate the elementary excitations (quasi-particles) of the system. We use a four-component notation,

$$\boldsymbol{c}^{\mathrm{T}}_{\boldsymbol{k}} = \left(c_{\boldsymbol{k}\uparrow}, c_{\boldsymbol{k}\downarrow}, c^\dagger_{-\boldsymbol{k}\uparrow}, c^\dagger_{-\boldsymbol{k}\downarrow} \right)^{\mathrm{T}}, \tag{2.1.12}$$

$$\boldsymbol{\gamma}^{\mathrm{T}}_{\boldsymbol{k}} = \left(\gamma_{\boldsymbol{k}\uparrow}, \gamma_{\boldsymbol{k}\downarrow}, \gamma^\dagger_{-\boldsymbol{k}\uparrow}, \gamma^\dagger_{-\boldsymbol{k}\downarrow} \right)^{\mathrm{T}}, \tag{2.1.13}$$

which gives a more compact formulation of Eq. (2.1.11): $\boldsymbol{c}_{\boldsymbol{k}} = U_{\boldsymbol{k}}\boldsymbol{\gamma}_{\boldsymbol{k}}$ with

$$U_{\boldsymbol{k}} = \begin{pmatrix} \hat{u}_{\boldsymbol{k}} & \hat{v}_{\boldsymbol{k}} \\ \hat{v}^*_{-\boldsymbol{k}} & \hat{u}^*_{-\boldsymbol{k}} \end{pmatrix} \quad \text{and} \quad U_{\boldsymbol{k}}U^\dagger_{\boldsymbol{k}} = 1, \tag{2.1.14}$$

where the second equation is the unitary condition of the transformation. The 2x2 matrices $\hat{u}_{\boldsymbol{k}}$ and $\hat{v}_{\boldsymbol{k}}$ are defined by Eq. (2.1.11). Using this formalism, diagonalization of $\hat{H}_{\mathrm{BCS}}$ is written as

$$\hat{E}_{\boldsymbol{k}} = U^\dagger_{\boldsymbol{k}}\hat{\mathcal{E}}_{\boldsymbol{k}}U_{\boldsymbol{k}}, \tag{2.1.15}$$

where we use the 4x4 matrices

$$\hat{E}_{\boldsymbol{k}} = \begin{pmatrix} E_{\boldsymbol{k}\uparrow} & 0 & 0 & 0 \\ 0 & E_{\boldsymbol{k}\downarrow} & 0 & 0 \\ 0 & 0 & -E_{-\boldsymbol{k}\uparrow} & 0 \\ 0 & 0 & 0 & -E_{-\boldsymbol{k}\downarrow} \end{pmatrix}, \tag{2.1.16}$$

and

$$\hat{\mathcal{E}}_{\boldsymbol{k}} = \begin{pmatrix} \xi(\boldsymbol{k})\hat{\sigma}_0 & \hat{\Delta}(\boldsymbol{k}) \\ \hat{\Delta}^{*\mathrm{T}}(\boldsymbol{k}) & -\xi(-\boldsymbol{k})\hat{\sigma}_0 \end{pmatrix}. \tag{2.1.17}$$

The diagonal elements of $\hat{\mathcal{E}}_{\boldsymbol{k}}$ correspond to the excitation spectrum of the system, and $\hat{\mathcal{E}}_{\boldsymbol{k}}$ is the representation of $\hat{H}_{\mathrm{BCS}}$, where 2x2 matrix $\hat{\sigma}_0$ is the 2x2 unit matrix and the matrix $\hat{\Delta}(\boldsymbol{k})$ is defined in Eq. (2.1.10). Let us find the transformation $U_{\boldsymbol{k}}$ for the spin-singlet pairing. For the singlet pairing, the gap function has to be an even function of $\boldsymbol{k}$. Therefore, $\hat{\Delta}(\boldsymbol{k})$ is an antisymmetric matrix which can be described by a single even function $\Delta_{\mathrm{SC}}(\boldsymbol{k})$,

$$\hat{\Delta}(\boldsymbol{k}) = i\hat{\sigma}_y\Delta_{\mathrm{SC}}(\boldsymbol{k}) = \begin{pmatrix} 0 & \Delta_{\mathrm{SC}}(\boldsymbol{k}) \\ -\Delta_{\mathrm{SC}}(\boldsymbol{k}) & 0 \end{pmatrix}. \tag{2.1.18}$$

The BCS Hamiltonian is then rewritten as

$$\hat{H}_{\mathrm{BCS}} = \sum_\sigma\sum_{\boldsymbol{k}} \left(c^\dagger_{\boldsymbol{k}\sigma}, c_{-\boldsymbol{k}\overline{\sigma}}\right) \begin{pmatrix} \xi(\boldsymbol{k}) & \sigma\Delta_{\mathrm{SC}}(\boldsymbol{k}) \\ \sigma\Delta_{\mathrm{SC}}(\boldsymbol{k}) & -\xi(-\boldsymbol{k}) \end{pmatrix} \begin{pmatrix} c_{\boldsymbol{k}\sigma} \\ c^\dagger_{-\boldsymbol{k}\overline{\sigma}} \end{pmatrix} \quad (\overline{\sigma} = -\sigma). \tag{2.1.19}$$

The Bogoliubov-Valatin transformation is given by

$$\gamma_{\boldsymbol{k}\sigma} = u_{\boldsymbol{k}}c_{\boldsymbol{k}\sigma} - \sigma v_{\boldsymbol{k}}c^\dagger_{-\boldsymbol{k}\overline{\sigma}}, \tag{2.1.20}$$

$$\gamma^\dagger_{-\boldsymbol{k}\overline{\sigma}} = \sigma v_{\boldsymbol{k}}c_{\boldsymbol{k}\sigma} + u_{\boldsymbol{k}}c^\dagger_{-\boldsymbol{k}\overline{\sigma}}, \tag{2.1.21}$$

with

$$u^2_{\boldsymbol{k}} = \frac{1}{2}\left(1 + \frac{\xi(\boldsymbol{k})}{E(\boldsymbol{k})}\right), \tag{2.1.22}$$

$$v^2_{\boldsymbol{k}} = \frac{1}{2}\left(1 - \frac{\xi(\boldsymbol{k})}{E(\boldsymbol{k})}\right), \tag{2.1.23}$$

$$u_{\boldsymbol{k}}v_{\boldsymbol{k}} = \frac{\Delta_{\mathrm{SC}}(\boldsymbol{k})}{2E(\boldsymbol{k})}, \tag{2.1.24}$$

$$E(\boldsymbol{k}) = \left[\xi(\boldsymbol{k})^2 + \Delta_{\mathrm{SC}}(\boldsymbol{k})^2\right]^{1/2}, \tag{2.1.25}$$

where $u_{\boldsymbol{k}}$ and $v_{\boldsymbol{k}}$ are assumed to be real and even functions for $\boldsymbol{k}$.

After diagonalizing $\hat{H}_{\mathrm{BCS}}$, the superconducting ground state is obtained by creating all negative energy states and annihilating all positive energy states on the vacuum state as follows,

$$|\phi_{\mathrm{BCS}}\rangle = \prod_{\boldsymbol{k}} \gamma_{\boldsymbol{k}\uparrow}\gamma_{-\boldsymbol{k}\downarrow}|0\rangle \tag{2.1.26}$$

$$\propto \prod_{\boldsymbol{k}} \left(u_{\boldsymbol{k}} + v_{\boldsymbol{k}} c^{\dagger}_{\boldsymbol{k}\uparrow} c^{\dagger}_{-\boldsymbol{k}\downarrow}\right)|0\rangle. \tag{2.1.27}$$

The gap function is derived as follows. Since the quasi-particle is the free fermion, the number of electrons per site is

$$\langle \gamma^{\dagger}_{\boldsymbol{k}\uparrow}\gamma_{\boldsymbol{k}\uparrow}\rangle = \langle \gamma^{\dagger}_{-\boldsymbol{k}\downarrow}\gamma_{-\boldsymbol{k}\downarrow}\rangle = \frac{1}{1+e^{\beta E(\boldsymbol{k})}}, \tag{2.1.28}$$

where $1/\beta = k_{\mathrm{B}}T$. k_{B} is the Boltzmann constant and T is the temperature. Using Eqs. (2.1.21) and (2.1.28), we have

$$\langle c_{\boldsymbol{k}\uparrow}c_{-\boldsymbol{k}\downarrow}\rangle = \frac{\Delta_{\mathrm{SC}}(\boldsymbol{k})}{2E(\boldsymbol{k})}\tanh\left(\frac{1}{2}\beta E(\boldsymbol{k})\right). \tag{2.1.29}$$

Thus, the self-consistent equation of gap functions is given by

$$\Delta_{\mathrm{SC}}(\boldsymbol{k}) = -\sum_{\boldsymbol{k}'} V(\boldsymbol{k},\boldsymbol{k}')\frac{\Delta_{\mathrm{SC}}(\boldsymbol{k}')}{2E(\boldsymbol{k}')}\tanh\left(\frac{1}{2}\beta E(\boldsymbol{k}')\right), \tag{2.1.30}$$

where $V(\boldsymbol{k},\boldsymbol{k}')$ is the interaction between up-spin and down-spin electrons ($V(\boldsymbol{k},\boldsymbol{k}') = V_{\downarrow\uparrow;\uparrow\downarrow}(\boldsymbol{k},\boldsymbol{k}')$).

Now, the momentum dependence of $V(\boldsymbol{k},\boldsymbol{k}')$ is neglected and the interaction is attractive ($V(\boldsymbol{k},\boldsymbol{k}') = -V < 0$). The gap equation is then written as

$$\Delta_{\mathrm{SC}}(\boldsymbol{k}) = V\sum_{\boldsymbol{k}'} \frac{\Delta_{\mathrm{SC}}(\boldsymbol{k}')}{2E(\boldsymbol{k}')}\tanh\left(\frac{1}{2}\beta E(\boldsymbol{k}')\right). \tag{2.1.31}$$

Since the right side of Eq. (2.1.31) is constant, $\Delta_{\mathrm{SC}}(\boldsymbol{k})$ is also constant. As T decreases, the superconducting gap Δ_{SC} starts to be finite at T_{c}. Then, the gap equation is

$$1 = V\sum_{\boldsymbol{k}'} \frac{1}{2\xi(\boldsymbol{k}')}\tanh\left(\frac{\xi(\boldsymbol{k}')}{2k_{\mathrm{B}}T_{\mathrm{c}}}\right). \tag{2.1.32}$$

The summation over $\boldsymbol{k}'$ is restricted to a narrow energy window ($-\omega_{\mathrm{D}} \leq \xi \leq \omega_{\mathrm{D}}$) where the density of states is constant $D(E_{\mathrm{F}})$. We have

$$1 \sim VD(E_{\mathrm{F}})\int_{-\omega_{\mathrm{D}}}^{\omega_{\mathrm{D}}} \frac{1}{2\xi}\tanh\left(\frac{\xi}{2k_{\mathrm{B}}T_{\mathrm{c}}}\right)d\xi, \tag{2.1.33}$$

where ω_{D} denotes the Debye frequency which determines the maximum value of phonon frequencies. For $k_{\mathrm{B}}T_{\mathrm{c}} \ll \omega_{\mathrm{D}}$, by using a dimensionless variable $x = \xi/2k_{\mathrm{B}}T_{\mathrm{c}}$ and the partial integration, Eq. (2.1.33) becomes now

$$1 \sim \lambda \log\left(\frac{2\gamma\omega_{\mathrm{D}}}{\pi k_{\mathrm{B}}T_{\mathrm{c}}}\right), \tag{2.1.34}$$

where $\log\gamma = 0.577\cdots$ denotes the Euler constant and $\lambda = VD(E_{\mathrm{F}})$. For $\lambda > 0$ (attractive force), using Eq. (2.1.34) gives a famous T_{c} formula

$$k_{\mathrm{B}}T_{\mathrm{c}} = 1.13\omega_{\mathrm{D}}\exp\left(-1/\lambda\right). \tag{2.1.35}$$

As can been seen in this equation, the assumption $k_{\mathrm{B}}T_{\mathrm{c}} \ll \omega_{\mathrm{D}}$ corresponds to the weak electron-phonon coupling limit ($\lambda = VD(E_{\mathrm{F}}) \ll 1$). Moreover, the exponential factor $\exp(-1/\lambda)$ in Eq. (2.1.35) exhibiting the essential singularity proves that the superconductivity results from the non-perturbative effect.

At absolute zero, the gap equation (Eq. (2.1.31)) is written as

$$1 = \lambda \int_{-\omega_{\mathrm{D}}}^{\omega_{\mathrm{D}}} \frac{d\xi}{2\sqrt{\xi^2 + \Delta_0^2}} \sim \lambda \log\left(\frac{2\omega_{\mathrm{D}}}{\Delta_0}\right). \tag{2.1.36}$$

Thus,

$$\Delta_0 = 2\omega_{\mathrm{D}}\exp\left(-1/\lambda\right), \tag{2.1.37}$$

where Δ_0 denotes the superconducting gap at $T = 0$. Using Eqs. (2.1.35) and (2.1.37) gives an universal relation in the BCS theory

$$\frac{2\Delta_0}{k_{\mathrm{B}}T_{\mathrm{c}}} = 3.53. \tag{2.1.38}$$

In this way, the T_{c} formula for the phonon-mediated s-wave superconductivity can be obtained in the weak coupling regime.

2.2 Strongly correlated electron systems

We next move on to unconventional high-temperature superconductors. The cuprates and iron-based superconductors are well known as typical strongly correlated electron systems. The strength of electron correlation is defined as the ratio of kinetic energy and the Coulomb interaction. Let us consider a Fermi gas with the mean distance between electrons r_{s} in a three-dimensional system. The kinetic energy and Coulomb potential energy are proportional to $1/r_{\mathrm{s}}^2$ and $1/r_{\mathrm{s}}$, respectively, so that the kinetic energy decreases earlier than the potential energy as r_{s} increases. Therefore, when the mean distance between electrons is large, the Coulomb interaction is dominant compared to the kinetic interaction.

The same is true of condensed matters. As the interatomic distance increases, the overlap integral of neighboring atomic orbitals decreases and the Coulomb interaction becomes dominant, resulting in the Mottness. Thus, transition metal oxides tend to be Mott insulators because the *d* orbitals of transition metals comprising bands near the Fermi level are far from each other due to oxygens surrounding the transition metals.

The common properties of strongly correlated electron systems are as follows:

1. Bandwidths of bands near the Fermi level are narrow.
2. Few bands intersect the Fermi level and are isolated from the other bands.

As mentioned above, the narrow bandwidth is due to small atomic orbitals compared to the lattice constant, which result in a small overlap of neighboring atomic orbitals. At the same time, the small atomic orbitals enhance a local Coulomb interaction between the orbital electrons. Next, the reduction of the screening effect is also required to preserve the strong correlation. The screening effect means that in a solid, a long-range term of Coulomb potential of an electron is screened by polarized ions surrounding the electron. If few bands near the Fermi level are isolated from the other bands, the screening effect is so weak that the electron correlation remains strong.

Moreover, the strong correlation effect brings about the competition between various ordering transitions, such as magnetism and dielectricity, superconductivity. Such a competition leads to a break down of mean-field theories like the local density approximation (LDA), which is a kind of first principles band calculations. The first principles calculation is the method to evaluate and estimate physical quantities of condensed matters only from constituent elements and fundamental physical constants, such as electron mass and elementary charge, based on the principle of quantum mechanics. The density functional theory (DFT) is a standard method for the first principles calculations. Omitting the details, the DFT has a variety of formalisms, including the LDA and generalized gradient approximation (GGA), GW approximation. The DFT provides a practical framework for estimating physical quantities of various weakly correlated systems, such as semiconductors. However, if the DFT is applied to strongly correlated systems, for example, transition metal oxides and organic conductors, rare-earth compounds, the obtained results often do not match with experimental results not only quantitatively but also qualitatively. For instance, a LDA study of a cuprate $\mathrm{La_2CuO_4}$ suggested a presence of a Fermi surface originating from the Cu $3d_{x^2-y^2}$ orbital, i.e. a metallic phase [42, 43]. Actually, however, the mother compounds of the cuprates are typical Mott insulating phases with a large gap of about 2 eV.

2.3 Downfolding

One of valid procedures to study the strongly correlated electrons is a downfolding approach (e.g. Ref. [44]) including the following three steps:

1. Evaluate the global band structure including bands far from the Fermi level by using DFT such as LDA, GGA or GW.
2. Construct effective models for low-energy degrees of freedom near the Fermi level incorporating the higher energy degrees of freedom.

3. Solve the low-energy effective model by using an accurate low-energy solver.

Putting it simply, electronic states for high- or low-energy degrees of freedom are evaluated by relying on DFT and low energy solvers, respectively. This downfolding method allows us to evaluate and estimate physical properties with high accuracy. This has been applied to various correlated systems, such as cuprates and iron-based superconductors, producing outstanding results. These researches tell us that a ground state is sensitive to effective model parameters due to ordering competition. Therefore, the accurate evaluation of model parameters is indispensable to reveal properties of actual strongly correlated materials. However, the modeling often involves some ambiguities, which can give rise to large change of model parameters especially for Coulomb interactions even in relatively simple systems like cuprates.

2.4 Hubbard model

One of simplest models of strongly correlated electron systems is a single-orbital Hubbard model including the tight binding term and the on-site Coulomb term,

$$\hat{H} = -\sum_{i>j}\sum_{\sigma} t_{ij}(c_{i\sigma}^{\dagger}c_{j\sigma} + \mathrm{h.c.}) + U\sum_{i} n_{i\uparrow}n_{i\downarrow}. \tag{2.4.1}$$

Here $c_{i\sigma}^{\dagger}/c_{i\sigma}$ creates/annihilates a fermion with spin $\sigma(=\uparrow,\downarrow)$ on the i^{th} site. t_{ij} is the hopping integral between site i and site j. U is the on-site Coulomb interaction, and $n_{i\sigma} = c_{i\sigma}^{\dagger}c_{i\sigma}$. This model has been considered to describe cuprates properly. Let us consider the half-filled Hubbard model on the square lattice. If U is much larger than the bandwidth, electrons are localized due to large U, resulting in the Mott insulating phase. If carrier is doped, electrons start to move like sliding puzzle. Historically, the parameters of low-energy effective models, such as hopping integrals t_{ij} and Hubbard U, have been given by hand. As mentioned above, the model parameters can be obtained from first principles calculations. From now on, we show numerical methods to solve this Hamiltonian and demonstrate the possible mechanism of the high-temperature superconductivity in cuprates.

2.5 Perturbation theories

A possible scenario for the mechanism of high-temperature unconventional superconductivity can be given by starting with the “Fermi liquid” theory, where the low energy excitation of correlated electron systems corresponds to an elementary fermionic particle incorporating the correlation effect, called “quasi-particle”, at low temperature. The normal phase of these unconventional superconductors exhibits completely different critical behaviors from that of the ordinal Fermi liquid but can be regarded as Fermi liquid like systems where there are dressed particles with both the spin and charge.

The spin-fluctuation mediated pairing is one of leading candidates for the mechanism of high-temperature superconductivity. Around a magnetic phase transition (paramagnetic phase to antiferromagnetic or ferromagnetic, SDW phases), there are no long-range spin-orders but spin fluctuations, which can mediate the pairing similarly to phonons.

Taking a two-dimensional Hubbard model as an example, we briefly explain the spin-fluctuation mediated pairing by using perturbation theories. According to the linear response theory, dynamical spin susceptibilities are given by

$$\chi_{\mathrm{s}}^{zz}(\boldsymbol{q}, i\omega_m) = \int_0^\beta d\tau \exp(i\omega_m \tau) \frac{1}{N} \langle S_{\boldsymbol{q}}^z(\tau) S_{-\boldsymbol{q}}^z(0) \rangle, \tag{2.5.1}$$

$$\chi_{\mathrm{s}}^{\pm}(\boldsymbol{q}, i\omega_m) = \int_0^\beta d\tau \exp(i\omega_m \tau) \frac{1}{N} \langle S_{\boldsymbol{q}}^+(\tau) S_{-\boldsymbol{q}}^-(0) \rangle, \tag{2.5.2}$$

$$\chi_{\mathrm{c}}(\boldsymbol{q}, i\omega_m) = \int_0^\beta d\tau \exp(i\omega_m \tau) \frac{1}{2N} \langle \rho_{\boldsymbol{q}}(\tau) \rho_{-\boldsymbol{q}}(0) \rangle, \tag{2.5.3}$$

where ω_m denotes the Matsubara frequency for bosons ($\omega_m = 2m\pi k_{\mathrm{B}}T$) and $\langle \hat{A} \rangle$ is the statistical average of an observable $\hat{A}$ at a temperature $k_{\mathrm{B}}T (= 1/\beta)$. N is the total number of k-point mesh. $S_{\boldsymbol{q}}^z$ and $S_{\boldsymbol{q}}^+$, $S_{\boldsymbol{q}}^-$ denote the z-component of the spin operator and spin creation and annihilation operators, respectively. $\rho_{\boldsymbol{q}}$ is the charge operator. These operators are defined as

$$\boldsymbol{S}_{\boldsymbol{q}} = \frac{1}{2} \sum_{\boldsymbol{k}} \sum_{\sigma\sigma'} c_{\boldsymbol{k}\sigma}^\dagger \boldsymbol{\sigma}_{\sigma\sigma'} c_{\boldsymbol{k}+\boldsymbol{q}\sigma'}, \tag{2.5.4}$$

$$S_{\boldsymbol{q}}^{\pm} = S_{\boldsymbol{q}}^x \pm i S_{\boldsymbol{q}}^y, \tag{2.5.5}$$

$$\rho_{\boldsymbol{q}} = \sum_{\boldsymbol{k}} (c_{\boldsymbol{k}\uparrow}^\dagger c_{\boldsymbol{k}+\boldsymbol{q}\uparrow} + c_{\boldsymbol{k}\downarrow}^\dagger c_{\boldsymbol{k}+\boldsymbol{q}\downarrow}). \tag{2.5.6}$$

In the case of the paramagnetic state without orders, there is the spin rotational symmetry and spin susceptibilities are given by

$$2\chi_{\mathrm{s}}^{zz}(\boldsymbol{q}, i\omega_m) = \chi_{\mathrm{s}}^{\pm}(\boldsymbol{q}, i\omega_m) \equiv \chi_{\mathrm{s}}(\boldsymbol{q}, i\omega_m). \tag{2.5.7}$$

These susceptibilities are represented as

$$\chi_{\mathrm{s}}(\boldsymbol{q}, i\omega_m) = \frac{\chi_0(\boldsymbol{q}, i\omega_m)}{1 - U\chi_0(\boldsymbol{q}, i\omega_m)}, \tag{2.5.8}$$

$$\chi_{\mathrm{c}}(\boldsymbol{q}, i\omega_m) = \frac{\chi_0(\boldsymbol{q}, i\omega_m)}{1 + U\chi_0(\boldsymbol{q}, i\omega_m)}, \tag{2.5.9}$$

where $\chi_0(\boldsymbol{q}, i\omega_m)$ denotes the irreducible susceptibility. The irreducible susceptibility is defined as the Feynman diagram where diagrams connect with each other even when arbitrary two internal lines are removed.

2.5.1 Random phase approximation

In the random phase approximation (RPA), one employs the following noninteracting irreducible susceptibility

$$\chi_0(\boldsymbol{q}, i\omega_m) = -\frac{k_{\mathrm{B}}T}{N}\sum_{\boldsymbol{k},n} G_0(\boldsymbol{q}+\boldsymbol{k}, i\omega_m + i\varepsilon_n)G_0(\boldsymbol{k}, i\varepsilon_n) \tag{2.5.10}$$

$$= \frac{1}{N}\sum_{\boldsymbol{k}} \frac{f(\xi(\boldsymbol{q}+\boldsymbol{k})) - f(\xi(\boldsymbol{k}))}{i\omega_m - [\xi(\boldsymbol{q}+\boldsymbol{k}) - \xi(\boldsymbol{k})]} \tag{2.5.11}$$

where ε_n denotes the Matsubara frequency for fermions ($\varepsilon_n = (2n+1)\pi k_{\mathrm{B}}T$). $G_0(\boldsymbol{k}, i\varepsilon_n)$ is the Green's function for free electrons

$$G_0(\boldsymbol{k}, i\varepsilon_n) = [i\varepsilon_n - \xi(\boldsymbol{k})]^{-1}. \tag{2.5.12}$$

Further, $f(\xi(\boldsymbol{k})) = [1 + \exp(\beta\xi(\boldsymbol{k}))]^{-1}$ denotes the Fermi distribution function.

Skipping several procedures, we show the gap equation of superconductivity caused by an effective interaction. By using the spin and charge susceptibilities, the effective interactions are given by

$$\begin{aligned}\Gamma_{\sigma,-\sigma}(\boldsymbol{k}, \boldsymbol{q}, i\varepsilon_n, i\varepsilon_m) = U &- \frac{1}{2}U^2\chi_{\mathrm{c}}(\boldsymbol{k}-\boldsymbol{q}, i\varepsilon_n - i\varepsilon_m)\\ &+ \frac{1}{2}U^2\chi_{\mathrm{s}}(\boldsymbol{k}-\boldsymbol{q}, i\varepsilon_n - i\varepsilon_m) + U^2\chi_{\mathrm{c}}(\boldsymbol{k}+\boldsymbol{q}, i\varepsilon_n + i\varepsilon_m),\end{aligned} \tag{2.5.13}$$

$$\begin{aligned}\Gamma_{\sigma,\sigma}(\boldsymbol{k}-\boldsymbol{q}, i\varepsilon_n - i\varepsilon_m) = &-\frac{1}{2}U^2\chi_{\mathrm{c}}(\boldsymbol{k}-\boldsymbol{q}, i\varepsilon_n - i\varepsilon_m)\\ &- \frac{3}{2}U^2\chi_{\mathrm{s}}(\boldsymbol{k}-\boldsymbol{q}, i\varepsilon_n - i\varepsilon_m),\end{aligned} \tag{2.5.14}$$

Then, the Green's function of quasi-particles satisfies the Dyson's equation

$$[G(\boldsymbol{k}, i\varepsilon_n)]^{-1} = [G_0(\boldsymbol{k}, i\varepsilon_n)]^{-1} - \Sigma(\boldsymbol{k}, i\varepsilon_n), \tag{2.5.15}$$

$$\begin{aligned}\Sigma(\boldsymbol{k}, i\varepsilon_n) = -\frac{k_{\mathrm{B}}T}{N}\sum_{\boldsymbol{q},m}&[G(\boldsymbol{q}, i\varepsilon_m)\Gamma_{\sigma,\sigma}(\boldsymbol{k}-\boldsymbol{q}, i\varepsilon_n - i\varepsilon_m)\\ &- U^2G_0(\boldsymbol{q}, i\varepsilon_m)\chi_0(\boldsymbol{k}-\boldsymbol{q}, i\varepsilon_n - i\varepsilon_m)],\end{aligned} \tag{2.5.16}$$

where $\Sigma(\boldsymbol{k}, i\varepsilon_n)$ denotes the self-energy without vertex corrections. The gap equation is given by

$$\lambda\Delta(\boldsymbol{k}, i\varepsilon_n) = -\frac{k_{\mathrm{B}}T}{N}\sum_{\boldsymbol{q},m} G(\boldsymbol{q}, i\varepsilon_m)G(-\boldsymbol{q}, -i\varepsilon_m)\Gamma_{\sigma,-\sigma}(\boldsymbol{k}, \boldsymbol{q}, i\varepsilon_n, i\varepsilon_m)\Delta(\boldsymbol{q}, i\varepsilon_m), \tag{2.5.17}$$

where $\Delta(\boldsymbol{k}, i\varepsilon_n)$ denotes the superconducting gap. This equation is called the linearized Eliashberg equation. The eigenvalue λ of the linearized Eliashberg equation reaches

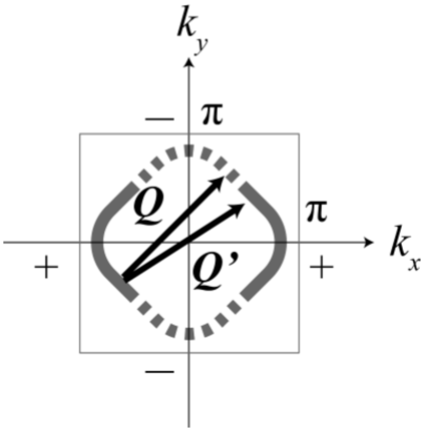

Fig. 2.1: Typical Fermi surface and $d_{x^2-y^2}$-gap structure of the hole-doped Hubbard model on the square lattice. $\boldsymbol{Q}$ and $\boldsymbol{Q}'$ denote nesting vectors.

unity at T_c, so that when it is calculated at a fixed temperature, systems with higher T_c give larger eigenvalues. In other word, λ calculated at a fixed temperature can be considered as a measure of T_c.

In the above equations, physical quantities are defined as functions of Matsubara frequencies, which can be mapped to functions of complex frequencies by using an analytic continuation, e.g. $\chi_\mathrm{s}(\boldsymbol{q}, i\omega_m) \to \chi_\mathrm{s}(\boldsymbol{q}, \omega)$ ($\omega \in \mathbb{C}$). From the gap equation (Eq. (2.5.17)), the $d_{x^2-y^2}$-wave superconducting phase is derived near the AFM phase in the Hubbard model on the square lattice, which corresponds to the simple model of cuprates. The band dispersion is given by

$$\varepsilon(\boldsymbol{k}) = -2t(\cos k_x + \cos k_y). \tag{2.5.18}$$

The Fermi surface and $d_{x^2-y^2}$-gap structure in the low hole-doping regime are shown in Fig. 2.1. Fermi surface nesting has been considered to be crucial for the occurrence of spin-fluctuation mediated superconductivity. The nesting means that two pieces of Fermi surfaces are connected with each other via a certain wave vector (nesting vector $\boldsymbol{Q}$). When there is good Fermi surface nesting ($\xi(\boldsymbol{k}+\boldsymbol{Q}) = \xi(\boldsymbol{k})$), the zero-energy irreducible susceptibility $\chi_0(\boldsymbol{Q}, \omega = 0)$ is enhanced as can be understood from in Eq. (2.5.11). As shown in Eqs. (2.5.8) and (2.5.13), the intraorbital repulsion U, combined with the nesting ($U\chi_0(\boldsymbol{q}, \omega = 0) \sim 1$), induces spin fluctuation ($\chi_\mathrm{s}(\boldsymbol{q}, \omega = 0) \to \infty$), which in turn mediates scattering processes between electron and hole Fermi surfaces ($\Gamma_{\sigma,-\sigma}(\boldsymbol{k}, \boldsymbol{k}+\boldsymbol{Q}, i\varepsilon_n, i\varepsilon_n) \to -\infty$). Then, the simplified gap equation is

$$\Delta(\boldsymbol{k}) \propto -V(\boldsymbol{Q})\Delta(\boldsymbol{k}+\boldsymbol{Q}) \tag{2.5.19}$$

where the energy dependency is omitted. $V(\boldsymbol{Q})(> 0)$ denotes the effective interaction between up-spin and down-spin electrons, which is roughly proportional to $\Gamma_{\sigma,-\sigma}(\boldsymbol{k}, \boldsymbol{k}+$

$\boldsymbol{Q}, i\varepsilon_n, i\varepsilon_n)$. Multiplying through by $\Delta(\boldsymbol{k})$, we have

$$\Delta(\boldsymbol{k})^2 \propto -V(\boldsymbol{Q})\Delta(\boldsymbol{k})\Delta(\boldsymbol{k}+\boldsymbol{Q}). \tag{2.5.20}$$

If $\Delta(\boldsymbol{k})^2$ is finite, the gap function should satisfy the following inequality

$$\Delta(\boldsymbol{k})\Delta(\boldsymbol{k}+\boldsymbol{Q}) < 0. \tag{2.5.21}$$

Therefore, if the superconducting gap changes the sign before and after the pair scattering ($\boldsymbol{k}\uparrow; -\boldsymbol{k}\downarrow \rightarrow \boldsymbol{k}+\boldsymbol{Q}\uparrow; -\boldsymbol{k}-\boldsymbol{Q}\downarrow$), the scattering processes act as a "repulsive" pairing interaction around $\boldsymbol{Q}$.

In the square lattice Hubbard model, a RPA study indicates the $d_{x^2-y^2}$-wave superconductivity, which is consistent with the experiments for the cuprates. However, the RPA is not applicable to the strong-correlation regime ($U/t \gg 1$), where superconductivity can be strongly enhanced, due to the Stoner-type instability ($U\chi_0(\boldsymbol{q}, \omega = 0) \sim 1$) because it neglects the interaction between electrons with various momentum. In the weak-correlation regime ($U/t \approx 1$), where the RPA is applicable, the estimated T_{c} is about $10^{-3}t$, which is very low compared to that of cuprates when the hopping integral takes an experimental value ($t = 0.4$ eV).

2.5.2 Fluctuation exchange approximation

The fluctuation exchange (FLEX) approximation is an expansion of the RPA, which is applicable to the relatively strong-correlation regime [45, 46]. In the FLEX approximation, the irreducible susceptibility is given by

$$\chi_0(\boldsymbol{q}, i\omega_m) = -\frac{k_{\mathrm{B}}T}{N_{\mathrm{s}}} \sum_{\boldsymbol{k},n} G(\boldsymbol{q}+\boldsymbol{k}, i\omega_m + i\varepsilon_n)G(\boldsymbol{k}, i\varepsilon_n) \tag{2.5.22}$$

As can be seen in this formalism, the irreducible susceptibility is self-consistently determined taking account of spin and charge fluctuations for the whole momentum (in the case of the RPA, the momentum takes the single value). Thus, the FLEX approximation incorporates the mode-mode coupling, which can reduce the Stoner-type instability.

For the realistic $U/t \sim 10$, the FLEX approximation exhibits the $d_{x^2-y^2}$-wave superconductivity similarly to the RPA and estimates the T_{c} to be about $10^{-2}t$, which is comparable to that of cuprates for $t = 0.4$ eV.

To begin with, in two-dimensional systems, a phase transition is rigorously forbidden at finite temperature by the Mermin-Wagner theorem. In addition, in one-dimensional systems, the phase transition is forbidden even at absolute zero by the theorem. However, the perturbation theory predicts the existence of phase transitions at finite-temperature, which appears to be contradictory to the Mermin-Wagner theorem. Throughout this thesis, we implicitly assume a working hypothesis that T_{c} estimated from the mean-field theory can correspond to that for two (one) dimensional systems weakly coupled with the other layers (chains).

2.6 Real space description of repulsive pairing interaction

Perturbation theories demonstrate that anisotropic superconductivity can be induced by spin fluctuation originating from the Hubbard U. At first glance, pairing originating from a purely repulsive interaction may seem strange strange but can be explained intuitively in the real space. Let us consider the square lattice Hubbard model with large U. An up-spin electron can move to the next site only when there are no up-spin electron at that site. Near half-filling, there has to be (nearly) one electron per site in average, the absence of up-spin electron implies presence of a down-spin electron. Electrons tend to hop to the nearest neighboring sites to reduce the total energy but return to the original site to avoid the Hubbard U. This can be considered as an effective nearest neighbor attractive interaction between up- and down- spin electrons. Actually, the Mott insulating state occurs due to the strong-correlation effect at half filling. By hole-doping, the electron mobility can be obtained like a sliding puzzle, resulting in superconductivity.

What is interesting is that in high-temperature superconductors, the same pairing symmetry is expected from momentum and real space descriptions corresponding to the weak and strong correlation limit, respectively. In principle, the pairing symmetry can change with respect to strength of correlations. The matching between these two pictures may be important for the occurrence of the high-temperature superconductivity.

2.7 Pairing mechanism of iron-based superconductors

We come back to the iron-based superconductors. As shown in Fig. 2.2, the nesting between disconnected pockets of the Fermi surface induces an interband pairing scattering associated with the nesting vector. This can lead to the superconducting gap changes the sign between electron and hole Fermi surfaces, namely, the sign-reversal s-wave pairing (see Eq. (2.5.20)) [17, 22].

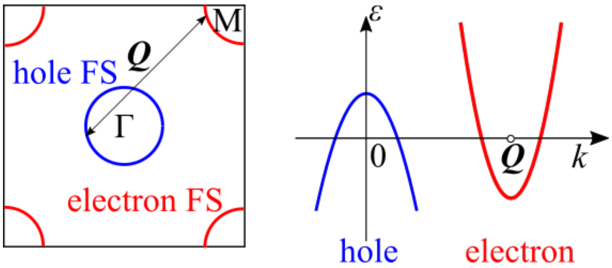

Fig. 2.2: Typical Fermi surface and band structure of iron-based superconductors. The arrow denotes the nesting vector $\boldsymbol{Q} = (\pi, 0)$.

3 Review on previous studies on multiband superconductivity with incipient band

After the observations of the iron-based superconductors where the nesting is degraded or absent, the role of "incipient bands", which sit close to, but do not intersect the Fermi level (see section 1.5), has received much attention. Various authors have suggested that the spin-fluctuation scattering of pairs between an electron Fermi surface and an incipient hole band can induce $s^{\pm}$ pairing [18, 31, 33, 35–40]. In this section, we review the previous studies on multiband superconductors with the incipient band.

3.1 Bilayer Hubbard model

In the context of the iron-based superconductors, the bilayer Hubbard model, which has been extensively studied in the past [47–56] has recently attracted renewed focus. Having hole and electron Fermi surfaces, it can be regarded as a single-orbital analogue of the iron-based superconductors. In fact, it has been found in previous studies that $s^{\pm}$ pairing is favored over $d_{x^2-y^2}$ pairing by increasing the relative strength of the inter-layer nearest hopping to the intra-layer nearest hopping [57]. Further, as one of the bands becomes shallow or incipient, the spectral weight of spin fluctuation is transferred to higher energies, which can lead to $s^{\pm}$ pairing state in which a gap appears on the hole band with the opposite sign to the gap on the electron Fermi surfaces as shown in Fig. 3.2 [58–60].

The bilayer Hubbard model shown in Fig. 3.1 is given as

$$\begin{aligned} H = -t \sum_{\langle ij\rangle m\sigma} (c^{\dagger}_{im\sigma} c_{jm\sigma} + \text{h.c.}) - t_{\perp} \sum_{i\sigma} (c^{\dagger}_{i0\sigma} c_{i1\sigma} + \text{h.c.}) \\ - t'_{\perp} \sum_{\langle ij\rangle \sigma} (c^{\dagger}_{i0\sigma} c_{j1\sigma} + \text{h.c.}) + U \sum_{im} n_{im\uparrow} n_{im\downarrow}. \end{aligned} \tag{3.1.1}$$

where $c^{\dagger}_{im\sigma}/c_{im\sigma}$ are creation/annihilation operators for a fermion with spin $\sigma(=\uparrow,\downarrow)$ on the i^{th} site on the m^{th} layer (m=0 or 1) and $n_{im\sigma} = c^{\dagger}_{im\sigma} c_{im\sigma}$. The intra-layer hopping is t and the inter-layer hopping is $t_{\perp}$, the next nearest neighbor inter-layer hopping is $t'_{\perp}$. In momentum space, the binding and antibonding bands are given as

$$\varepsilon(\boldsymbol{k}) = -2(t + t'_{\perp} \cos k_z)(\cos k_x + \cos k_y) - t_{\perp} \cos k_z, \tag{3.1.2}$$

where the case of $k_z = 0$ (π) corresponds to the bonding (anti-bonding) band. At $t'_{\perp} = 0$, the bonding and antibonding bands have the same width, and for finite $t'_{\perp}$, the bonding

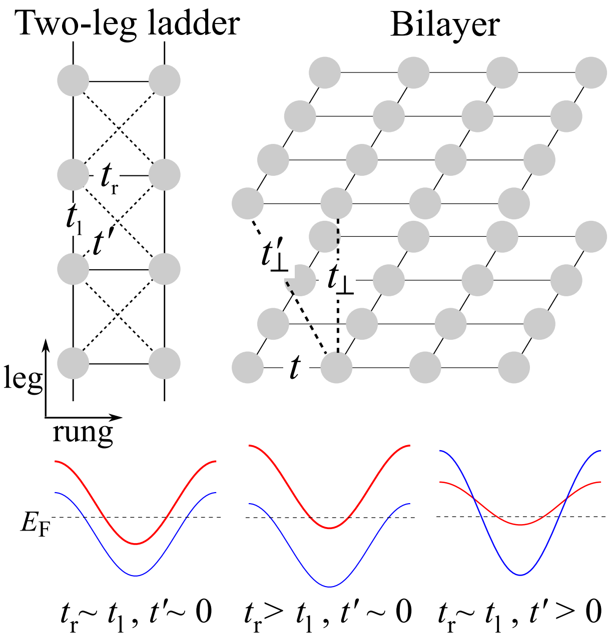

Fig. 3.1: Upper panel: the two-leg ladder lattice (left) and the bilayer lattice (right). Lower panels: typical band structures of the two-leg ladder lattice. Left: $t_\mathrm{r} \sim t_\mathrm{l}, t' \sim 0$, middle: $t_\mathrm{r} > t_\mathrm{l}, t' \sim 0$, right: $t_\mathrm{r} \sim t_\mathrm{l}, t' > 0$.

band is wide and the antibonding band is narrow (see the bottom panels of Fig. 3.1). Especially, at $t'_\perp = 1$, the antibonding band is perfectly flat. The band filling n is defined as the average number of electrons per site; $n = 1$ corresponds to half filling. For $n < 1$, the narrow antibonding band becomes incipient by hole doping (see the bottom panels of Fig. 3.1).

3.2 Systems with wide and narrow bands

Regarding the incipient band situation, it was proposed in refs. [61, 62] that strongly enhanced superconductivity can take place in a system with coexisting wide and narrow bands when the narrow band sits in the vicinity of the Fermi level. The electrons in the wide band, which are not so strongly renormalized, can form Cooper pairs with a strong pairing interaction mediated by the large number of interband pair scattering channels making use of the large DOS of the incipient narrow band as intermediate states (see Fig. 3.3). There, the Hubbard model on a two-leg ladder was studied within the FLEX approximation. In the two-leg ladder model, which is a two-band model with bonding and antibonding bands, one of the bands becomes wide and the other becomes narrow when diagonal hoppings t' are introduced. In nowadays' terminology, the narrow band in this case is incipient. This theory has been extended to various one and two dimensional systems with coexisting wide and narrow (or flat) bands [62–67]. However, as seen in

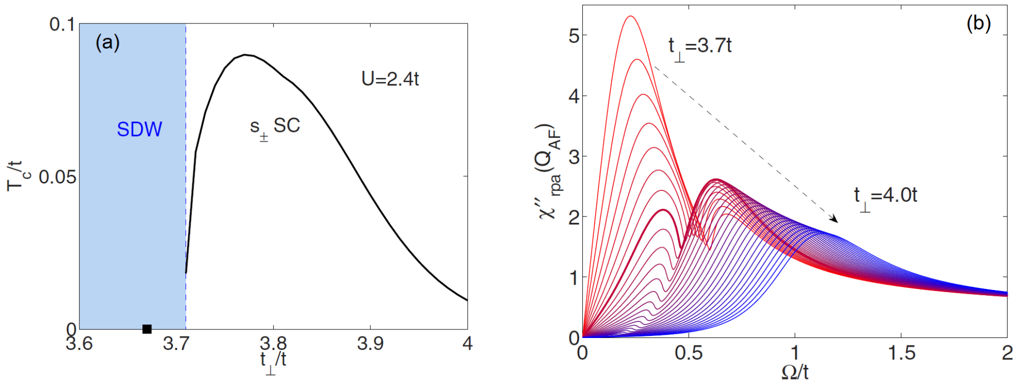

Fig. 3.2: (a) The $s^{\pm}$ superconducting transition temperature T_{c} versus $t_{\perp}/t$ for $n = 1.05$ and $U = 2.4t$ in the bilayer Hubbard model. The Lifshitz point is denoted by a filled square on the $t_{\perp}/t$ axis and the $t_{\perp}/t$ value where the RPA evaluated SDW instability ends by a vertical dashed line with light blue shading to the left of it. (b) The imaginary part of RPA $\chi(\pi,\pi,\pi,\Omega)$ at $T = 0.1t$ versus Ω for $U = 2.4t$ for different values of $t_{\perp}$, which continuously increases in units of $0.01t$ from $t_{\perp} = 3.7t$ (red curve) to $t_{\perp} = 4t$ (blue curve). The thick line represents the value of $t_{\perp} = 3.77t$ corresponding to the maximum value of T_{c}. This figure is taken from Ref. [58].

Fig. 3.2, superconductivity is strongly enhanced in the bilayer Hubbard model with incipient bands, where the DOS of the band edges is not large. What is the key factor to the enhancement of superconductivity in multiband systems?

3.3 Role of finite-energy spin-fluctuation mediated pairing

Recently, in ref. [68], the role played by the spin fluctuations in different energy ranges in two-band systems has been discussed as follows. There is a critical frequency ω_{c} in the spin-fluctuation spectrum, which should be smaller than a pairing cutoff energy ε_{c}. In general, the low-energy spin fluctuations with $\omega < \omega_{\mathrm{c}}$ lead to strong renormalization and have a pair breaking effect whilst finite-energy spin fluctuations with $\omega > \omega_{\mathrm{c}}$ enhance T_{c}. Further, the contribution from pair-breaking (pairing-effective) spin fluctuations scales as $1/\omega^4(1/\omega^2)$ [69]. Thus, when the low-lying spin fluctuations are suppressed while the finite-energy spin fluctuations are enhanced, superconductivity can be enhanced. In multiband systems, as one of bands gets away from the Fermi level, the spin-fluctuation spectral weight is transfered to higher energies. When the spin-fluctuation spectral weight is away from the critical frequency of spin fluctuations, but is concentrated at a frequency within the paring energy cutoff ($\varepsilon_{\mathrm{c}} > \varepsilon > \omega_{\mathrm{c}}$), the pairing interaction can be strong without strongly renormalizing the quasiparticles. On the other hand, when the spin fluctuations are concentrated at very low or too high energies, superconductivity is degraded. From this viewpoint, the commonalities and differences between the bilayer and the two-leg ladder has been discussed in ref. [68]. In this section, we will briefly

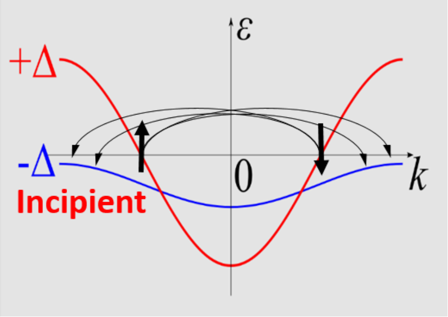

Fig. 3.3: Schematic picture of the system where a wide band crosses the Fermi level and a narrow band is incipient. The arrows indicate inter-band pair scattering channels.

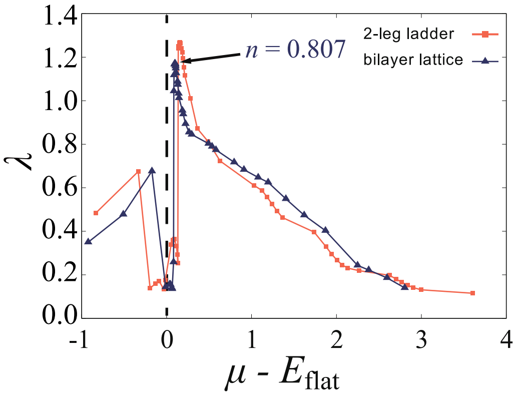

Fig. 3.4: Eigenvalue of the Eliashberg equation λ at $T = 0.05$ plotted against the bare Fermi level measured from the flat band energy for the two-leg ladder and bilayer lattices with $t' = 1$. This figure is taken from Ref. [68] with some modifications in the notations.

review papers [62, 68], which have partially motivated the study of the present thesis.

They obtained the renormalized Green's function by relying on the FLEX approximation. Using the Green's function, the imaginary part of the dynamical spin susceptibility $\chi(\boldsymbol{q}, \omega)$ is calculated. As a quantity that measures the strength of the spin fluctuation, they defined $\mathrm{Im}\Gamma(\omega)$ as

$$\mathrm{Im}\Gamma(\omega) \equiv \sum_{\boldsymbol{q}} \mathrm{Im}\chi(\boldsymbol{q}, \omega). \tag{3.3.1}$$

To study superconductivity mediated by the spin fluctuation, the linearized Eliashberg equation (Eq. (2.5.17)) is solved. The Eliashberg λ calculated at a fixed temperature can be a measure for T_{c}. Unless noted otherwise, they adopted $U/t = 6$, which is a typical value for the cuprate superconductors.

They considered a bilayer (two-leg ladder) lattice where the inter layer (chain) nearest neighbor hopping $t_{\perp}(t_{\mathrm{r}})$ is equal to the intra layer (chain) nearest neighbor hopping t. They started with the case with $t'_{\perp}(t') = 1$, where the antibonding band is perfectly flat.

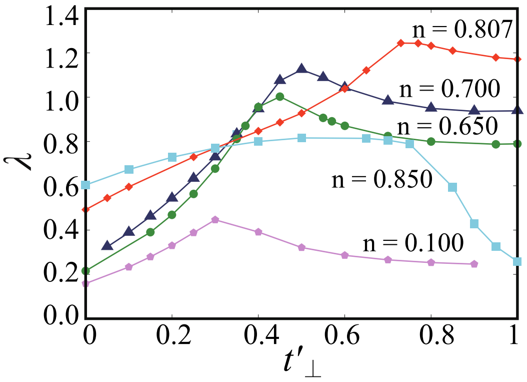

Fig. 3.5: λ at $T = 0.05$ plotted against $t'_{\perp}$ for the bilayer lattice with various band fillings. This figure is taken from Ref. [68] with some modifications in the notations.

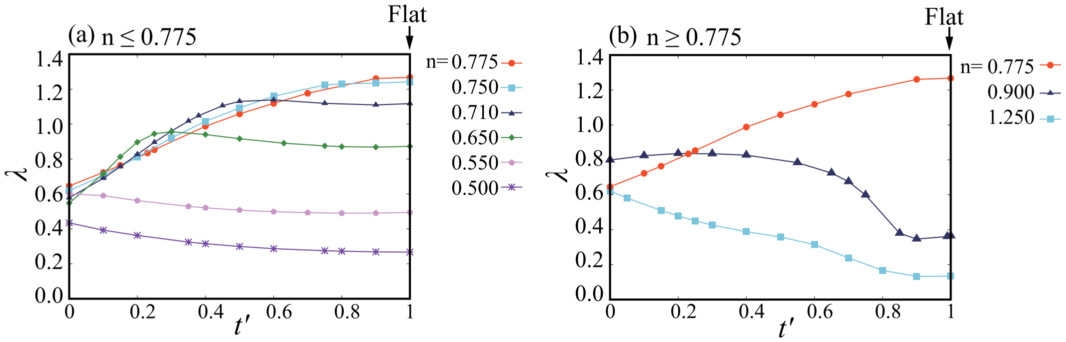

Fig. 3.6: λ at $T = 0.05$ plotted against t' for the two-leg ladder lattice with various band fillings. This figure is taken from Ref. [62] with some modifications in the notations.

Both in the bilayer and two-leg ladder lattices, the eigenvalue is maximized when the flat band is close to the Fermi level as shown in Fig. 3.4. Further, they also studied the case when the antibonding band has a finite band width, namely, for $t'_{\perp}(t') < 1$, both in these two systems with various band fillings, as shown in Figs. 3.5 and 3.6. In both of the models, it was found that λ is optimized at $t'_{\perp}(t')$ where the antibonding band nearly touches the Fermi level, and λ is reduced for smaller $t'_{\perp}(t')$, where the antibonding band intersects the Fermi level. On the other hand, the suppression of λ against the reduction of $t'_{\perp}(t')$ was found to be faster in 2D than in 1D.

The origin of this difference can be interpreted in terms of the relation between the frequency dependence of the spin fluctuations and the shape of the DOS. As $t'_{\perp}(t')$ increases, the bottom of the antibonding band becomes closer to the Fermi level. When the antibonding band is just above the Fermi level, around the bottom of the antibonding band contributes to the pair-breaking spin fluctuations, while the portion of the band somewhat away from the bottom contributes more to the pairing effective ones.

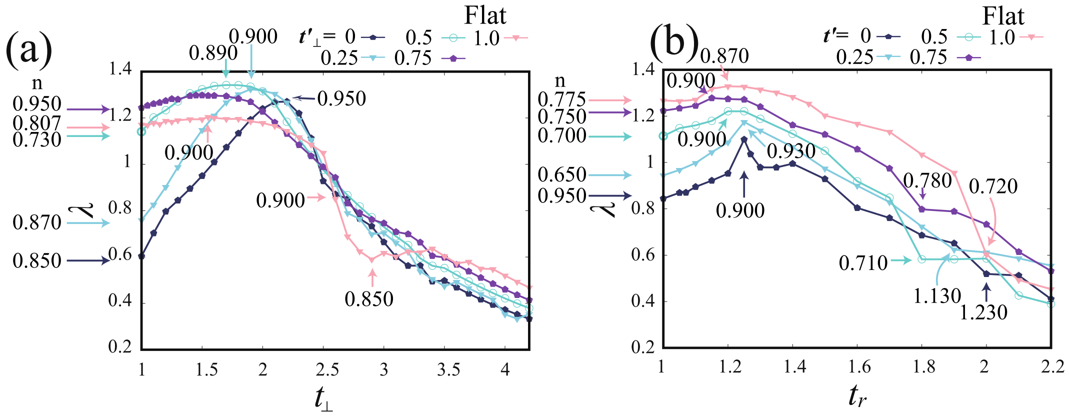

Fig. 3.7: (a) Maximized λ of the bilayer Hubbard model at $T = 0.05$ plotted against $t_\perp$ for various $t'_\perp$. λ is maximized for each set of $(t'_\perp, t_\perp)$ by varying the band filling n. The numbers near arrows indicate the band filing that maximizes λ. Similar plot for the two-leg Hubbard ladder model, where $t_\perp$ is replaced by t_r. This figure is taken from Ref. [68] with some modifications in the notations.

Therefore, for the bilayer model (Fig.3.10(c)), the large portion of the DOS produces the pairing-effective spin fluctuations while the small portion of the DOS gives rise to the pair-breaking ones. As the van Hove singularity of the antibonding band approaches the Fermi level (Fig. 3.10(e)), the large DOS increases the low-energy, pair-breaking, spin fluctuations rapidly (see the dash-dotted lines in Fig. 3.9). By contrast, in the two-leg ladder case, where the DOS at the antibonding band bottom is (nearly) diverging (Fig.3.10(d)), the large portion of the DOS contributes to the pair-breaking spin fluctuations, while the small portion of the DOS enhances the pairing-effective spin fluctuations. After the Fermi surface of the antibonding band is formed, the DOS at the Fermi level decreases (Fig. 3.10(f)), leading to a milder suppression of superconductivity.

In fact, they showed the relation between the spin-fluctuation spectral function and the eigenvalue λ. Figure 3.9 shows ImΓ as functions of the frequency ω for various t' and $(t_\perp, n)$. The parameter sets are chosen from those adopted in Fig. 3.7. When the spectral weight of spin fluctuation is concentrated at relatively low energies ($\omega < O(0.1)$), superconductivity is degraded. Large values of λ is obtained when the low-energy spin fluctuation with $\omega < O(0.1)$ is suppressed while the spin fluctuation in the range $\sim 0.1 < \omega <\sim 1$ is large. When the spin fluctuation weight is transferred to too high energies, superconductivity is once again degraded. Thus, when the low-energy spin fluctuation is suppressed while the finite-energy spin fluctuation is enhanced within a specific energy regime, superconductivity can be enhanced.

They also considered the cases when the vertical inter layer (chain) hopping $t_\perp(t_\mathrm{r})$ is larger than the intralayer nearest neighbor hopping t in the bilayer (two-leg ladder) system. Figures 3.7(a) and (b) show $t_\perp(t_\mathrm{r})$ dependence of λ which is maximized for each set of $(t', t_\perp(t_\mathrm{r}))$ by varying the band filling n. In most cases, λ is optimized at a band filling where the antibonding band is (near) incipient. On the other hand, in the case

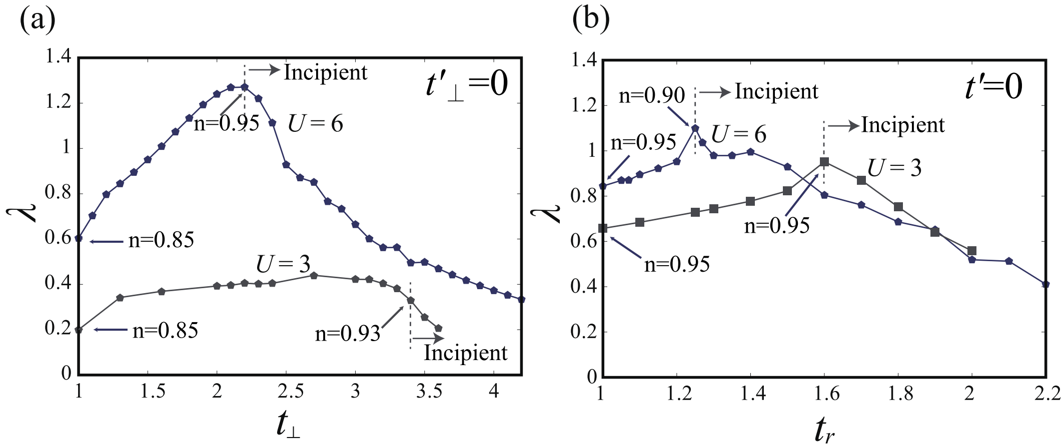

Fig. 3.8: (a) The result for $t'_\perp = 0$ is extracted from Fig. 3.7(a), and compared to that of $U = 3, t'_\perp = 0$. (b) A similar plot for the two-leg ladder, where the result for $t' = 0$ is extracted from Fig. 3.7(b), and compared to that of $U = 3, t' = 0$. This figure is taken from Ref. [68] with some modifications in the notations.

of $t' \sim 0, t_\perp(t_\mathrm{r}) \sim 1$, λ is optimized at a band filling close to half filling, where both bands form the Fermi surface firmly. In general, when the band filling is too far from half filling, superconductivity is degraded due to the suppression of correlation effects. As in the $t'_\perp(t')$ variation of λ, the suppression of λ against the reduction of $t_\perp(t_\mathrm{r})$ was found to be faster in 2D than in 1D. This difference is also attribute to the shape of the DOS as discussed in section 5.5.

They further studied the effect of electron correlation on the band width comparing cases with $U = 6$ and $U = 3$ for $t'_\perp = 0$ as shown in Fig. 3.8(a). λ is strongly suppressed for $U = 3$ compared to $U = 6$. Also, much larger $t_\perp$ is required to realize the incipient antibonding band, where λ is further suppressed. This result indicates that in the bilayer Hubbard model, superconductivity is not enhanced in the presence of the incipient band when U is small. In the bottom panel of Fig. 3.9, they also compared $\mathrm{Im}\Gamma$ for the two values of U. When U is large, the spin fluctuation weight is not only squeezed into a narrow energy range regime, but also it is enhanced due to the electron correlation effect. The situation here for the bilayer model was found to be also different from that in the two-leg ladder shown in Fig.3.8(b). In the 1D case, superconductivity is enhanced when the band is incipient even when U is small. This was again attributed to the shape of the DOS; it is diverging at the band edge, so that when the band is incipient, spin fluctuation develops in the energy range effective as a pairing glue even when U is small.

3.4 Motivation of the studies in the present thesis

As reviewed above, enhancement of superconductivity in some models with incipient bands has been attributed to different roles played by spin fluctuations in different energy ranges. There, the spin fluctuation spectra can be roughly understood from the shape of the density of states. However, it is not clear whether such a weak coupling view is valid when electron correlation becomes strong.

In this thesis, we study various two-band Hubbard models, namely, single-orbital Hubbard models on two-leg ladder and bilayer square lattices, and two-orbital Hubbard models on one-dimensional chain and square lattices, using a many-variable variational Monte-Carlo (mVMC) method [70, 71], which incorporates the strong correlation effect and order competitions accurately. By comparing the results for the two-leg (one-dimensional) ladder and the bilayer (two-dimensional) lattices, and with and without the coexistence of wide and narrow bands, we discuss how the DOS affects superconductivity and antiferromagnetism. Further, we show that two-orbital systems can be approximated as single-orbital two-band systems under specific conditions.

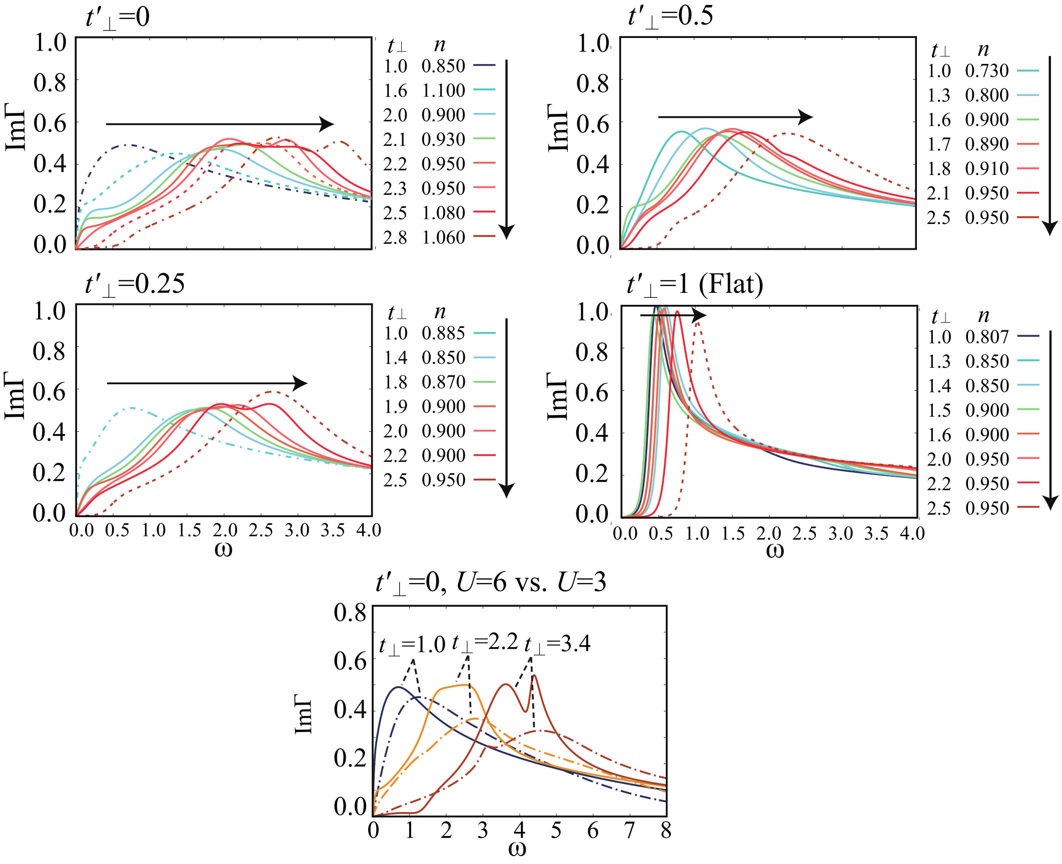

Fig. 3.9: Upper four panels : ImΓ plotted against ω for various $t'_\perp$ and $(t_\perp, n)$. The parameter sets are chosen from those adopted in Fig. 3.5. The solid, dashed, and dash-dotted lines correspond to the cases where $\lambda > 1.1$, $1.1 > \lambda > 0.8$, and $0.8 > \lambda$, respectively, in Fig. 3.5. Bottom panel : ImΓ plotted against ω for $t'_\perp = 0$ and $U = 6$ (solid) or $U = 3$ (dash-dotted). $(t_\perp, n)$ are chosen from those adopted in Fig. 3.8, where three values of $t_\perp$ are chosen ; $t_\perp = 1, t_\perp = 2.2$ (where the antibonding band for $U = 6$ goes just above the Fermi level) and $t_\perp = 3.4$ (where the antibonding band for $U = 3$ goes just above the Fermi level). This figure is taken from Ref. [68] with some modifications in the notations.

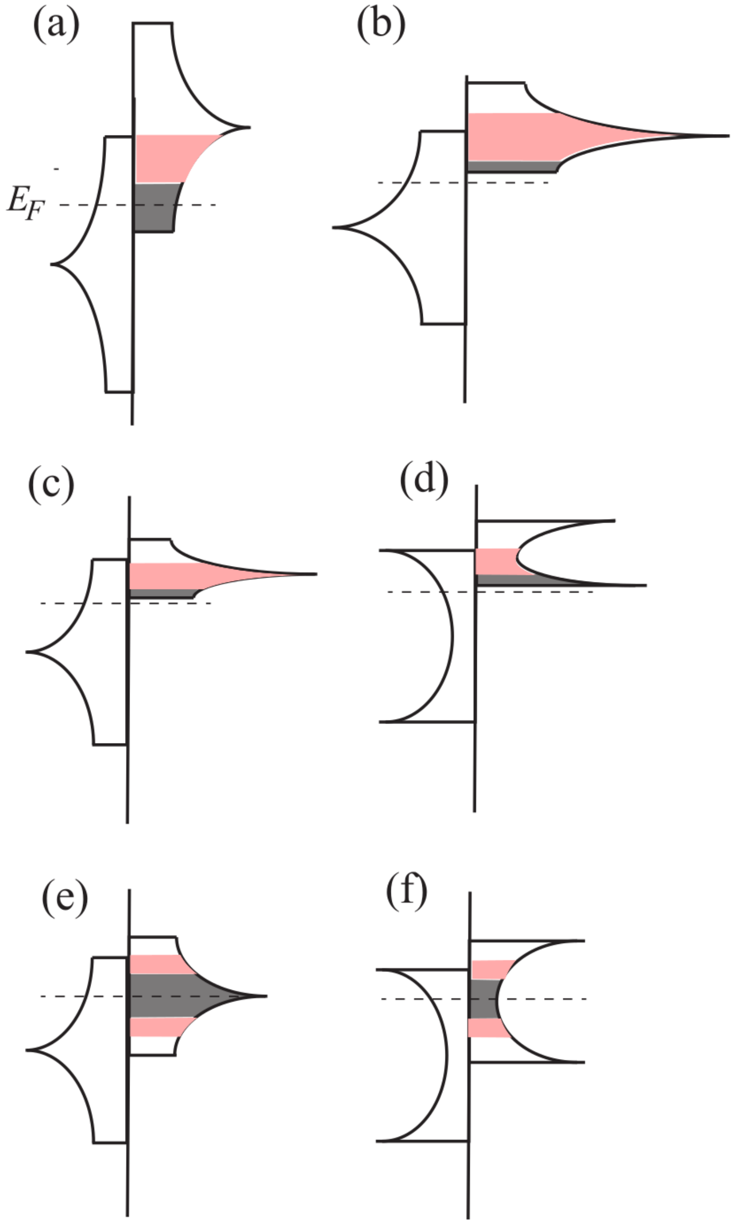

Fig. 3.10: Schematic images of the renormalized DOS of the bilayer and two-leg ladder models. In each figure, the left (right) side of the vertical line depicts the DOS of the bonding (antibonding) band. The gray area denotes the portion of the bonding band DOS which gives rise to the low energy (pair breaking) spin fluctuations, and the red area is the portion of the antibonding band DOS contributing to the spin fluctuations that are effective for superconductivity. (a)(b)(c)(e) are for the bilayer model, and (d)(f) are for the two-leg ladder model. (a) small U case, and (b) large U case with the antibonding band being incipient. (c) and (d) are cases where the anti bonding band is incipient. (e) and (f) are cases where $t'_\perp \sim 0$ and $t_\perp \sim 1$, so the antibonding band intersects the Fermi level (large amount of electrons are required for the antibonding band to be incipient).

4 Variational Monte-Carlo method

The variational Monte-Carlo (VMC) method is a combination of the variational theory with the Monte-Carlo technique for evaluating expectation values [72]. In the VMC method, the variational wave function $|\psi_\gamma\rangle$ with variational parameters γ is employed as the numerical solution of fundamental equations of quantum mechanics, such as the Schrödinger equation,

$$\hat{H}|\psi_\gamma\rangle = E_\gamma|\psi_\gamma\rangle, \tag{4.0.1}$$

Here $\hat{H}$ is the Hamiltonian and E_γ is the variational energy, which is calculated from the variational wave function using Monte-Carlo methods. Variational parameters are optimized so as to minimize the variational energy as follows:

$$E_0 \leq \min_\gamma E_\gamma = \min_\gamma \frac{\langle\psi_\gamma|\hat{H}|\psi_\gamma\rangle}{\langle\psi_\gamma|\psi_\gamma\rangle}, \tag{4.0.2}$$

where E_0 is the exact ground-state energy.

The VMC method does not have the negative sign problem unlike the auxiliary field quantum Monte-Carlo method, so that it can be applied to study relatively large system sizes even at large amplitude of electron interactions and geometrical frustration at reasonable computational cost. However, the result can be biased strongly depending on the form and initial value of variational wave functions. In the region where various phases compete with each other in a narrow energy window, the search for the correct ground state is very challenging.

A stochastic reconfiguration (SR) method has been developed to optimize large number of parameters stably and efficiently, which can reduce the substantial bias of the VMC method [73–75]. In the conventional VMC method, the number of variational parameters is several dozen. On the other hand, in the many-variable VMC (mVMC) method, one can employ thousands of variational parameters, which enables us to describe various quantum fluctuations of order parameters and strong correlation effects accurately [70, 71, 73–76]. Further, in comparison to the dynamical mean-field theory, the mVMC method has good tractability of various anisotropic orders and long-range interactions. The mVMC method has achieved fruitful and reproducible comparisons with the experimental results [77, 78], for instance, for cuprates and iron-based superconductors, in studies where effective Hamiltonians derived from ab *initio* calculations were adopted [79–84]. However, the physical intuition is still required to choose "good" variational wave functions. Systematic improvement of trial wave functions has been desired in the VMC method. In this section, we explain the VMC method.

4.1 Intuitive image and local minimum problem of mVMC method

The mVMC method searches for the optimum solution in the large parameter space. The above statement is trivial but is helpful for understanding this method deeply. In general, the trial wave function is defined as

$$|\psi_\gamma\rangle = \prod_i \exp(-i\gamma_i \hat{g}_i)|0\rangle, \tag{4.1.1}$$

where γ_i is a variational parameter and $\hat{g}_i$ is a generator defined as a product of creation and annihilation operators. The operator $\exp(-i\gamma_i\hat{g}_i)$ represents a translation in the parameter space. Now, we consider the translation of a trial wave function. The Taylor expansion is given by

$$\begin{aligned} |\psi(x+\delta x)\rangle &= |\psi(x)\rangle + \delta x \frac{\partial}{\partial x}|\psi(x)\rangle + \cdots + (\delta x)^n \left(\frac{\partial}{\partial x}\right)^n |\psi(x)\rangle + \cdots \\ &= \exp\left(\delta x \frac{\partial}{\partial x}\right)|\psi(x)\rangle = \exp\left(-i\delta x\hat{p}\right)|\psi(x)\rangle, \end{aligned} \tag{4.1.2}$$

where x is a parameter and the operator $\hat{p}(= i\frac{\partial}{\partial x})$ is a generator. $\exp\left(-i\delta x\hat{p}\right)$ denotes the translation operator. Therefore, Eq. (4.1.1) corresponds to the generalization of Eq. (4.1.2) in the high-dimensional parameter space.

Many-variables can provide so many paths not only toward the accurate optimum solution but also toward local minima. In the present circumstances, we have no *ab initio* way to obtain the optimum solution avoiding local minima. Thus, we have to choose initial values which are already close to the possible optimum solution. However, in most cases, we do not know the correct answer. The problem of choosing initial values is common with the dynamical mean-field theory (DMFT). Especially in the case of strongly-correlated electron systems, there are so many possible ground states due to ordering competition.

4.2 Ensemble average

The ensemble average is the average of a quantity that is a function of the individual states of the system. Now, we consider N particle systems. The ensemble average of an observable $\hat{A}$ is defined as

$$\langle\hat{A}\rangle = \frac{\langle\psi|\hat{A}|\psi\rangle}{\langle\psi|\psi\rangle}, \tag{4.2.1}$$

Here we consider the set of positions of N particles: $x = \{\boldsymbol{x}_1, \boldsymbol{x}_2, \cdots, \boldsymbol{x}_N\}$. $|x\rangle$ is the real space configuration defined as

$$|x\rangle = c^\dagger_{r_1\sigma_1} c^\dagger_{r_2\sigma_2} \cdots c^\dagger_{r_N\sigma_N}|0\rangle, \tag{4.2.2}$$

where $c^{\dagger}_{r_i\sigma_i}$ creates a fermion with spin σ_i at the position r_i $(i = 1, 2, \cdots, N)$. Eq. (4.2.1) is then rewritten as

$$\langle \hat{A} \rangle = \sum_x \frac{\langle \psi | \hat{A} | x \rangle \langle x | \psi \rangle}{\langle \psi | \psi \rangle} = \sum_x P(x) \frac{\langle \psi | \hat{A} | x \rangle}{\langle \psi | x \rangle}, \tag{4.2.3}$$

with

$$P(x) = \frac{|\langle \psi | x \rangle|^2}{\langle \psi | \psi \rangle}, \tag{4.2.4}$$

where $P(x)$ is the distribution of the configuration x.

4.3 Markov chain Monte-Carlo method

In general, large systems have enormous configurations, which give rise to the huge-computational cost of calculating the ensemble average. For instance, the total number of configurations is 2^N in the N site Ising model. On the other hand, if we can extract a small number of high-probability random states, we can calculate highly accurate ensemble averages at low cost as follows:

$$\langle \hat{A} \rangle \approx \frac{1}{M} \sum_{x \in \text{Random Sampling}} \frac{\langle \psi | \hat{A} | x \rangle}{\langle \psi | x \rangle}, \tag{4.3.1}$$

where M is the total number of random samples. The above method is called the importance sampling.

The importance sampling can be performed by a Markov chain Monte-Carlo method, which is a stochastic process defined as follows:

1. Each trials result in a finite number of possible events, whose indexes are $1, 2, \cdots, m$.
2. At the first trial, the event $1, 2, \cdots, m$ is produced with the possibility $P_1, P_2, \cdots, P_m$, respectively.

When events $i_1, i_2, \cdots, i_n$ are obtained up to the n^{th} trial, the event i is produced at the $(n+1)^{\text{th}}$ trial with the conditional possibility $\omega_{i_1 i_2 \cdots i_n i}$. This stochastic process is called the Markov chain. In particular, when the $(n+1)^{\text{th}}$ trial only depends on the latest result ($\omega_{i_1 i_2 \cdots i_n i} = \omega_{i_n i}$), the stochastic process is called the simple Markov chain. In addition, the (simple) Markov chain Monte-Carlo method is the method which produces the simple Markov chain making use of random numbers.

In N particle systems, the Markov chain Monte-Carlo method is performed as follows;

1. The initial configuration of N particles is set.
2. The temporary state j is generated.
3. We calculate the acceptance possibility ω_{ij} with which the current state i is transitioned to the temporary state j.

4. ω_{ij} is compared with uniform random numbers ξ ($1 > \xi \geq 0$). If $\omega_{ij} \geq \xi$, the temporary state j is adopted as the new state. Otherwise, the state does not change and the current state i is adopted as the new state.

5. Repeat the above steps 2-4.

6. Calculate physical quantities using the Monte-Carlo sampling.

The Mersenne twister method is often adopted as a random number generator for sampling [85].

ω_{ij} is derived from the following stochastic differential equation, called the Master equation,

$$P_i(n+1) - P_i(n) = -\sum_{j\neq i} \omega_{ij} P_i(n) + \sum_{j\neq i} \omega_{ji} P_j(n), \tag{4.3.2}$$

where $P_i(n)$ is the probability density, called the (stochastic) distribution, for the state i occurring at the n^{th} step. In equilibrium, the distribution is independent of the number of steps ($P_i(n) = P_i^{(\mathrm{eq})}$), and Eq. (4.3.2) is given by

$$0 = -\sum_{j\neq i} \omega_{ij} P_i^{(\mathrm{eq})} + \sum_{j\neq i} \omega_{ji} P_j^{(\mathrm{eq})}. \tag{4.3.3}$$

When the above equation is established, the following equation should be satisfied

$$\omega_{ij} P_i^{(\mathrm{eq})} = \omega_{ji} P_j^{(\mathrm{eq})}. \tag{4.3.4}$$

This condition is called the detailed balance. One of the possible solution is

$$\omega_{ij} = \begin{cases} P_j^{(\mathrm{eq})}/P_i^{(\mathrm{eq})} & (P_i^{(\mathrm{eq})} > P_j^{(\mathrm{eq})}) \\ 1 & (P_i^{(\mathrm{eq})} < P_j^{(\mathrm{eq})}) \end{cases}. \tag{4.3.5}$$

This algorithm is called the Metropolis-Hastings algorithm. Therefore, we have to calculate distributions $P_i^{(\mathrm{eq})}$ in the equilibrium state to obtain the transition probability ω_{ij}. In the high-temperature limit, $P_i^{(\mathrm{eq})}$ is approximated as the Boltzmann distribution. The transition probability is then given by $\omega_{ij} = \exp\left[-\beta(E_j - E_i)\right]$ where E_i is the total energy of the state i and β is the inverse temperature. These equations mean that when the energy of the temporary state j is lower (higher) than that of the current state i, the temporary state j is adopted as the new state with the probability 1 ($\exp\left[-\beta(E_j - E_i)\right]$). Therefore, we can obtain low-energy configurations from the Monte-Carlo method.

Quantum many-body states are superpositions of enormous configurations, so that the calculation of distributions $P_i^{(\mathrm{eq})}$ is hard. If you want to calculate the distributions exactly, you have to solve the large-scale eigenvalue problem, but it eliminates the merit of the Monte-Carlo method and is often impossible. Therefore, we have to employ some approximations to calculate distributions in equilibrium numerically with a reasonable computational cost.

4.4 Basic algorithm of variational Monte-Carlo method

The VMC method provides accurate estimation of distributions of configurations in quantum many-body systems at a low-computational cost. In this subsection, we show the basic algorithm of the VMC method [86]. We employ the Hubbard model for N_e electrons on N_s sites. As previously stated in the beginning of this section, the VMC method includes the following procedures:

1. Set up a variational wave function.
2. Evaluate the energy expectation value with the trial function.
3. Find a minimum of the energy expectation value with respect to the variational parameters.
4. Calculate various physical quantities with the optimized wave function.

The first step is the most important since the variational wave function determines the accuracy of this method. To describe a correlated paramagnetic state, we employ the following Gutzwiller's wave function:

$$|\psi_g\rangle = \mathcal{P}_\mathrm{G}|\phi_\mathrm{FS}\rangle, \tag{4.4.1}$$

with

$$|\phi_\mathrm{FS}\rangle = \prod_{\boldsymbol{k}\in\mathrm{BZ}} \prod_{\sigma} \theta\left(\varepsilon(\boldsymbol{k}) - \mu\right) c^\dagger_{\boldsymbol{k}\sigma}|0\rangle, \tag{4.4.2}$$

where $|\phi_\mathrm{FS}\rangle$ is the Hartree-Fock type wave function of the paramagnetic state of free electrons. As is well known, the Pauli exclusion principle is adopted in the Hartree-Fock approximation. BZ denotes the first Brillouin zone, and $c^\dagger_{\boldsymbol{k}\sigma}$ is an annihilation operator of an electron with momentum $\boldsymbol{k}$ and spin σ. $\varepsilon(\boldsymbol{k})$ is the band dispersion and μ is the Fermi level of free electrons. $\theta(x)$ is a step function defined as

$$\theta(x) = \begin{cases} 1 & (x \leq 0) \\ 0 & (x > 0) \end{cases}. \tag{4.4.3}$$

$\mathcal{P}_\mathrm{G}$ is the Gutzwiller factor, which describes the on-site Coulomb repulsion [87], defined as

$$\begin{aligned} \mathcal{P}_\mathrm{G} &= \exp\left(-g\sum_i n_{i\uparrow}n_{i\downarrow}\right) \\ &= \prod_i [1-(1-e^{-g})n_{i\uparrow}n_{i\downarrow}], \end{aligned} \tag{4.4.4}$$

Here g is a variational parameter, which is rewritten as $e^{-g} \to g$ $(0 \leq g \leq 1)$ in this subsection. For $g = 0$, double occupations are prohibited. Meanwhile, for $g = 1$, electrons are free.

$|\phi_{\mathrm{FS}}\rangle$ is rewritten in a real space representation:

$$\begin{aligned}|\phi_{\mathrm{FS}}\rangle &= \prod_{\sigma}\prod_{\boldsymbol{k}\in\mathrm{BZ}}\frac{1}{\sqrt{N_{\mathrm{s}}}}\theta\left(\varepsilon(\boldsymbol{k})-\mu\right)\sum_{i}\exp\left(i\boldsymbol{k}\cdot\boldsymbol{r}_{i\sigma}\right)c^{\dagger}_{i\sigma}|0\rangle \\ &\propto \prod_{\sigma}\sum_{i_1,i_2,\cdots,i_{N_{\mathrm{e}}/2}}\exp\left(i\boldsymbol{k}_1\cdot\boldsymbol{r}_{i_1\sigma}\right)\exp\left(i\boldsymbol{k}_2\cdot\boldsymbol{r}_{i_2\sigma}\right)\cdots\exp\left(i\boldsymbol{k}_{N_{\mathrm{e}}/2}\cdot\boldsymbol{r}_{i_{N_{\mathrm{e}}/2}\sigma}\right) \\ &\qquad\times c^{\dagger}_{i_1\sigma}c^{\dagger}_{i_2\sigma}\cdots c^{\dagger}_{i_{N_{\mathrm{e}}/2}\sigma}|0\rangle, \end{aligned} \tag{4.4.5}$$

where $\boldsymbol{k}_i$ is the i^{th} wave vector of free electrons under boundary conditions, which will be specified in subsection 4.14. $\boldsymbol{r}_{j\sigma}$ denotes j^{th} electron with spin σ ($j = 1, 2, \cdots, N_{\mathrm{e}}/2$).

In the second step, one has to evaluate the energy expectation value (see Eq. (4.2.1))

$$E(\gamma) \equiv \frac{\langle\psi_\gamma|\hat{H}|\psi_\gamma\rangle}{\langle\psi_\gamma|\psi_\gamma\rangle}, \tag{4.4.6}$$

where γ denotes a set of variational parameters, which is g in this subsection. Eq. (4.4.6) can be rewritten as

$$E(\gamma) = \sum_{\boldsymbol{R}}\frac{\langle\psi_\gamma|\hat{H}|\boldsymbol{R}\rangle\langle\boldsymbol{R}|\psi_\gamma\rangle}{\langle\psi_\gamma|\psi_\gamma\rangle} = \sum_{\boldsymbol{R}}P_\gamma(\boldsymbol{R})\frac{\langle\psi_\gamma|\hat{H}|\boldsymbol{R}\rangle}{\langle\psi_\gamma|\boldsymbol{R}\rangle}, \tag{4.4.7}$$

where $\boldsymbol{R}$ represents a certain configurations of total spin-up and down electrons: $\boldsymbol{R} = \{\boldsymbol{R}_\uparrow, \boldsymbol{R}_\downarrow\}$ and $\boldsymbol{R}_\sigma = \{\boldsymbol{r}_{1\sigma}, \boldsymbol{r}_{2\sigma}, \cdots, \boldsymbol{r}_{N_{\mathrm{e}}/2\sigma}\}$. $P_\gamma(\boldsymbol{R})$ is the distribution of a configuration $\boldsymbol{R}$:

$$P_\gamma(\boldsymbol{R}) = \frac{|\langle\psi_\gamma|\boldsymbol{R}\rangle|^2}{\langle\psi_\gamma|\psi_\gamma\rangle} > 0. \tag{4.4.8}$$

The positive value of $P_\gamma(\boldsymbol{R})$ circumvents the negative sign problem unlike AFQMC. According to the Monte-Carlo method, the summation over $\boldsymbol{R}$ is replaced by the importance sampling with weight $P_\gamma(\boldsymbol{R})$, for which we employ the Metropolis algorithm (see subsection 4.3). Eq. (4.4.7) is then reduced to

$$E(\gamma) \sim \frac{1}{M}\sum_{\boldsymbol{R}\in\mathrm{MC\ sampling}}\frac{\langle\psi_\gamma|\hat{H}|\boldsymbol{R}\rangle}{\langle\psi_\gamma|\boldsymbol{R}\rangle}, \tag{4.4.9}$$

When a present configuration $\boldsymbol{R}_i$ is to be changed to a new configuration $\boldsymbol{R}_j$, the acceptance possibility is given by Eq. (4.3.5) and (4.4.8) as

$$\omega_{ij} \equiv \frac{P_\gamma(\boldsymbol{R}_j)}{P_\gamma(\boldsymbol{R}_i)} = \frac{|\langle\boldsymbol{R}_j|\psi_\gamma\rangle|^2}{|\langle\boldsymbol{R}_i|\psi_\gamma\rangle|^2}. \tag{4.4.10}$$

Using the trial wave function $|\phi_g\rangle$ defined as in Eq. (4.4.2), $\langle\boldsymbol{R}|\phi_g\rangle$ is given by

$$\langle\boldsymbol{R}|\psi_g\rangle = g^{N_{\mathrm{d}}}\det\left[D_\uparrow(\boldsymbol{R}_\uparrow)\right]\det\left[D_\downarrow(\boldsymbol{R}_\downarrow)\right], \tag{4.4.11}$$

where $\det\left[D_\sigma(\boldsymbol{R}_\sigma)\right]$ is a Slater determinant of the paramagnetic state of free electrons and N_{d} denotes the total number of double occupied sites. The i, j-element of the determinant is simply

$$[D_\sigma(\boldsymbol{R}_\sigma)]_{ij} = \exp(i\boldsymbol{k}_i \cdot \boldsymbol{r}_{j\sigma}) \equiv \varphi_\sigma(\boldsymbol{k}_i, \boldsymbol{r}_{j\sigma}), \tag{4.4.12}$$

Using Eq. (4.4.10), the acceptance possibility is then given by

$$\omega_{ij} = g^{2\delta d} \left| \frac{\det\left[D_\uparrow(\boldsymbol{R}_{j\uparrow})\right]}{\det\left[D_\uparrow(\boldsymbol{R}_{i\uparrow})\right]} \right|^2 \left| \frac{\det\left[D_\downarrow(\boldsymbol{R}_{j\downarrow})\right]}{\det\left[D_\downarrow(\boldsymbol{R}_{i\downarrow})\right]} \right|^2, \tag{4.4.13}$$

where δd denotes the change in the number of the doubly occupied sites. In the Monte-Carlo step, the single electron hopping is often considered. When the α^{th} electron with spin σ moves from $\boldsymbol{r}_{\alpha\sigma}$ to $\boldsymbol{r}_{\alpha\sigma} + \boldsymbol{\delta}$, the configuration is

$$|\cdots, \boldsymbol{r}_{\alpha\sigma}, \cdots\rangle \to |\cdots, \boldsymbol{r}_{\alpha\sigma} + \boldsymbol{\delta}, \cdots\rangle. \tag{4.4.14}$$

The acceptance possibility is then given by

$$\omega_{ij} = g^{2\delta d} \left| \frac{\det\left[D_\sigma(\cdots, \boldsymbol{r}_{\alpha\sigma} + \boldsymbol{\delta}, \cdots)\right]}{\det\left[D_\sigma(\cdots, \boldsymbol{r}_{\alpha\sigma}, \cdots)\right]} \right|^2. \tag{4.4.15}$$

Thus, the ratio of determinants is needed to evaluate ω_{ij}.

The energy expectation value is calculated as follows. In the first-quantization representation, the Hubbard Hamiltonian is rewritten as

$$\hat{H} = -\sum_\alpha \sum_\sigma \sum_{\boldsymbol{\delta}} t_{\boldsymbol{\delta}} \Delta_{\alpha\sigma}(\boldsymbol{\delta}) + U \sum_{i,j} \delta_{r_{i\uparrow}, r_{j\downarrow}}. \tag{4.4.16}$$

Here $t_{\boldsymbol{\delta}}$ is a hopping integral, and $\Delta_{\alpha\sigma}(\boldsymbol{\delta})$ is a hopping operator defined as

$$\Delta_{\alpha\sigma}(\boldsymbol{\delta})|\cdots, \boldsymbol{r}_{\alpha\sigma}, \cdots\rangle = |\cdots, \boldsymbol{r}_{\alpha\sigma} + \boldsymbol{\delta}, \cdots\rangle \tag{4.4.17}$$

where $\overline{\sigma}$ denotes the spin with the opposite sign to the spin σ. Using Eqs. (4.4.16) and (4.4.17), we have

$$\frac{\langle\psi_\gamma|\hat{H}|\boldsymbol{R}\rangle}{\langle\psi_\gamma|\boldsymbol{R}\rangle} = -\sum_i \sum_\sigma \sum_{\boldsymbol{\delta}} g^{\delta d} t_{\boldsymbol{\delta}} \frac{\det D_\sigma(\cdots, \boldsymbol{r}_{i\sigma} + \boldsymbol{\delta}, \cdots)}{\det D_\sigma(\cdots, \boldsymbol{r}_{i\sigma}, \cdots)} + UN_{\mathrm{d}}. \tag{4.4.18}$$

Same as ω_{ij}, the ratio of Slater determinants is required to evaluate the energy expectation value. The expectation value of any other observable $\hat{A}$, e.g. the momentum distribution function and structure factors, can be evaluated in a similar way with the score $\langle\psi_\gamma|\hat{A}|\boldsymbol{R}\rangle / \langle\psi_\gamma|\boldsymbol{R}\rangle$.

In order to evaluate ω_{ij} and $\langle\psi_\gamma|\hat{H}|\boldsymbol{R}\rangle / \langle\psi_\gamma|\boldsymbol{R}\rangle$, we need the ratio of determinants

$$q \equiv \frac{\det D_\sigma(\cdots, \boldsymbol{r}_{i\sigma} + \boldsymbol{\delta}, \cdots)}{\det D_\sigma(\cdots, \boldsymbol{r}_{i\sigma}, \cdots)}. \tag{4.4.19}$$

The Leibniz formula for determinants gives a $\mathcal{O}\left((N_\mathrm{e}/2)!\right)$ time complexity, which is very high in the repeated calculation of the VMC method. In ref. [72], it has been proposed that the most effective way to handle this wave function is to calculate the inverse of the matrices D_σ (Eq. (4.4.12)). This inverse is needed to compute the acceptance possibility ω_{ij} (Eq. (4.4.10)) and the variational energy. Since only one particle is being moved, only one column of the matrix D_σ will change, and the required ratio of wave functions is easily evaluated. Since D_σ^{-1} is proportional to the matrix of cofactors, the ratio of determinants is

$$q = \sum_{i=1}^{N_\mathrm{e}/2} [D_\sigma^{-1}]_{i\alpha}\ \varphi_\sigma(\boldsymbol{k}_i, \boldsymbol{r}_{\alpha\sigma} + \boldsymbol{\delta}). \tag{4.4.20}$$

If the move of the single electron is accepted, all of the elements of D_σ^{-1} need to be changed.

$$[D_\sigma^{-1}]_{ji}^{(n+1)} = \begin{cases} [D_\sigma^{-1}]_{ji}^{(n)}/q^{(n)} & (i = \alpha) \\ [D_\sigma^{-1}]_{ji}^{(n)} - [D_\sigma^{-1}]_{j\alpha}^{(n)} \displaystyle\sum_{l=1}^{N_\mathrm{e}/2} \frac{[D_\sigma^{-1}]_{lj}^{(n)} \varphi_\sigma(\boldsymbol{k}_l, \boldsymbol{r}_{\alpha\sigma} + \boldsymbol{\delta})}{q^{(n)}} & (i \neq \alpha) \end{cases}. \tag{4.4.21}$$

This method gives a $\mathcal{O}\left(N_\mathrm{e}/2\right)^2$ time complexity, which is quite low compared to that of the Leibniz formula.

We demonstrate the easy example of the Gutzwiller's wave function (Eq. (4.4.1)) in the two-site Hubbard model for two electrons. The absolute values of inner products $\langle x|\phi_g\rangle$ are $1, g, g, 1$ for $|x\rangle = |\uparrow, \downarrow\rangle, |\uparrow\downarrow, 0\rangle, |0, \uparrow\downarrow\rangle, |\downarrow, \uparrow\rangle$, respectively. Substitution the above equations in Eq. (4.4.7) leads to

$$E(g) = U - \frac{4tg + U}{1 + g^2}. \tag{4.4.22}$$

The variational energy $E(g)$ is minimized at

$$g = -\frac{U}{4t} + \sqrt{1 + \left(\frac{U}{4t}\right)^2} \equiv g^{(\mathrm{opt})}. \tag{4.4.23}$$

Substituting this optimized value $g^{(\mathrm{opt})}$ for Eq. (4.4.22), the exact energy of the ground state can be reproduced. Taking the limit $U/4t \to \infty$ (0), $g^{(\mathrm{opt})}$ converges to 0 (1). These results are consistent with intuitive pictures. The variational method can reduce the computational cost efficiently since we do not have to solve eigenvalue problems.

In small-scale systems, the trial-wave function can reach the exact solution. Meanwhile, large-scale systems are usually unsolvable due to a huge number of configurations, so that many variational parameters are required to describe the ground state of the systems accurately. The more elaborate variational wave functions are discussed later.

4.5 Variational wave functions

The “accurate” variational wave function is expected to bear the following properties:

1. Unified form which can describe several different phases by using many variables,
2. Treatment of various many-body correlations beyond the mean-field theory,
3. Restoring symmetry which is broken in the mean-field theory.

The development of multi-variable optimization methods enables the treatment of wave functions with many variational parameters, which can provide the above properties.

The generalized form of wave functions in this thesis is

$$|\psi\rangle = \mathcal{P}\mathcal{L}|\phi\rangle, \tag{4.5.1}$$

where $|\phi\rangle$ is a Hartree-Fock-Bogoliubov type function called “one-body part”, $\mathcal{L}$ is the quantum number projector controlling symmetries of wave function [88,89], and $\mathcal{P}$ is the Gutzwiller-Jastrow factor describing many-body correlations [87, 90]. Here, we employ $\mathcal{P}$ which is commutable with $\mathcal{L}$ ($\mathcal{L}\mathcal{P} = \mathcal{L}\mathcal{P}$) in order to preserve symmetries of $|\psi\rangle$.

4.6 One-body part

The mean-field Slater determinant is usually employed as the one-body part. In this subsection, we show one-body parts for various states; namely, the superconducting state and antiferromaginetic (AFM) state, state with AFM and superconducting orders, respectively. Further, the formalism for multi-orbital systems is also given.

4.6.1 BCS wave functions

From Eq. (2.1.27) in section 2.1, the BCS wave function is given by

$$|\phi_{\mathrm{BCS}}\rangle = \prod_{\boldsymbol{k}} \left(1 + \varphi(\boldsymbol{k}) c^{\dagger}_{\boldsymbol{k}\uparrow} c^{\dagger}_{-\boldsymbol{k}\downarrow}\right) |0\rangle, \tag{4.6.1}$$

with

$$\varphi(\boldsymbol{k}) = \frac{\Delta_{\mathrm{SC}}(\boldsymbol{k})}{\xi(\boldsymbol{k}) + \sqrt{\xi(\boldsymbol{k})^2 + \Delta_{\mathrm{SC}}(\boldsymbol{k})^2}}, \tag{4.6.2}$$

where $\xi(\boldsymbol{k}) = \varepsilon(\boldsymbol{k}) - \mu$, μ is the chemical potential and $\Delta_{\mathrm{SC}}(\boldsymbol{k})$ is the superconducting gap. Since the number of electrons N_{e} is fixed in VMC calculations, the BCS wave function [91] is rewritten as

$$|\phi_{\mathrm{BCS}}\rangle = \left(\sum_{\boldsymbol{k}\in\mathrm{BZ}} \varphi(\boldsymbol{k}) c^{\dagger}_{\boldsymbol{k}\uparrow} c^{\dagger}_{-\boldsymbol{k}\downarrow} \right)^{N_{\mathrm{e}}/2} |0\rangle. \tag{4.6.3}$$

For actual calculations, we employ the following real space representation:

$$|\phi_{\text{pair}}\rangle = \left(\sum_{i,j=1}^{N_{\text{s}}} f_{ij} c_{i\uparrow}^{\dagger} c_{j\downarrow}^{\dagger}\right)^{N_{\text{e}}/2} |0\rangle. \tag{4.6.4}$$

In this case, the coefficient f_{ij} is given by

$$f_{ij} = \frac{1}{N_{\text{s}}} \sum_{\boldsymbol{k}\in\text{BZ}} \varphi(\boldsymbol{k}) e^{i\boldsymbol{k}\cdot(\boldsymbol{r}_i - \boldsymbol{r}_j)}. \tag{4.6.5}$$

The one body part $|\phi_{\text{pair}}\rangle$ is called the "generalized pairing function". The merit of this formalism is discussed later.

4.6.2 AFM ordered states

Here, we consider the AFM order,

$$\begin{aligned}\hat{H}_{\text{MF}} &= \sum_{\sigma} \sum_{\boldsymbol{k}\in\text{BZ}} \varepsilon(\boldsymbol{k}) c_{\boldsymbol{k}\sigma}^{\dagger} c_{\boldsymbol{k}\sigma} + \sum_{i} \Delta_{\text{AF}} \exp(i\boldsymbol{Q}\cdot\boldsymbol{r}_i)(c_{i\uparrow}^{\dagger} c_{i\uparrow} - c_{i\downarrow}^{\dagger} c_{i\downarrow}) + \text{H.c.} \\ &= \sum_{\sigma} \sum_{\boldsymbol{k}\in\text{AFBZ}} \left(c_{\boldsymbol{k}\sigma}^{\dagger}, c_{\boldsymbol{k}+\boldsymbol{Q}\sigma}^{\dagger}\right) \begin{pmatrix} \xi(\boldsymbol{k}) & \sigma\Delta_{\text{AF}} \\ \sigma\Delta_{\text{AF}} & \xi(\boldsymbol{k}+\boldsymbol{Q}) \end{pmatrix} \begin{pmatrix} c_{\boldsymbol{k}\sigma} \\ c_{\boldsymbol{k}+\boldsymbol{Q}\sigma} \end{pmatrix},\end{aligned} \tag{4.6.6}$$

where AFBZ denotes the folded AFM Brillouin zone and Δ_{AF} is the AFM order parameter, $\boldsymbol{Q}$ is the AFM nesting vector. Here we assume the ordered moment to be aligned in the z direction. After diagonalizing $\hat{H}_{\text{MF}}$, the band dispersion is given by

$$\begin{cases} \varepsilon^{a}(\boldsymbol{k}) = \xi_2(\boldsymbol{k}) - \sqrt{\xi_1(\boldsymbol{k})^2 + \Delta_{\text{AF}}^2} \\ \varepsilon^{b}(\boldsymbol{k}) = \xi_2(\boldsymbol{k}) + \sqrt{\xi_1(\boldsymbol{k})^2 + \Delta_{\text{AF}}^2} \end{cases} (\boldsymbol{k} \in \text{AFBZ}), \tag{4.6.7}$$

with $\xi_1(\boldsymbol{k}) = (\varepsilon(\boldsymbol{k}) - \varepsilon(\boldsymbol{k}+\boldsymbol{Q}))/2$ and $\xi_2(\boldsymbol{k}) = (\varepsilon(\boldsymbol{k}) + \varepsilon(\boldsymbol{k}+\boldsymbol{Q}))/2$. The operators $\{a_{\boldsymbol{k}\sigma}^{\dagger}, b_{\boldsymbol{k}\sigma}^{\dagger}\}$ ($\{a_{\boldsymbol{k}\sigma}, b_{\boldsymbol{k}\sigma}\}$) are creation (annihilation) operators for the AFM quasiparticles transformed from $c_{\boldsymbol{k}\sigma}^{\dagger}$ ($c_{\boldsymbol{k}\sigma}$) as follows:

$$\begin{cases} a_{\boldsymbol{k}\sigma}^{\dagger} = u_{\boldsymbol{k}} c_{\boldsymbol{k}\sigma}^{\dagger} + \sigma v_{\boldsymbol{k}} c_{\boldsymbol{k}+\boldsymbol{Q}\sigma}^{\dagger} \\ b_{\boldsymbol{k}\sigma}^{\dagger} = -\sigma v_{\boldsymbol{k}} c_{\boldsymbol{k}\sigma}^{\dagger} + u_{\boldsymbol{k}} c_{\boldsymbol{k}+\boldsymbol{Q}\sigma}^{\dagger} \end{cases} (\boldsymbol{k} \in \text{AFBZ}), \tag{4.6.8}$$

with

$$u_{\boldsymbol{k}}(v_{\boldsymbol{k}}) = \left[\frac{1}{2}\left(1 - (+)\frac{\xi_1(\boldsymbol{k})}{\sqrt{\xi_1(\boldsymbol{k})^2 + \Delta_{\text{AF}}^2}}\right)\right]^{1/2}.. \tag{4.6.9}$$

$u_{\boldsymbol{k}}$ and $v_{\boldsymbol{k}}$ are assumed to satisfy the following relations:

$$u_{\boldsymbol{k}}^2 + v_{\boldsymbol{k}}^2 = 1, \quad u_{\boldsymbol{k}} = u_{-\boldsymbol{k}}, \quad v_{\boldsymbol{k}} = v_{-\boldsymbol{k}}. \tag{4.6.10}$$

In the hole-doped case, the wave function is then given by

$$\begin{aligned}|\phi_{\mathrm{AFM}}\rangle &= \prod_{\boldsymbol{k}\in\mathrm{AFBZ}}\prod_{\sigma}\theta\left(\varepsilon^a(\boldsymbol{k})-\mu\right)a^\dagger_{\boldsymbol{k}\sigma}|0\rangle\\ &\propto \prod_{\boldsymbol{k}\in\mathrm{AFBZ}}\prod_{\sigma}\theta\left(\varepsilon^a(\boldsymbol{k})-\mu\right)\sum_i\left(u_k-\sigma v_k\exp(i\boldsymbol{Q}\cdot\boldsymbol{r}_i)\right)\exp\left(i\boldsymbol{k}\cdot\boldsymbol{r}_i\right)c^\dagger_{i\sigma}|0\rangle.\end{aligned} \tag{4.6.11}$$

The i,j element of the Slater determinant (Eq. (4.4.12)) is then given by

$$\varphi_\sigma(\boldsymbol{k}_i,\boldsymbol{r}_{j\sigma})=\left(u_{k_i}-\sigma v_{k_i}\exp(i\boldsymbol{Q}\cdot\boldsymbol{r}_j)\right)\exp\left(i\boldsymbol{k}_i\cdot\boldsymbol{r}_j\right) \tag{4.6.12}$$

In the limit $\Delta_{\mathrm{AF}}\to 0$, the operators $a^\dagger_{\boldsymbol{k}\sigma}$ and $b^\dagger_{\boldsymbol{k}\sigma}$ are reduced to $c^\dagger_{\boldsymbol{k}\sigma}$ and $c^\dagger_{\boldsymbol{k}+\boldsymbol{Q}\sigma}$, respectively. Then, the wave function $|\phi_{\mathrm{AF}}\rangle$ becomes the Slater determinant. The summation over all possible AFM orders $\boldsymbol{Q}$ would improve the accuracy of the one-body part. However, such an expansion increases computational costs due to the large number of variational parameters. Thus, the single plausible nesting vector $\boldsymbol{Q}$ is taken in this thesis.

4.6.3 States with AFM and superconducting orders

A wave function with AFM and superconducting orders can be introduced as follows [92]. Here, we start from the mean-field Hamiltonian,

$$\begin{aligned}\hat{H}_{\mathrm{MF}} = \sum_{\boldsymbol{k}\in\mathrm{AFBZ}}&\Big[\varepsilon^a(\boldsymbol{k})\left(a^\dagger_{\boldsymbol{k}\uparrow}a_{\boldsymbol{k}\uparrow}+a^\dagger_{\boldsymbol{k}\downarrow}a_{\boldsymbol{k}\downarrow}\right)+\Delta^a_{\mathrm{SC}}(\boldsymbol{k})\left(a^\dagger_{\boldsymbol{k}\uparrow}a_{-\boldsymbol{k}\downarrow}+a^\dagger_{-\boldsymbol{k}\downarrow}a_{\boldsymbol{k}\uparrow}\right)\\ &+\varepsilon^b(\boldsymbol{k})\left(b^\dagger_{\boldsymbol{k}\uparrow}b_{\boldsymbol{k}\uparrow}+b^\dagger_{\boldsymbol{k}\downarrow}b_{\boldsymbol{k}\downarrow}\right)+\Delta^b_{\mathrm{SC}}(\boldsymbol{k})\left(b^\dagger_{\boldsymbol{k}\uparrow}b_{-\boldsymbol{k}\downarrow}+b^\dagger_{-\boldsymbol{k}\downarrow}b_{\boldsymbol{k}\uparrow}\right)\Big]-\mu\sum_{i,\sigma}c^\dagger_{i\sigma}c_{i\sigma},\end{aligned} \tag{4.6.13}$$

where $\Delta^a_{\mathrm{SC}}(\boldsymbol{k})$and $\Delta^b_{\mathrm{SC}}(\boldsymbol{k})$ are superconducting order parameters, and μ is the chemical potential. The definitions of operators $\{a^\dagger_{\boldsymbol{k}\sigma},b^\dagger_{\boldsymbol{k}\sigma}\}$ ($\{a_{\boldsymbol{k}\sigma},b_{\boldsymbol{k}\sigma}\}$) are the same as Eq. (4.6.8).

Using eigenfunctions of $\hat{H}_{\mathrm{MF}}$, the wave function is obtained as

$$|\phi_{\mathrm{AF+SC}}\rangle=\left[\sum_{\boldsymbol{k}\in\mathrm{AFBZ}}\left(\varphi^a(\boldsymbol{k})a^\dagger_{\boldsymbol{k}\uparrow}a^\dagger_{-\boldsymbol{k}\downarrow}+\varphi^b(\boldsymbol{k})b^\dagger_{\boldsymbol{k}\uparrow}b^\dagger_{-\boldsymbol{k}\downarrow}\right)\right]^{N_{\mathrm{e}}/2}|0\rangle, \tag{4.6.14}$$

with

$$\begin{cases}\varphi^a(\boldsymbol{k})=\dfrac{\Delta^a_{\mathrm{SC}}(\boldsymbol{k})}{(\varepsilon^a(\boldsymbol{k})-\mu)+\sqrt{(\varepsilon^a(\boldsymbol{k})-\mu)^2+\Delta^a_{\mathrm{SC}}(\boldsymbol{k})^2}}\\ \varphi^b(\boldsymbol{k})=\dfrac{\Delta^b_{\mathrm{SC}}(\boldsymbol{k})}{(\varepsilon^b(\boldsymbol{k})-\mu)+\sqrt{(\varepsilon^b(\boldsymbol{k})-\mu)^2+\Delta^b_{\mathrm{SC}}(\boldsymbol{k})^2}}\end{cases}. \tag{4.6.15}$$

In the limit $\Delta_{\mathrm{AF}}\to 0$, the operators $a^\dagger_{\boldsymbol{k}\sigma}$ and $b^\dagger_{\boldsymbol{k}\sigma}$ are reduced to $c^\dagger_{\boldsymbol{k}\sigma}$ and $c^\dagger_{\boldsymbol{k}+\boldsymbol{Q}\sigma}$, respectively. Then, the wave function $|\phi_{\mathrm{AF+SC}}\rangle$ is reduced to the conventional BCS wave function. On the other hand, in the limit $\Delta^a_{\mathrm{SC}}(\boldsymbol{k})(\Delta^b_{\mathrm{SC}}(\boldsymbol{k})) \to 0$, $\varphi^a(\boldsymbol{k})(\varphi^a(\boldsymbol{k}))$ converges to zero if $\varepsilon^{a(b)}(\boldsymbol{k}) > \mu$ and otherwise diverges. Thus, the states only below the chemical potential are occupied by the AFM quasiparticles and $|\phi_{\mathrm{AF+SC}}\rangle$ is reduced to the normal AFM mean-field wave function.

By replacing the operators for the AFM quasiparticles $\{a^\dagger_{\boldsymbol{k}\sigma}, b^\dagger_{\boldsymbol{k}\sigma}\}$ with that for the electron $\{c^\dagger_{\boldsymbol{k}\sigma}\}$ in Eq. (4.6.14), the superconducting and AFM terms are represented explicitly. Using Eqs. (4.6.8) and (4.6.14), (4.6.10), we have

$$\begin{aligned}|\phi_{\mathrm{AF+SC}}\rangle = \Bigg[\sum_{\boldsymbol{k}\in\mathrm{AFBZ}} \Big\{ &\left(u^2_{\boldsymbol{k}}\varphi^a(\boldsymbol{k}) - v^2_{\boldsymbol{k}}\varphi^b(\boldsymbol{k})\right) c^\dagger_{\boldsymbol{k}\uparrow}c^\dagger_{-\boldsymbol{k}\downarrow} \\ &+ \left(-v^2_{\boldsymbol{k}}\varphi^a(\boldsymbol{k}) + u^2_{\boldsymbol{k}}\varphi^b(\boldsymbol{k})\right) c^\dagger_{\boldsymbol{k}+\boldsymbol{Q}\uparrow}c^\dagger_{-\boldsymbol{k}-\boldsymbol{Q}\downarrow} \\ &+ \left(\varphi^a(\boldsymbol{k}) + \varphi^b(\boldsymbol{k})\right) u_{\boldsymbol{k}}v_{\boldsymbol{k}} \left(c^\dagger_{\boldsymbol{k}+\boldsymbol{Q}\uparrow}c^\dagger_{-\boldsymbol{k}\downarrow} - c^\dagger_{\boldsymbol{k}\uparrow}c^\dagger_{-\boldsymbol{k}-\boldsymbol{Q}\downarrow}\right)\Big\}\Bigg]^{N_{\mathrm{e}}/2} |0\rangle, \end{aligned} \quad (4.6.16)$$

where $\varphi^a(\boldsymbol{k})$ and $\varphi^b(\boldsymbol{k})$ are the variational parameters with the condition

$$\varphi^a(-\boldsymbol{k}) = \varphi^a(\boldsymbol{k}), \quad \varphi^b(-\boldsymbol{k}) = \varphi^b(\boldsymbol{k}). \quad (4.6.17)$$

Then, $u_{\boldsymbol{k}}, v_{\boldsymbol{k}}, \varphi^a(\boldsymbol{k}), \varphi^b(\boldsymbol{k})$ are rewritten as

$$\begin{cases} u_{\boldsymbol{k}} = \cos\theta_{\boldsymbol{k}}, \quad v_{\boldsymbol{k}} = \sin\theta_{\boldsymbol{k}} \\ A(\boldsymbol{k}) = \cos^2\theta_{\boldsymbol{k}}\varphi^a(\boldsymbol{k}) - \sin^2\theta_{\boldsymbol{k}}\varphi^b(\boldsymbol{k}) \\ B(\boldsymbol{k}) = -\sin^2\theta_{\boldsymbol{k}}\varphi^a(\boldsymbol{k}) + \cos^2\theta_{\boldsymbol{k}}\varphi^b(\boldsymbol{k}) \end{cases} . \quad (4.6.18)$$

The coefficient of the third term in Eq. (4.6.16) is given by

$$\left(\varphi^a(\boldsymbol{k}) + \varphi^b(\boldsymbol{k})\right) u_{\boldsymbol{k}}v_{\boldsymbol{k}} = \frac{1}{2}\left(A(\boldsymbol{k}) + B(\boldsymbol{k})\right)\tan 2\theta_{\boldsymbol{k}} = C(\boldsymbol{k}). \quad (4.6.19)$$

Thus, the parameters $u_{\boldsymbol{k}}, v_{\boldsymbol{k}}, \varphi^a(\boldsymbol{k}), \varphi^b(\boldsymbol{k})$ are mapped to the new parameters $A(\boldsymbol{k}), B(\boldsymbol{k})$ and $C(\boldsymbol{k})$. $A(\boldsymbol{k})$ ($B(\boldsymbol{k})$) corresponds to singlet pairing in (out) the AFBZ. Thus, we define the following parameters

$$\begin{cases} \varphi^{(1)}(\boldsymbol{k}) = A(\boldsymbol{k}), \quad \varphi^{(1)}(\boldsymbol{k}+\boldsymbol{Q}) = B(\boldsymbol{k}) \\ \varphi^{(2)}(\boldsymbol{k}) = C(\boldsymbol{k}) \end{cases} \quad (\boldsymbol{k} \in \mathrm{AFBZ}). \quad (4.6.20)$$

The wave function is then rewritten as

$$|\phi_{\mathrm{pair}}\rangle = \Bigg[\sum_{\boldsymbol{k}\in\mathrm{BZ}} \varphi^{(1)}(\boldsymbol{k})c^\dagger_{\boldsymbol{k}\uparrow}c^\dagger_{-\boldsymbol{k}\downarrow} + \sum_{\boldsymbol{k}\in\mathrm{AFBZ}} \varphi^{(2)}(\boldsymbol{k})\left(c^\dagger_{\boldsymbol{k}+\boldsymbol{Q}\uparrow}c^\dagger_{-\boldsymbol{k}\downarrow} - c^\dagger_{\boldsymbol{k}\uparrow}c^\dagger_{-\boldsymbol{k}-\boldsymbol{Q}\downarrow}\right)\Bigg]^{N_{\mathrm{e}}/2} |0\rangle, \quad (4.6.21)$$

with

$$\varphi^{(1)}(-\boldsymbol{k}) = \varphi^{(1)}(\boldsymbol{k}), \quad \varphi^{(2)}(-\boldsymbol{k}) = \varphi^{(2)}(\boldsymbol{k}). \tag{4.6.22}$$

The first and second terms in Eq. (4.6.21) mainly come from the superconducting spin singlet state and AFM state, respectively. The second term also contains the spin triplet state, which breaks the spin rotational symmetry.

In the form of the generalized pairing function, f_{ij} is given by

$$f_{ij} = \frac{1}{N_{\mathrm{s}}} \sum_{\boldsymbol{k}\in\mathrm{BZ}} \varphi^{(1)}(\boldsymbol{k}) e^{i\boldsymbol{k}\cdot(\boldsymbol{r}_i-\boldsymbol{r}_j)} + \frac{1}{N_{\mathrm{s}}} \sum_{\boldsymbol{k}\in\mathrm{AFBZ}} \varphi^{(2)}(\boldsymbol{k}) e^{i\boldsymbol{k}\cdot(\boldsymbol{r}_i-\boldsymbol{r}_j)} \left(e^{i\boldsymbol{Q}\cdot\boldsymbol{r}_i} - e^{-i\boldsymbol{Q}\cdot\boldsymbol{r}_j}\right). \tag{4.6.23}$$

At most, f_{ij} have N_{s}^2 independent variational parameters, which can give rise to high computational costs. Thus, one had better allow f_{ij} to have a sublattice structure so as to reduce the cost. The large number of variational parameters f_{ij} can represent various ordering states such as paramagnetic metals, AFM ordered states, charge ordered states, spin liquid, and superconducting states within an unified form of $|\phi_{\mathrm{pair}}\rangle$.

4.6.4 Multi-orbital BCS wave functions

The multi-orbital kinetic term is given by

$$\hat{H}_{\mathrm{kin}} = \sum_{\boldsymbol{k},\sigma} \sum_{\alpha,\beta} \xi_{\alpha\beta}(\boldsymbol{k}) c^{\dagger}_{\boldsymbol{k}\alpha\sigma} c_{\boldsymbol{k}\beta\sigma}. \tag{4.6.24}$$

Here $c^{\dagger}_{\boldsymbol{k}\alpha\sigma}/c_{\boldsymbol{k}\alpha\sigma}$ creates/annihilates a fermion with momentum $\boldsymbol{k}$ and spin $\sigma(=\uparrow,\downarrow)$, α^{th} orbital $(\alpha = 1, 2, \cdots, M)$. $\xi_{\alpha\beta}(\boldsymbol{k})$ is given by

$$\xi_{\alpha\beta}(\boldsymbol{k}) = -\sum_{ij} (t_{i\alpha,j\beta} - \mu) \exp\left(-i\boldsymbol{k}\cdot(\boldsymbol{r}_i - \boldsymbol{r}_j)\right). \tag{4.6.25}$$

where $t_{i\alpha,j\beta}$ denotes the hopping integral between the α^{th} orbital of site i and the β^{th} orbital of site j. μ is the chemical potential.

At the beginning, one diagonalizes this kinetic term by using a unitary transformation,

$$d_{\boldsymbol{k}p\sigma} = \Lambda_{\boldsymbol{k};p\alpha} c_{\boldsymbol{k}\alpha\sigma}, \tag{4.6.26}$$

$$d^{\dagger}_{\boldsymbol{k}p\sigma} = \Lambda^{*}_{\boldsymbol{k};\alpha p} c^{\dagger}_{\boldsymbol{k}\alpha\sigma}. \tag{4.6.27}$$

Here $d^{\dagger}_{\boldsymbol{k}p\sigma}/d_{\boldsymbol{k}p\sigma}$ creates/annihilates a fermion with momentum $\boldsymbol{k}$ and spin $\sigma(=\uparrow,\downarrow)$, p^{th} band $(p = 1, 2, \cdots, M)$. The kinetic term is rewritten as

$$\hat{H}_{\mathrm{kin}} = \sum_{\boldsymbol{k},\sigma} \sum_{p} \lambda_p(\boldsymbol{k}) d^{\dagger}_{\boldsymbol{k}p\sigma} d_{\boldsymbol{k}p\sigma}, \tag{4.6.28}$$

where $\lambda_p(\boldsymbol{k})$ is the band dispersion of the p^{th} band measured from the chemical potential. The multi-orbital BCS-type Hamiltonian is then given by

$$\hat{H}_{\mathrm{BCS}} = \sum_{\boldsymbol{k}} \left(\boldsymbol{d}^{\dagger}_{\boldsymbol{k}\uparrow}, \boldsymbol{d}_{-\boldsymbol{k}\downarrow}\right) \begin{pmatrix} \mathcal{E}(\boldsymbol{k}) & \Delta(\boldsymbol{k}) \\ \Delta^{\dagger}(\boldsymbol{k}) & -\mathcal{E}(\boldsymbol{k}) \end{pmatrix} \begin{pmatrix} \boldsymbol{d}_{\boldsymbol{k}\uparrow} \\ \boldsymbol{d}^{\dagger}_{-\boldsymbol{k}\downarrow} \end{pmatrix}, \tag{4.6.29}$$

with

$$\boldsymbol{d}^{\dagger}_{\boldsymbol{k}\uparrow} = \left(d^{\dagger}_{\boldsymbol{k}1\uparrow}, d^{\dagger}_{\boldsymbol{k}2\uparrow}, \cdots, d^{\dagger}_{\boldsymbol{k}M\uparrow}\right), \tag{4.6.30}$$

$$\boldsymbol{d}_{-\boldsymbol{k}\downarrow} = \left(d_{-\boldsymbol{k}1\downarrow}, d_{-\boldsymbol{k}2\downarrow}, \cdots, d_{-\boldsymbol{k}M\downarrow}\right), \tag{4.6.31}$$

$$\boldsymbol{d}_{\boldsymbol{k}\uparrow} = \left(d_{\boldsymbol{k}1\uparrow}, d_{\boldsymbol{k}2\uparrow}, \cdots, d_{\boldsymbol{k}M\uparrow}\right)^{\mathrm{T}}, \tag{4.6.32}$$

$$\boldsymbol{d}^{\dagger}_{-\boldsymbol{k}\downarrow} = \left(d^{\dagger}_{-\boldsymbol{k}1\downarrow}, d^{\dagger}_{-\boldsymbol{k}2\downarrow}, \cdots, d^{\dagger}_{-\boldsymbol{k}M\downarrow}\right)^{\mathrm{T}}, \tag{4.6.33}$$

where T means transpose. $\mathcal{E}(\boldsymbol{k})$ and $\Delta(\boldsymbol{k})$ are $M \times M$ matrices describing the kinetic terms and superconducting order parameters, respectively. $\mathcal{E}(\boldsymbol{k})$ is defined as

$$[\mathcal{E}(\boldsymbol{k})]_{pq} = \lambda_p(\boldsymbol{k})\delta_{pq}, \tag{4.6.34}$$

where δ_{pq} is the Kronecker delta. The BCS Hamiltonian is diagonalized by using the Bogoliubov-Valatin transformation matrix Λ_{SC}. The $2M \times 2M$ transformation matrix Λ_{SC} is divided into $M \times M$ matrices A, B, C, D as follows:

$$\Lambda_{\mathrm{SC}}(\boldsymbol{k}) = \begin{pmatrix} A(\boldsymbol{k}) & B(\boldsymbol{k}) \\ C(\boldsymbol{k}) & D(\boldsymbol{k}) \end{pmatrix}, \quad \Lambda^{\dagger}_{\mathrm{SC}}(\boldsymbol{k}) = \begin{pmatrix} A^{\dagger}(\boldsymbol{k}) & C^{\dagger}(\boldsymbol{k}) \\ B^{\dagger}(\boldsymbol{k}) & D^{\dagger}(\boldsymbol{k}) \end{pmatrix}. \tag{4.6.35}$$

These matrices are obtained from the exact diagonalization. The diagonalized BCS Hamiltonian is given by

$$\hat{H}_{\mathrm{BCS}} = \sum_{\boldsymbol{k}} \left(\gamma^{\dagger}_{\boldsymbol{k}\uparrow}, \gamma_{-\boldsymbol{k}\downarrow}\right) \begin{pmatrix} \tilde{\mathcal{E}}(\boldsymbol{k}) & 0 \\ 0 & -\tilde{\mathcal{E}}(\boldsymbol{k}) \end{pmatrix} \begin{pmatrix} \gamma_{\boldsymbol{k}\uparrow} \\ \gamma^{\dagger}_{-\boldsymbol{k}\downarrow} \end{pmatrix}. \tag{4.6.36}$$

$\tilde{\mathcal{E}}(\boldsymbol{k})$ denotes the diagonal matrix with eigenvalues E

$$[\tilde{\mathcal{E}}(\boldsymbol{k})]_{\mu\nu} = E_{\mu}(\boldsymbol{k})\delta_{\mu\nu} \quad (E_1 \leq E_2 \leq \cdots \leq E_{2M}). \tag{4.6.37}$$

where $\mu.\nu$ are the band indexes. The new operators $\gamma^{(\dagger)}_{\boldsymbol{k}\mu\sigma}$ satisfy the anti-communication relations of fermions and generate the elementary excitations (quasi-particles) of the system. $\gamma^{(\dagger)}_{\boldsymbol{k}\mu\sigma}$ is given by

$$\gamma_{\boldsymbol{k}\mu\uparrow} = A_{\mu p}(\boldsymbol{k})d_{\boldsymbol{k}p\uparrow} + B_{\mu p}(\boldsymbol{k})d^{\dagger}_{-\boldsymbol{k}p\downarrow}, \tag{4.6.38}$$

$$\gamma^{\dagger}_{-\boldsymbol{k}\mu\downarrow} = C_{\mu p}(\boldsymbol{k})d_{\boldsymbol{k}p\uparrow} + D_{\mu p}(\boldsymbol{k})d^{\dagger}_{-\boldsymbol{k}p\downarrow}. \tag{4.6.39}$$

The ground state of the superconducting state is obtained by creating all negative energy states ($\gamma_{\mu}{}^{\dagger}$) and annihilating all positive energy states ($\gamma_{\overline{\mu}}$) on the vacuum state, $|\phi_{\mathrm{BCS}}\rangle = \prod_{\mu,\boldsymbol{k}} \gamma_{\overline{\mu},\boldsymbol{k}}\gamma_{\mu,\boldsymbol{k}}{}^{\dagger}|0\rangle$ where $E_{\overline{\mu}} = -E_{\mu} \geq 0$. Thus, the multi-orbital BCS wave function has the form

$$\begin{aligned}\prod_{\boldsymbol{k},\mu}\gamma_{-\boldsymbol{k}\bar{\mu}\downarrow}\gamma_{\boldsymbol{k}\mu\uparrow}{}^{\dagger}|0\rangle &= \prod_{\boldsymbol{k},\mu}\sum_{pq}\left(C^{*}_{\bar{\mu}p}(\boldsymbol{k})d^{\dagger}_{\boldsymbol{k}p\uparrow}+D^{*}_{\bar{\mu}p}(\boldsymbol{k})d_{-\boldsymbol{k}p\downarrow}\right)\\ &\qquad\times\left(A_{\mu q}(\boldsymbol{k})d_{\boldsymbol{k}q\uparrow}+B_{\mu q}(\boldsymbol{k})d^{\dagger}_{-\boldsymbol{k}q\downarrow}\right)|0\rangle\\ &= \prod_{\alpha,\boldsymbol{k}}\sum_{pq}\left(C^{*}_{\bar{\mu}p}(\boldsymbol{k})B_{\mu q}(\boldsymbol{k})d^{\dagger}_{\boldsymbol{k}p\uparrow}d^{\dagger}_{-\boldsymbol{k}q\downarrow}+D^{*}_{\bar{\mu}p}(\boldsymbol{k})B_{\mu q}(\boldsymbol{k})\delta_{pq}\right)|0\rangle\\ &\propto \prod_{\boldsymbol{k}}\left(1+\sum_{\mu,pq}\frac{B_{\mu p}(\boldsymbol{k})C^{*}_{\bar{\mu}q}(\boldsymbol{k})}{\sum_{p'}B_{\mu p'}(\boldsymbol{k})D^{*}_{\bar{\mu}p'}(\boldsymbol{k})}c^{\dagger}_{\boldsymbol{k}p\uparrow}c^{\dagger}_{-\boldsymbol{k}q\downarrow}\right)|0\rangle,\end{aligned}$$

This wave function is rewritten as

$$|\phi^{*}_{\mathrm{pair}}\rangle = \left(\sum_{\boldsymbol{k}\in\mathrm{BZ}}\sum_{pq}\varphi_{pq}(\boldsymbol{k})d^{\dagger}_{\boldsymbol{k}p\uparrow}d^{\dagger}_{-\boldsymbol{k}q\downarrow}\right)^{N_{\mathrm{e}}/2}|0\rangle, \tag{4.6.40}$$

with

$$\varphi_{pq}(\boldsymbol{k}) = \sum_{\mu}\frac{B_{\mu p}(\boldsymbol{k})C^{*}_{\bar{\mu}q}(\boldsymbol{k})}{\sum_{p'}B_{\mu p'}(\boldsymbol{k})D^{*}_{\bar{\mu}p'}(\boldsymbol{k})}. \tag{4.6.41}$$

$|\phi^{*}_{\mathrm{pair}}\rangle$ is the generalized multi-orbital pairing function for the intra and inter orbital spin-singlet states. By using transformation (Eqs. (4.6.26) and (4.6.27)), the generalized multi-orbital pairing function is rewritten as

$$|\phi^{*}_{\mathrm{pair}}\rangle = \left(\sum_{\boldsymbol{k}\in\mathrm{BZ}}\sum_{\alpha\beta}\tilde{\varphi}_{\alpha\beta}(\boldsymbol{k})c^{\dagger}_{\boldsymbol{k}\alpha\uparrow}c^{\dagger}_{-\boldsymbol{k}\beta\downarrow}\right)^{N_{\mathrm{e}}/2}|0\rangle, \tag{4.6.42}$$

with

$$\tilde{\varphi}_{\alpha\beta}(\boldsymbol{k}) = \sum_{pq}[\Lambda^{\dagger}_{\boldsymbol{k}}]_{p\alpha}[\Lambda^{\dagger}_{-\boldsymbol{k}}]_{q\beta}\varphi_{pq}(\boldsymbol{k}). \tag{4.6.43}$$

4.6.5 Inner products of the generalized pair function and real space configuration

The inner product of the generalized pair function and real space configuration $\langle x|\phi_{\mathrm{pair}}\rangle$ is required in the VMC calculation. We recall the real space configuration $|x\rangle$ (Eq. (4.2.2)) ,

$$|x\rangle = c^{\dagger}_{r_1\sigma_1}c^{\dagger}_{r_2\sigma_2}\cdots c^{\dagger}_{r_{N_{\mathrm{e}}}\sigma_{N_{\mathrm{e}}}}|0\rangle, \tag{4.6.44}$$

The generalized pair function $|\phi_{\mathrm{pair}}\rangle$ is given by

$$|\phi_{\mathrm{pair}}\rangle = \left(\sum_{i,j=1}^{N_{\mathrm{s}}}\sum_{\sigma,\sigma'=\uparrow,\downarrow}f^{\sigma\sigma'}_{ij}c^{\dagger}_{i\sigma}c^{\dagger}_{j\sigma'}\right)^{N_{\mathrm{e}}/2}|0\rangle \tag{4.6.45}$$

where $f_{ij}^{\sigma\sigma'}$ denotes variational parameters.

The inner product $\langle x|\phi_{\mathrm{pair}}\rangle$ is represented as a pfaffian of $N_{\mathrm{e}} \times N_{\mathrm{e}}$ skew symmetric matrix [93]. The inner product is given by

$$\begin{aligned}\langle x|\phi_{\mathrm{pair}}\rangle = \sum_{\mathcal{P}} (N_{\mathrm{e}}/2)! \prod_{l=1}^{N_{\mathrm{e}}/2} \left(f_{r_{\mathcal{P}(2l-1)} r_{\mathcal{P}(2l)}}^{\sigma_{\mathcal{P}(2l-1)}\sigma_{\mathcal{P}(2l)}} - f_{r_{\mathcal{P}(2l)} r_{\mathcal{P}(2l-1)}}^{\sigma_{\mathcal{P}(2l)}\sigma_{\mathcal{P}(2l-1)}} \right) \\ \times \prod_{l=1}^{N_{\mathrm{e}}/2} \langle x| \left(c_{r_{\mathcal{P}(2l-1)}\sigma_{\mathcal{P}(2l-1)}}^{\dagger} c_{r_{\mathcal{P}(2l)}\sigma_{\mathcal{P}(2l)}}^{\dagger} \right) |0\rangle, \qquad (4.6.46)\end{aligned}$$

where $\mathcal{P}$ is the permutation of N_{e} with the condition

$$\begin{cases} \mathcal{P}(2l-1) < \mathcal{P}(2l) \\ \mathcal{P}(1) < \mathcal{P}(3) < \cdots < \mathcal{P}(N_{\mathrm{e}}-1) \end{cases}. \qquad (4.6.47)$$

From the power $N_{\mathrm{e}}/2$ in $|\phi\rangle$, the same term $\prod \left(f_{rr'}^{\sigma\sigma'} - f_{r'r}^{\sigma'\sigma} \right) \prod \left(c_{r\sigma}^{\dagger} c_{r'\sigma'}^{\dagger} \right)$ appears $(N_{\mathrm{e}}/2)!$ times. Using the commutation relation of fermion operators, we have

$$\langle x| \prod_{l=1}^{N_{\mathrm{e}}/2} \left(c_{r_{\mathcal{P}(2l-1)}\sigma_{\mathcal{P}(2l-1)}}^{\dagger} c_{r_{\mathcal{P}(2l)}\sigma_{\mathcal{P}(2l)}}^{\dagger} \right) |0\rangle = (-1)^{\mathcal{P}}, \qquad (4.6.48)$$

where $(-1)^{\mathcal{P}}$ is the parity of $\mathcal{P}$. Thus, $\langle x|\phi_{\mathrm{pair}}\rangle$ is given by

$$\begin{aligned}\langle x|\phi_{\mathrm{pair}}\rangle &= (N_{\mathrm{e}}/2)! \sum_{\mathcal{P}} \prod_{l=1}^{N_{\mathrm{e}}/2} \left(f_{r_{\mathcal{P}(2l-1)} r_{\mathcal{P}(2l)}}^{\sigma_{\mathcal{P}(2l-1)}\sigma_{\mathcal{P}(2l)}} - f_{r_{\mathcal{P}(2l)} r_{\mathcal{P}(2l-1)}}^{\sigma_{\mathcal{P}(2l)}\sigma_{\mathcal{P}(2l-1)}} \right) \qquad (4.6.49) \\ &= (N_{\mathrm{e}}/2)! \mathrm{Pf} X, \qquad (4.6.50)\end{aligned}$$

where PfX is a pfaffian of $N_{\mathrm{e}} \times N_{\mathrm{e}}$ skew symmetric matrix X with the element

$$X_{ij} = f_{r_i r_j}^{\sigma_i \sigma_j} - f_{r_j r_i}^{\sigma_j \sigma_i}. \qquad (4.6.51)$$

4.7 Gutzwiller-Jastrow correlation factor

By using the one-body part, such as the single mean-field Slater determinant and Hartree-Fock-Bogoliubov type wave function, the Pauli exclusion principle and pair correlation are described. However, there are also many-body correlations beyond the mean-filed theory, which can be represented by the Gutzwiller-Jastrow factor [87, 90, 94, 95]. Here, we introduce three famous many-body operators $\mathcal{P}_{\mathrm{G}}, \mathcal{P}_{\mathrm{G}}$ and $\mathcal{P}_{\text{d-h}}^{\mathrm{ex}}$.

As mentioned in subsection 4.4, the Gutzwiller factor [87] punishes the double occupation of electrons defined as

$$\mathcal{P}_{\mathrm{G}} = \exp\left(-\frac{1}{2} \sum_i g_i n_{i\uparrow} n_{i\downarrow} \right). \qquad (4.7.1)$$

The Jastrow factor [90] is defined as

$$\mathcal{P}_{\mathrm{J}} = \exp\left(-\frac{1}{2}\sum_{ij} v_{ij} n_i n_j\right), \tag{4.7.2}$$

with two-body term, where $n_i = \sum_\sigma n_{i\sigma}$ is a density operator and $v_{ij} = v(\boldsymbol{r}_i - \boldsymbol{r}_j)$ are variational parameters depending on the displacement $\boldsymbol{r}_i - \boldsymbol{r}_j$. The long-range part of this factor drives the charge density correlation and distinction between the metal and insulator.

The doublon-holon correlation factor [94, 95] is defined as

$$\mathcal{P}_{\text{d-h}}^{\text{ex}} = \exp\left[-\sum_{m=0}^{2}\sum_{l=1,2} \alpha_{(m)}^{(l)} \sum_i \xi_{i(m)}^{(l)}\right], \tag{4.7.3}$$

where $\alpha_{(m)}^{(l)}$ are variational parameters. $\xi_{i(m)}^{(l)}$ is a many-body operator which is diagonal in the real space configuration. If a doublon (holon) exists at site i and m holons (doublons) surround it at the l^{th} nearest neighbor, $\xi_{i(m)}^{(l)} = 1$. Otherwise, $\xi_{i(m)}^{(l)} = 0$. This factor represents a tendency toward formation of bound state between a doublon (doubly occupied site) and a holon (empty site) in the Mott insulating state due to the strong electron correlation.

4.8 Quantum number projection

Many electron systems have several symmetries such as translational symmetry, point group symmetry of lattice, $U(1)$ gauge symmetry, and $SU(2)$ spin-rotational symmetry. On the other hand, spontaneous symmetry breaking occurs when the vacuum is unstable in the thermodynamic limit. Superconductivity and ferromagnetism are examples of the symmetry breaking.

In the VMC method, the trial wave function sometimes does not have the symmetry of systems because the one-body part comes from a symmetry violating mean-field treatment. For example, the spin-rotational symmetry is broken in the present generalized wave function (Eq. (4.6.21)), which includes a state with total spin $S = 0$ and $S = 1$. However, the symmetry should be preserved in finite systems.

The quantum number projection technique can control and restore symmetries of variational wave functions [88, 89]. The spin projection operator $\mathcal{L}^S$ which generates a state with total spin S and $S^z = 0$ has a form

$$\mathcal{L}^S = \frac{2S+1}{8\pi^2}\int d\Omega P_S(\cos\beta) R(\Omega), \tag{4.8.1}$$

where $\Omega = (\alpha, \beta, \gamma)$ is the Euler angle and the integral is calculated over all range of Ω. The weight $P_S(\cos\beta)$ is the S^{th} Legendre polynomial. $R(\Omega)$ denotes a rotational operator defined as

$$R(\Omega) = R_z(\alpha)R_y(\beta)R_z(\gamma) = e^{i\alpha S_z} e^{i\beta S_y} e^{i\gamma S_z}, \tag{4.8.2}$$

where S_y and S_z are total spin operators of y and z directions, respectively.

Let us consider operating $\mathcal{L}^S$ to the generalized one-body part $|\phi\rangle$:

$$|\phi\rangle = \left(\sum_{i,j=1}^{N_\mathrm{s}} \sum_{\sigma,\sigma'=\uparrow,\downarrow} f_{ij}^{\sigma\sigma'} c_{i\sigma}^\dagger c_{j\sigma'}^\dagger \right)^{N_\mathrm{e}/2} |0\rangle. \tag{4.8.3}$$

The rotated wave function $R(\Omega)|\phi\rangle$ is represented using the rotated creation operator $c_{i\sigma}^\dagger(\Omega)$ in the same form as Eq. (4.8.3):

$$\mathcal{L}^S|\phi\rangle = \left(\sum_{i,j=1}^{N_\mathrm{s}} \sum_{\sigma,\sigma'=\uparrow,\downarrow} f_{ij}^{\sigma\sigma'} c_{i\sigma}^\dagger(\Omega) c_{j\sigma'}^\dagger(\Omega) \right)^{N_\mathrm{e}/2} |0\rangle. \tag{4.8.4}$$

The rotated creation operator $c_{i\sigma}^\dagger(\Omega)$ is given by

$$\begin{pmatrix} c_{i\uparrow}^\dagger(\Omega) \\ c_{i\downarrow}^\dagger(\Omega) \end{pmatrix} = R_z(\alpha) R_y(\beta) R_z(\gamma) \begin{pmatrix} c_{i\uparrow}^\dagger \\ c_{i\downarrow}^\dagger \end{pmatrix}, \tag{4.8.5}$$

with

$$R_z(\theta) = \begin{pmatrix} e^{i\theta/2} & 0 \\ 0 & e^{-i\theta/2} \end{pmatrix}, \tag{4.8.6}$$

$$R_y(\theta) = \begin{pmatrix} \cos(\theta/2) & \sin(\theta/2) \\ -\sin(\theta/2) & \cos(\theta/2) \end{pmatrix}. \tag{4.8.7}$$

Thus,

$$\begin{aligned} \mathcal{L}^S|\phi\rangle &= \frac{2S+1}{8\pi^2} \int d\Omega P_S(\cos\beta) \left(\sum_{i,j=1}^{N_\mathrm{s}} \sum_{\sigma,\sigma'=\uparrow,\downarrow} f_{ij}^{\sigma\sigma'} c_{i\sigma}^\dagger(\Omega) c_{j\sigma'}^\dagger(\Omega) \right)^{N_\mathrm{e}/2} |0\rangle \\ &= \frac{2S+1}{8\pi^2} \int_0^{2\pi} d\alpha \int_0^{\pi} d\beta \int_0^{2\pi} d\gamma \sin\beta P_S(\cos\beta) \\ &\quad \times \left(\sum_{i,j=1}^{N_\mathrm{s}} \sum_{\sigma,\sigma'=\uparrow,\downarrow} F_{ij}^{\sigma\sigma'}(\Omega) c_{i\sigma}^\dagger c_{j\sigma'}^\dagger \right)^{N_\mathrm{e}/2} |0\rangle, \end{aligned} \tag{4.8.8}$$

where $F_{ij}^{\sigma\sigma'}(\Omega)$ is transformed from $f_{ij}^{\sigma\sigma'}$ using Eqs. (4.8.5) and (4.8.6), (4.8.7).

In this thesis, the one-body part (Eq. (4.6.4)) contains only $S^z = 0$ components, so that the integration over γ is omitted,

$$\mathcal{L}^S|\phi\rangle = \frac{2S+1}{4\pi} \int_0^{2\pi} d\alpha \int_0^{\pi} d\beta \sin\beta P_S(\cos\beta) R_z(\alpha) R_y(\beta) |\phi\rangle. \tag{4.8.9}$$

Moreover, the integration over α is also omitted by using a set of real space configurations $\{|x\rangle\}$ since $\mathcal{L}^S$ filters out $S^z \neq 0$ components from samples of $|x\rangle$,

$$\begin{aligned}
\mathcal{L}^S|\phi\rangle &= \sum_x |x\rangle\langle x|\mathcal{L}^S|\phi\rangle \quad \text{(Filtering out } S^z \neq 0 \text{ components)} \\
&= \sum_x^{S^z=0} |x\rangle\langle x|\mathcal{L}^S|\phi\rangle \\
&= \sum_x^{S^z=0} |x\rangle \frac{2S+1}{2}\int_0^\pi d\beta \sin\beta P_S(\cos\beta)\langle x|R_y(\beta)|\phi\rangle. \qquad (4.8.10)
\end{aligned}$$

When the Gutzwiller-Jastrow factor is operated to $\mathcal{L}^S|\phi\rangle$, the form is given by

$$|\psi\rangle = \mathcal{P}\mathcal{L}^S|\phi\rangle = \sum_x^{S^z=0} |x\rangle\langle x|\mathcal{P}\mathcal{L}^S|\phi\rangle, \qquad (4.8.11)$$

with

$$\langle x|\mathcal{P}\mathcal{L}^S|\phi\rangle = P(x)\frac{2S+1}{2}\int_0^\pi d\beta \sin\beta P_S(\cos\beta)\langle x|R_y(\beta)|\phi\rangle. \qquad (4.8.12)$$

The integration over β is evaluated efficiently by the Gauss-Legendre quadrature [96]. The required number of mesh points is typically 10 and 20 for the spin singlet state in the half-filled Hubbard model with 10 and 200 sites, respectively.

Under the condition $S^z = 0$, $|x\rangle$ is defined as

$$|x\rangle = c^\dagger_{r_1\uparrow}c^\dagger_{r_2\uparrow}\cdots c^\dagger_{r_{N_{\mathrm{e}}/2}\uparrow}c^\dagger_{r_{N_{\mathrm{e}}/2+1}\downarrow}c^\dagger_{r_{N_{\mathrm{e}}/2+2}\downarrow}\cdots c^\dagger_{r_{N_{\mathrm{e}}}\downarrow}|0\rangle. \qquad (4.8.13)$$

The component $\langle x|R^y(\beta)|\phi\rangle$ is given by

$$\begin{aligned}
\langle x|R_y(\beta)|\phi\rangle &= \langle x|\left(\sum_{i,j}^{N_s}\sum_{\sigma_1,\sigma_2,\sigma_3,\sigma_4}[R_y(\beta)]_{\sigma_1\sigma_3}[R_y(\beta)]_{\sigma_2\sigma_4}f_{ij}^{\sigma_1\sigma_2}c^\dagger_{i\sigma_3}c^\dagger_{i\sigma_4}\right)^{N_{\mathrm{e}}/2}|0\rangle \\
&= \langle x|\left[\sum_{i,j=1}^{N_{\mathrm{s}}}\sum_{\sigma\sigma'}F_{ij}^{\sigma\sigma'}(\beta)c^\dagger_{i\sigma}c^\dagger_{j\sigma'}\right]^{N_{\mathrm{e}}/2}|0\rangle \\
&= (N_{\mathrm{e}}/2)!\ \mathrm{Pf}X(\beta), \qquad (4.8.14)
\end{aligned}$$

where the element of skew symmetric matrix $X(\beta)$ is

$$X_{ij}(\beta) = \begin{cases}
F^{\uparrow\uparrow}_{r_ir_j}(\beta) - F^{\uparrow\uparrow}_{r_jr_i}(\beta) & (i \leq N_{\mathrm{e}}/2, j \leq N_{\mathrm{e}}/2) \\
F^{\uparrow\downarrow}_{r_ir_j}(\beta) - F^{\downarrow\uparrow}_{r_jr_i}(\beta) & (i \leq N_{\mathrm{e}}/2, j > N_{\mathrm{e}}/2) \\
F^{\downarrow\uparrow}_{r_ir_j}(\beta) - F^{\uparrow\downarrow}_{r_jr_i}(\beta) & (i > N_{\mathrm{e}}/2, j \leq N_{\mathrm{e}}/2) \\
F^{\downarrow\downarrow}_{r_ir_j}(\beta) - F^{\downarrow\downarrow}_{r_jr_i}(\beta) & (i > N_{\mathrm{e}}/2, j > N_{\mathrm{e}}/2)
\end{cases}. \qquad (4.8.15)$$

Therefore, the inner product $\langle x|R_y(\beta)|\phi\rangle$ is

$$\langle x|\mathcal{P}\mathcal{L}^S|\phi\rangle = (N_{\mathrm{e}}/2)!P(x)\frac{2S+1}{2}\int_0^\pi d\beta \sin\beta P_S(\cos\beta)\mathrm{Pf}X(\beta). \qquad (4.8.16)$$

4.9 Stochastic reconfiguration method

The stochastic reconfiguration (SR) method, which restricts the variation of the wave function, offers an efficient and stable multi-variable optimization method [74–76]. The SR method is in part similar to the Newton method and steepest descent (SD) method. In addition, the SR method is equivalent to the time and imaginary-time evolution [97, 98]. We recall the variational energy

$$E_\gamma = \min_\gamma \frac{\langle\psi_\gamma|\hat{H}|\psi_\gamma\rangle}{\langle\psi_\gamma|\psi_\gamma\rangle}, \tag{4.9.1}$$

where $|\psi_\gamma\rangle$ is the variational wave function with variational parameters $\gamma = (\gamma_1, \gamma_2, \cdots, \gamma_p)$. p is the total number of variational parameters. Let us consider the optimization by energy minimization for the variation $\alpha_i \to \alpha_i + \gamma_i$ $(i = 1, 2, \cdots, p)$. The second order Taylor approximation of the variational energy around α is

$$E_{\alpha+\gamma} = E_\alpha + \sum_k g_k\gamma_k + \frac{1}{2}\sum_{k,l} h_{kl}\gamma_k\gamma_l + \mathcal{O}(\gamma^3), \tag{4.9.2}$$

where g_k is the energy gradient vector and h_{kl} is the energy Hessian matrix,

$$g_k = \frac{\partial}{\partial\alpha_k}E_\gamma, \tag{4.9.3}$$

$$h_{kl} = \frac{\partial^2}{\partial\alpha_k\partial\alpha_l}E_\gamma. \tag{4.9.4}$$

We employ the following cost function,

$$\mathcal{F}_{\mathrm{N}} = \sum_k g_k\gamma_k + \frac{1}{2}\sum_{k,l} h_{kl}\gamma_k\gamma_l. \tag{4.9.5}$$

The stationary condition $\partial\mathcal{F}_{\mathrm{N}}/\partial\gamma = 0$ leads to the Newton method,

$$\gamma_k = -h_{kl}^{-1}g_l. \tag{4.9.6}$$

In a similar way, the cost function of the SD method is defined as

$$\mathcal{F}_{\mathrm{SD}} = \sum_k g_k\gamma_k + \lambda\sum_k \gamma_k^2, \tag{4.9.7}$$

where λ is a Lagrange multiplier. The second term $\lambda\sum_k\gamma_k^2$, which denotes the Cartesian distance in the parameter space, restricts the variation of parameters to stabilize the optimization. From the stationary condition, we have

$$\gamma_k = -\frac{1}{2\lambda}g_k. \tag{4.9.8}$$

This method optimizes all the parameters simultaneously, but is unstable when various ordering fluctuations compete. Small change of the variational parameters sometimes give rise to a large change of the wave function, which induces the instability of the SD method.

On the other hand, the SR method restricts the variation of the wave function. We introduce the normalized wave function in the p-dimensional parameter space,

$$|\overline{\psi}_\alpha\rangle = \frac{1}{\sqrt{\langle\psi_\alpha|\psi_\alpha\rangle}}|\psi_\alpha\rangle. \tag{4.9.9}$$

The first order Taylor approximation of $|\overline{\psi}_{\alpha+\gamma}\rangle$ around α is given by

$$|\overline{\psi}_{\alpha+\gamma}\rangle = |\overline{\psi}_\alpha\rangle + \sum_{k=1}^{p}\gamma_k|\overline{\psi}_{k\alpha}\rangle + \mathcal{O}(\gamma^2), \tag{4.9.10}$$

where $|\overline{\psi}_{k\alpha}\rangle$ is the derivative of $|\overline{\psi}_\alpha\rangle$.

$$\begin{aligned}|\overline{\psi}_{k\alpha}\rangle &= \frac{\partial}{\partial\alpha_k}|\overline{\psi}_\alpha\rangle \\ &= \frac{1}{\sqrt{\langle\psi_\alpha|\psi_\alpha\rangle}}\left(\frac{\partial}{\partial\alpha_k}|\psi_\alpha\rangle - \frac{\langle\psi_\alpha|\partial/\partial\alpha_k|\psi_\alpha\rangle}{\langle\psi_\alpha|\psi_\alpha\rangle}|\psi_\alpha\rangle\right).\end{aligned} \tag{4.9.11}$$

The wave function set $|\overline{\psi}_\alpha\rangle$ forms a non-orthogonal basis. The norm of the variation between $|\overline{\psi}_\alpha\rangle$ and $|\overline{\psi}_{\alpha+\gamma}\rangle$ is defined as

$$\begin{aligned}\Delta^2_{\mathrm{norm}} &=\| \, |\overline{\psi}_{\alpha+\gamma}\rangle - |\overline{\psi}_\alpha\rangle \, \|^2 \\ &= \sum_{k,l=1}^{p}\gamma_k\gamma_l\langle\overline{\psi}_{k\alpha}|\overline{\psi}_{l\alpha}\rangle = \sum_{k,l=1}^{p}\gamma_k\gamma_l S_{kl},\end{aligned} \tag{4.9.12}$$

where $S_{kl} = \langle\overline{\psi}_{k\alpha}|\overline{\psi}_{l\alpha}\rangle$ is the overlap matrix.From Eq. (4.9.12), the matrix S corresponds to the metric matrix in the parameter space. The cost function of the SR method is defined as

$$\mathcal{F}_{\mathrm{SR}} = \sum_k g_k\gamma_k + \lambda\Delta^2_{\mathrm{norm}}. \tag{4.9.13}$$

From the stationary condition, the optimized parameter change is given by

$$\gamma_k = -\Delta t\sum_{l=1}^{p}S^{-1}_{kl}g_l, \tag{4.9.14}$$

where $\Delta t = (2\lambda)^{-1}$ determines the speed of the optimization.

4.10 Stabilization of SR method

The instability of the SR method arises from the overlap matrix S. Since S is a positive definite symmetric matrix, S can be diagonalized using an orthogonal matrix U:

$$\sum_{k,l=1}^{p}U_{ki}U_{lj}S_{kl} = \lambda_i\delta_{ij}, \tag{4.10.1}$$

and

$$S_{kl} = \sum_{i=1}^{p} \lambda_i U_{ki} U_{li}, \tag{4.10.2}$$

$$S_{kl}^{-1} = \sum_{i=1}^{p} \frac{1}{\lambda_i} U_{ki} U_{li}, \tag{4.10.3}$$

where $\lambda_i > 0$ are the eigenvalues arranged in descending order ($\lambda_1 \geq \lambda_2 \geq \cdots \geq \lambda_p$). The small eigenvalues ($\lambda_i \ll \lambda_1$) give rise to the instability in the inverse matrix S^{-1} (Eq. (4.10.3)). Using Eqs. (4.10.2) and (4.9.12), we have

$$\Delta_{\text{norm}}^2 = \sum_{k,l,i=1}^{p} \gamma_k \gamma_l \lambda_i U_{ki} U_{li} = \sum_{i=1}^{p} \lambda_i x_i^2, \tag{4.10.4}$$

with

$$x_k = \sum_{i=1}^{p} \gamma_k U_{ki}. \tag{4.10.5}$$

Eq. (4.10.4) means that the variation in the direction x_i is negligible in the case of $\lambda_i/\lambda_1 \ll 1$. We introduce the truncation of the directions which satisfy $\lambda_i/\lambda_1 < \varepsilon_{\text{wf}}$. Eq. (4.9.14) is then rewritten as

$$\gamma_k = -\Delta t \sum_{l=1}^{p} S_{kl}^{-1} g_l = -\Delta t \sum_{l=1}^{p} \sum_{k=1}^{p} \sum_{i=1}^{p} \frac{1}{\lambda_i} U_{ki} U_{li} g_l \tag{4.10.6}$$

$$\Downarrow \text{(Truncation)}$$

$$\gamma_k = -\Delta t \sum_{l=1}^{p} \sum_{k=1}^{p} \sum_{i=1}^{q} \frac{1}{\lambda_i} U_{ki} U_{li} g_l \tag{4.10.7}$$

By changing the truncation parameter ε_{wf}, both the accuracy and stability of the SR method can be controlled [99].

Further, the small eigenvalues can be increased by the modification of diagonal elements in the overlap matrix S,

$$S_{kk} \to (1+\varepsilon) S_{kk}, \tag{4.10.8}$$

where $\varepsilon \ll 1$ is a small constant [100]. This modification preserves the positive definite property and does not change the optimal parameters.

4.11 Derivative operator

The overlap matrix S and energy gradient $\boldsymbol{g}$ are evaluated as follows. The wave function considered here is

$$|\psi_\alpha\rangle = \mathcal{P}_\alpha \mathcal{L} |\phi_\alpha\rangle = \mathcal{P}_\alpha \sum_n \omega_n |\phi_\alpha^{(n)}\rangle, \tag{4.11.1}$$

where the summation $\sum_n$ and weight ω_n comes from the quantum number projection $\mathcal{L}$. The variational parameters of the Gutzwiller-Jastrow factor and transformed one-body parts are independent of each other. We introduce the diagonal operator $\mathcal{O}_k$ in the real space configuration $|x\rangle$,

$$\mathcal{O}_k = \sum_x |x\rangle \left[\frac{1}{\langle x|\psi_\alpha\rangle} \frac{\partial}{\partial \alpha_k} \langle x|\psi_\alpha\rangle \right] \langle x| = \sum_x |x\rangle O_k(x) \langle x|. \tag{4.11.2}$$

$\mathcal{O}_k$ satisfies the following relations:

$$\langle x|\mathcal{O}_k|\psi_\alpha\rangle = \frac{\partial}{\partial \alpha_k} \langle x|\psi_\alpha\rangle, \tag{4.11.3}$$

$$\mathcal{O}_k|\psi_\alpha\rangle = \sum_x |x\rangle \frac{\partial}{\partial \alpha_k} \langle x|\psi_\alpha\rangle, \tag{4.11.4}$$

$$\langle \mathcal{O}_k\rangle = \frac{\langle\psi_\alpha|\mathcal{O}_k|\psi_\alpha\rangle}{\langle\psi_\alpha|\psi_\alpha\rangle} = \frac{\langle\psi_\alpha|\partial/\partial\alpha_k|\psi_\alpha\rangle}{\langle\psi_\alpha|\psi_\alpha\rangle}. \tag{4.11.5}$$

The derivative of the normalized wave function (Eq. (4.9.9)) is rewritten as

$$|\overline{\psi}_{k\alpha}\rangle = \frac{1}{\sqrt{\langle\psi_\alpha|\psi_\alpha\rangle}} \left(\mathcal{O}_k - \langle\mathcal{O}_k\rangle\right) |\psi_\alpha\rangle, \tag{4.11.6}$$

and the overlap matrix S is

$$S_{kl} = \langle\mathcal{O}_k\mathcal{O}_l\rangle - \langle\mathcal{O}_k\rangle\langle\mathcal{O}_l\rangle. \tag{4.11.7}$$

The energy gradient $\boldsymbol{g}$ is

$$g_k = \frac{\partial}{\partial \alpha_k} \langle\overline{\psi}_\alpha|\mathcal{H}|\overline{\psi}_\alpha\rangle = \langle\overline{\psi}_{k\alpha}|\mathcal{H}|\overline{\psi}_\alpha\rangle + \langle\overline{\psi}_\alpha|\mathcal{H}|\overline{\psi}_{k\alpha}\rangle \tag{4.11.8}$$

$$= 2\langle\mathcal{H}\mathcal{O}_k\rangle - 2\langle\mathcal{H}\rangle\langle\mathcal{O}_k\rangle. \tag{4.11.9}$$

The expressions of $O_k(x)$ are derived as follows [73, 74, 101, 102]. The Gutzwiller-Jastrow correlation factor has an exponential form,

$$\mathcal{P}_\alpha = \exp\left[-\sum_k \alpha_k \Theta_k \right], \tag{4.11.10}$$

where α_k are variational parameters and Θ_k are diagonal operators in real space configurations ($\Theta_k|x\rangle = \Theta_k(x)|x\rangle$). The expression for $\mathcal{P}_\alpha$ is

$$O_k(x) = -\Theta_k(x). \tag{4.11.11}$$

Since the inner product $\langle x|\phi_\alpha^{(n)}\rangle$ is proportional to the Pfaffian $\mathrm{Pf}X_\alpha^{(n)}$, the expression for the one-body part is given by

$$\begin{aligned}
O_k(x) &= \frac{1}{\langle x|\psi_\alpha\rangle}\frac{\partial}{\partial\alpha_k}\langle x|\psi_\alpha\rangle \\
&= \frac{1}{\langle x|\mathcal{L}|\phi_\alpha\rangle}\frac{\partial}{\partial\alpha_k}\langle x|\mathcal{L}|\phi_\alpha\rangle \\
&= \frac{1}{\langle x|\mathcal{L}|\phi_\alpha\rangle}\frac{\partial}{\partial\alpha_k}\sum_n \omega_n\langle x|\phi_\alpha^{(n)}\rangle \\
&= (N_\mathrm{e}/2)!\frac{1}{\langle x|\mathcal{L}|\phi_\alpha\rangle}\sum_n \omega_n\frac{\partial}{\partial\alpha_k}\mathrm{Pf}X_\alpha^{(n)} \\
&= \frac{\sum_n \omega_n \mathrm{Pf}X_\alpha^{(n)}\mathrm{Tr}\left[X_\alpha^{(n)-1}\frac{\partial}{\partial\alpha_k}X_\alpha^{(n)}\right]}{2\times\sum_n\omega_n\mathrm{Pf}X_\alpha^{(n)}}.
\end{aligned} \tag{4.11.12}$$

By using the above equations, the overlap matrix and energy gradient are evaluated in the VMC method.

4.12 Skew symmetric matrix and pfaffian

A $2M \times 2M$ skew-symmetric matrix is the matrix which satisfies

$$A^\mathrm{T} = -A \quad (A_{ij} = -A_{ji}), \tag{4.12.1}$$

where A^T denotes the transposed matrix of A. The pfaffian of A is defined as antisymmetric product

$$\mathrm{Pf}A = \sum_{\mathcal{P}}(-1)^{\mathcal{P}}\prod_{k=1}^{M} A_{\mathcal{P}(2k-1)\mathcal{P}(2k)}, \tag{4.12.2}$$

where the summation runs over all the pair partitions $\mathcal{P}$ of $2M$ indices which satisfy $\mathcal{P}(2k-1) < \mathcal{P}(2k)$. $(-1)^{\mathcal{P}}$ denotes the parity of the permutation $\mathcal{P}$:

$$\begin{pmatrix} 1 & 2 & \cdots & 2M-1 & 2M \\ \mathcal{P}(1) & \mathcal{P}(2) & \cdots & \mathcal{P}(2M-1) & \mathcal{P}(2M) \end{pmatrix}.$$

4.13 Update technique for skew-symmetric matrix

In the present formalism, one has to evaluate the pfaffian for each Monte-Carlo step. The update of the pfaffian is carried out efficiently by using an algorithm which is similar to the Ceperley's method [70,72]. When the 1st electron moves, the 1st row and column of the skew matrix A are changed simultaneously. The pfaffian of the updated skew matrix B is calculated using the Cayley's identity [103]:

$$\det\begin{bmatrix} 0 & A_{12} & \cdots & A_{1M} \\ -b_{12} & 0 & \cdots & A_{2M} \\ \vdots & \vdots & \ddots & \vdots \\ -b_{1M} & -A_{2M} & \cdots & 0 \end{bmatrix} = \mathrm{Pf}\begin{bmatrix} 0 & A_{12} & \cdots & A_{1M} \\ -A_{12} & 0 & \cdots & A_{2M} \\ \vdots & \vdots & \ddots & \vdots \\ -A_{1M} & -A_{2M} & \cdots & 0 \end{bmatrix}$$
$$\times\ \mathrm{Pf}\begin{bmatrix} 0 & b_{12} & \cdots & b_{1M} \\ -b_{12} & 0 & \cdots & A_{2M} \\ \vdots & \vdots & \ddots & \vdots \\ -b_{1M} & -A_{2M} & \cdots & 0 \end{bmatrix}.$$

Using this identity and cofactor expansion of determinants, $\det A = (\mathrm{Pf}A)^2$, we have

$$\begin{aligned} \mathrm{Pf}B &= \det A \sum_m A^{-1}_{\alpha m} b_m \ / \ \mathrm{Pf}A \\ &= \mathrm{Pf}A \sum_m A^{-1}_{\alpha m} b_m, \end{aligned} \tag{4.13.1}$$

where b_m is the updated element of α^{th} row in B. Thus, the inverse matrix A^{-1} also has to be evaluated.

An inverse matrix of B is calculated by using the Sherman-Morrison's formula [104]. For any nonsingular matrix A and any column vector $\boldsymbol{u}$ and $\boldsymbol{v}$ with the condition $1 + \boldsymbol{v}^{\mathrm{T}} A \boldsymbol{u} \neq 0$, the formula is given by

$$[A + \boldsymbol{u}\boldsymbol{v}^{\mathrm{T}}]^{-1}_{ij} = A^{-1}_{ij} - \frac{1}{1 + \boldsymbol{v}^{\mathrm{T}} A \boldsymbol{u}} \sum_{m,n} A^{-1}_{im} u_m v_n A^{-1}_{nj}. \tag{4.13.2}$$

If A is a skew-symmetric matrix, an inverse matrix of $B = A + \boldsymbol{u}\boldsymbol{v}^{\mathrm{T}} - \boldsymbol{v}\boldsymbol{u}^{\mathrm{T}}$ is

$$B^{-1}_{ij} = A^{-1}_{ij} + \frac{1}{\sum_m A^{-1}_{\alpha m} b_m} \sum_{m,n} \left(A^{-1}_{im} v_m u_n A^{-1}_{nj} - A^{-1}_{im} u_m v_n A^{-1}_{nj} \right). \tag{4.13.3}$$

Substituting $u_i = b_i - A_{\alpha i},\ v_i = \delta_{\alpha i}$ for the above equation, we have

$$\begin{aligned} B^{-1}_{ij} = A^{-1}_{ij} + \frac{1}{\sum_m A^{-1}_{\alpha m} b_m} \Bigg[&- \left(\sum_m A^{-1}_{im} b_m \right) A^{-1}_{\alpha j} \\ &+ \left(\sum_m A^{-1}_{jm} b_m \right) A^{-1}_{\alpha i} + \delta_{i\alpha} A^{-1}_{\alpha j} - \delta_{j\alpha} A^{-1}_{\alpha i} \Bigg]. \end{aligned} \tag{4.13.4}$$

4.14 Finite-size effects and boundary conditions in VMC

By using the VMC method, one studies finite-size systems. However, what is needed is an information about actual materials containing huge number of atoms. There are qualitative differences between finite-size systems and infinite-size systems rigorously. For instance, the spontaneous symmetry breaking occurs not in finite-size systems but in infinite-size systems. Thus, order parameters, such as the superconducting and AFM, ferromagnetic order parameters, should be zero in the finite-size systems. However, finite-size systems have a boundary, which should not be essential in large scale properties.

Boundaries of finite-size systems are eliminated by periodic boundary condition. Let us consider a one-dimensional chain of L sites with the periodic boundary condition, where site $L+1(0)$ is equal to site $1(L)$. Thus, the topology of the system corresponds to a ring, where there is no boundary. Further, the periodic boundary condition can be extended in higher dimensional systems. This procedure allows us to examine large scale properties by using finite-size systems. Of course, the magnitude of order parameters (strictly speaking, ordering fluctuations) can be overestimated in small systems since order parameters tend to decrease with the system size. This wrong estimation is called the finite-size effect.

In the VMC calculation, degenerate states (open-shell) are unfavored because the optimization can become unstable due to the large number of configurations of the ground state. To form non-degenerate states (closed shells), one can set appropriate phase changes of electrons passing through boundaries. There are two notable ways for setting the phase changes; the periodic and antiperiodic boundary conditions. The former is already specified above. Under the antiperiodic condition, the value of the phase change is π when an electron goes across the boundary. In a one-dimensional chain of L sites, creation operators satisfy $c^\dagger_{L+1} = -c^\dagger_1$ ($c^\dagger_0 = -c^\dagger_L$). Then, the k-points decrease by L/π compared to the case of the periodic boundary condition

$$k = \frac{2\pi}{L} n \text{ (periodic)}, \tag{4.14.1}$$

$$k = \frac{2\pi}{L}\left(n - \frac{1}{2}\right) \text{ (antiperiodic)}. \tag{4.14.2}$$

We demonstrate the merit of the antiperiodic boundary condition in the case of half-filled square lattice. The band dispersion is given by $\varepsilon(\boldsymbol{k}) = -2t(\cos k_x + \cos k_y)$. The periodic boundary condition along one of the two axes and antiperiodic for the other axis (p.a.) as shown in Fig. 4.1. Under this condition, the states at the Fermi level are non-degenerate. On the other hand, in case the periodic boundary condition is imposed in both directions (p.p.), the states at the Fermi level are highly degenerate (see Fig. 4.1); therefore it is not suitable for the VMC calculation. In general, the antiperiodic boundary condition enables us to form the closed shell in the low-doped two- and three-dimensional systems, which are attractive in terms of relations with exotic phenomena, such as unconventional superconductivity and phase competition.

Unfortunately, the antiperiodic boundary condition often brings confusion when one sets trial wave functions and calculate physical quantities in the VMC method. Here we explain the misleading point referring to the formalism shown in subsection 4.4. Let us consider a one-dimensional chain with the antiperiodic boundary condition. When an electron moves from site L to the "nearest neighbor site" $L+1$, the electron returns to site 1 and the sign of the creation operator is changed. When one evaluates and updates Slater determinants (see Eqs. (4.4.20) and (4.4.21)), one has to care about the sign of them.

From the above, the boundary condition is helpful to obtain approximations of long scale properties from VMC calculations of finite-size systems but can give rise to the finite-size effect and bring some confusion.

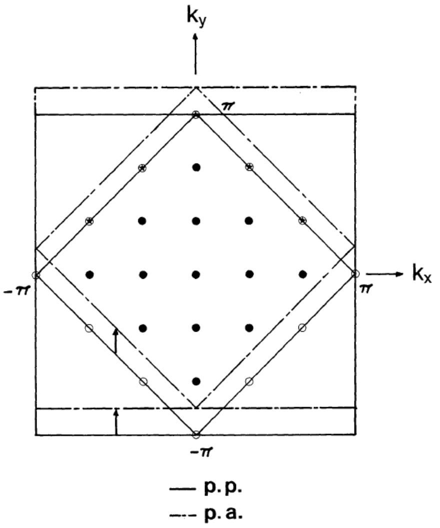

Fig. 4.1: An illustration for the boundary condition and k-points within the Fermi sea in the case of square lattice for 6x6 sites. The first Brillouin zone and the Fermi line for the periodic-periodic (p.p) case is drawn with solid lines, while those of the periodic-antiperiodic (p.a.) case is shown with dash-dotted lines. This figure is taken from Ref. [86].

4.15 Algorithm of mVMC method

We summarize the algorithm of the mVMC method.

1. Set the model and system size, form of variational wave functions, computational conditions,
2. Set the initial value of variational parameters such as $g_i, v_{ij}, \alpha^{(l)}_{(m)}, f_{ij}$,
3. Set the initial configuration of electrons,
4. Construct the skew-symmetric matrix X of the initial state and evaluate the pfaffian $\mathrm{Pf}X$ and inverse matrix X^{-1} by using the definition of the pfaffian (Eq. (4.12.2)) and Cramer's rule,
5. Update the configuration several times without observations, and make systems reach equilibrium,
6. Update the configuration several times without observations, and improve the independency between samples,
7. Measure observables,
8. Repeat steps 6 and 7,
9. The expected values of observables are obtained from the sample,
10. Optimize variational parameters referring to observables by using the SR method,
11. Repeat steps 3-10,
12. The optimized variational parameters are obtained by averaging the parameters over the last several optimization steps,
13. Repeat steps 3-7 times,
14. By using expected values of observables, the expected values and standard errors are evaluated.

The computational cost of the VMC method can be strongly reduce if the sampling is parallelized. When the parallel computing grain size of a task is large, the calculation efficiency is highly improved. Thus, the VMC method is suitable to the parallelization.

Although the mVMC method is difficult to handle, I implemented the mVMC method by myself referring a previous work [70]. Further, I mastered the method and performed the mVMC calculations successfully. Later, I transfered from my own program to an open software [71] because it has the convenient flexible interface. We performed all calculations in this thesis by using the open software. The initial values of the variational wave functions and superconducting correlation functions are obtained from my own program.

5 Two-leg ladder and bilayer Hubbard models with an incipient band

5.1 Motivation

The above mentioned studies on the two-leg ladder and bilayer lattices with diagonal hoppings adopted the FLEX approximation [61,62,68], but because FLEX ignores higher order vertex corrections, it is not clear whether the method can be applied to strongly correlated regime. In this section, we study Hubbard models on the two-leg ladder and bilayer square lattices, using a many-variable variational Monte-Carlo (mVMC) method [70, 71], which enables us to perform high-precision calculations in the strong coupling regime. By comparing the results for the two-leg ladder (one dimensional) and the bilayer lattice (two dimensional), and with and without the diagonal hoppings, we discuss how the density of states (DOS) affects superconductivity and antiferromagnetism when one of the bands is close to being incipient.

5.2 Models

We study Hubbard models on the two-leg ladder and bilayer square lattices (Fig. 5.1). The two-leg Hubbard ladder is given as

$$\begin{aligned} H = &-t_{\mathrm{l}} \sum_{\langle ij\rangle m\sigma} (c^{\dagger}_{im\sigma} c_{jm\sigma} + \mathrm{h.c.}) - t_{\mathrm{r}} \sum_{i\sigma} (c^{\dagger}_{i0\sigma} c_{i1\sigma} + \mathrm{h.c.}) \\ &- t' \sum_{\langle ij\rangle \sigma} (c^{\dagger}_{i0\sigma} c_{j1\sigma} + \mathrm{h.c.}) + U \sum_{im} n_{im\uparrow} n_{im\downarrow}, \end{aligned} \tag{5.2.1}$$

where $c^{\dagger}_{im\sigma}/c_{im\sigma}$ are creation/annihilation operators for an electron with spin $\sigma(=\uparrow,\downarrow)$ on the i^{th} site on the m^{th} chain (m=0 or 1), and $n_{im\sigma} = c^{\dagger}_{im\sigma} c_{im\sigma}$. The nearest neighbor hoppings in the leg and rung directions are t_{l} and t_{r}, respectively, and the next nearest neighbor diagonal hopping is t'. Since two chains are connected by t_{r}, we will call this the inter-chain hopping. The band structure for this model is

$$\varepsilon(\boldsymbol{k}) = -2(t_{\mathrm{l}} + t' \cos k_y) \cos k_x - t_{\mathrm{r}} \cos k_y, \tag{5.2.2}$$

where the case of $k_y = 0$ (π) corresponds to the bonding (anti-bonding) band. For $t' > 0$, the bonding band is wider than the anti-bonding one.

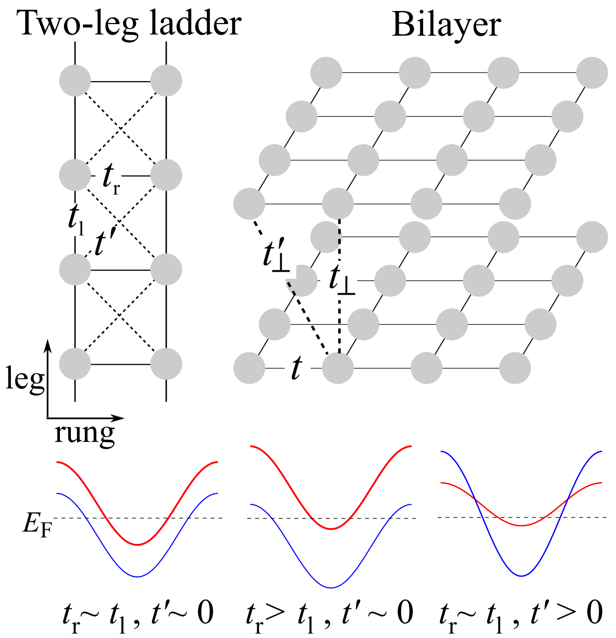

Fig. 5.1: Upper panel: the two-leg ladder lattice (left) and the bilayer lattice (right). Lower panels: typical band structures of the two-leg ladder lattice. Left: $t_\mathrm{r} \sim t_\mathrm{l}, t' \sim 0$, middle: $t_\mathrm{r} > t_\mathrm{l}, t' \sim 0$, right: $t_\mathrm{r} \sim t_\mathrm{l}, t' > 0$.

The bilayer Hubbard model on the square lattice is given as

$$\begin{aligned} H = &-t \sum_{\langle ij \rangle m\sigma} (c^\dagger_{im\sigma} c_{jm\sigma} + \mathrm{h.c.}) - t_\perp \sum_{i\sigma} (c^\dagger_{i0\sigma} c_{i1\sigma} + \mathrm{h.c.}) \\ &- t'_\perp \sum_{\langle ij \rangle \sigma} (c^\dagger_{i0\sigma} c_{j1\sigma} + \mathrm{h.c.}) + U \sum_{im} n_{im\uparrow} n_{im\downarrow}, \end{aligned} \tag{5.2.3}$$

where $c^\dagger_{im\sigma}/c_{im\sigma}$ are creation/annihilation operators for an electron with spin $\sigma(=\uparrow,\downarrow)$ on the i^th site on the m^th layer (m=0 or 1). The intra-layer hopping is t and the inter-layer hopping is $t_\perp$, the next nearest neighbor inter-layer hopping is $t'_\perp$. The band structure for this model is

$$\varepsilon(\boldsymbol{k}) = -2(t + t'_\perp \cos k_z)(\cos k_x + \cos k_y) - t_\perp \cos k_z, \tag{5.2.4}$$

where the case of $k_z = 0$ (π) corresponds to the bonding (anti-bonding) band. For $t'_\perp > 0$, the bonding band is wider than the anti-bonding one.

We take $N_\mathrm{s} = 60 \times 2$ ($12 \times 12 \times 2$) sites for the two-leg ladder (bilayer) Hubbard model with the antiperiodic-periodic boundary condition in x (y) direction. A band filling is defined as $n = N_\mathrm{e}/N_\mathrm{s}$ where $N_\mathrm{e} = \sum_{mi\sigma} n_{im\sigma}$. Hereinafter, the site index (i, m) is simply rewritten as i.

To study the ground state of these Hubbard models, we employ a mVMC method [70, 71], which incorporates the strong correlation and various ordering fluctuations accurately. Our variational wave function is defined as

$$|\phi\rangle = \mathcal{P}_{\mathrm{G}}\mathcal{P}_{\mathrm{J}}|\phi_{\mathrm{pair}}\rangle, \tag{5.2.5}$$

where $\mathcal{P}_{\mathrm{G}}, \mathcal{P}_{\mathrm{J}}$ are the Gutzwiller and Jastrow correlation factors, respectively. $|\phi_{\mathrm{pair}}\rangle$ is the one-body part defined as

$$|\phi_{\mathrm{pair}}\rangle = \left[\sum_{i,j=1}^{N_{\mathrm{s}}} f_{ij} c_{i\uparrow}^{\dagger} c_{j\downarrow}^{\dagger}\right]^{N_{\mathrm{e}}/2} |0\rangle, \tag{5.2.6}$$

where f_{ij} is assumed to have 2×2 $(2 \times 2 \times 2)$ sublattice structure or equivalently $2 \times 2 \times N_{\mathrm{s}}$ $(2 \times 2 \times 2 \times N_{\mathrm{s}})$ independent variational parameters for one-body part in the two-leg ladder (bilayer) systems. To study a possible superconducting state, we consider the BCS wave function (Eq. (4.6.3)). In this study, the BCS partial d ($s^{\pm}$)-wave superconducting state are employed as the initial states for the ladder (bilayer) system, namely, $\Delta_{\pm}(k) = \pm\Delta_0$ for bonding and antibonding bands, respectively. We also employed more elaborate variational wave functions with antiferromagnetic and superconducting mean fields, spin projection. However, the improvement did not affect results qualitatively because antiferromagnetic orders are destroyed by spin singlets formed in the interchain (interlayer) direction when the interchain (interlayer) hopping is large. Thus, this simple wave function can describe the ground state of these models properly. We optimize the variational parameters simultaneously to minimize the variational energy by relying on the stochastic reconfiguration method [73].

To investigate the ground state properties of these Hubbard models, we evaluate the momentum distribution function and spin-structure factors, equal-time superconducting correlation. The momentum distribution function is defined as

$$n_{\sigma}(\boldsymbol{q}) = \frac{1}{N_{\mathrm{s}}} \sum_{i,j} \langle c_{i\sigma}^{\dagger} c_{j\sigma}\rangle \exp\left[i\boldsymbol{q}\cdot(\boldsymbol{r}_i - \boldsymbol{r}_j)\right].$$

and the spin-structure factor is defined as

$$S(\boldsymbol{q}) = \frac{1}{3N_{\mathrm{s}}} \sum_{i,j} \langle \boldsymbol{S}_i \cdot \boldsymbol{S}_j\rangle \exp\left[i\boldsymbol{q}\cdot(\boldsymbol{r}_i - \boldsymbol{r}_j)\right].$$

In the case of the two-leg ladder (bilayer squar) lattice, as the interchain (interlayer) hopping is large, an interchain (interlayer) antiferromagnetic spin correlation tends to be enhanced in real space, which corresponds to a peak value of spin structure factor around $\boldsymbol{Q} = (\pi, \pi)((\pi, \pi, \pi))$ in momentum space.

Moreover, the equal-time superconducting correlations are defined as

$$P_{\alpha}(\boldsymbol{r}) = \frac{1}{2N_{\mathrm{s}}} \sum_{\boldsymbol{r}_i} \langle \Delta_{\alpha}^{\dagger}(\boldsymbol{r}_i)\Delta_{\alpha}(\boldsymbol{r}_i + \boldsymbol{r}) + \Delta_{\alpha}(\boldsymbol{r}_i)\Delta_{\alpha}^{\dagger}(\boldsymbol{r}_i + \boldsymbol{r})\rangle.$$

Superconducting order parameters $\Delta_\alpha(\boldsymbol{r}_i)$ are defined as

$$\Delta_\alpha(\boldsymbol{r}_i) = \frac{1}{\sqrt{2}} \sum_{\boldsymbol{r}} f_\alpha(\boldsymbol{r})(c_{\boldsymbol{r}_i\uparrow} c_{\boldsymbol{r}_i+\boldsymbol{r}\downarrow} - c_{\boldsymbol{r}_i\downarrow} c_{\boldsymbol{r}_i+\boldsymbol{r}\uparrow}).$$

Here $f_\alpha(\boldsymbol{r})$, which is called the form factor, describes the symmetry of the superconducting pairing. For the partial d-wave pairing in the two-leg ladder chain lattice, we define

$$f_d(r_x, r_y) = \delta_{r_x,0}\delta_{r_y,1},$$

where δ_{ij} denotes the Kronecker's delta. For the $s^{\pm}$-wave pairing in the bilayer square lattice, we define

$$f_{s^\pm}(r_x, r_y, r_z) = \delta_{r_x,0}\delta_{r_y,0}\delta_{r_z,1}.$$

In order to decrease stochastic errors, long-range average of the superconducting correlation is evaluated, which is defined as

$$\overline{P}_\alpha = \frac{1}{M} \sum_{2<|\boldsymbol{r}|<r_{\max}} P_\alpha(\boldsymbol{r}),$$

where $r_{\max}$ is 30 ($6\sqrt{2}$) for the present two-leg ladder (bilayer) systems. M is the total number of vectors satisfying $2 < r < r_{\max}$. Here, we eliminate the short range part of the superconducting correlation since it does not reflect the off-diagonal ordering nature of superconductivity to diminish the effect of the boundary condition.

5.3 Results of two-leg Hubbard ladders

We begin with the two-leg Hubbard ladder with/without diagonal hopping. Figure 5.2a shows the inter-chain hopping dependence of several physical properties for $t'/t_{\mathrm{l}} = 0$ and $U/t_{\mathrm{l}} = 4$; peak value of the spin structure factor $S(\boldsymbol{q}_{\max})$, which is the square of the anti-ferromagnetic ordered moment, and average value of superconducting correlation $\overline{P}_d$ at long distance with the partial d symmetry, corresponding to the square of the superconducting order parameter. We also plot the momentum distribution function at the anti-bonding band minimum $n(0, \pi)$, which monitors whether or not the anti-bonding band intersects the Fermi level. For $1.2 \leq t_{\mathrm{r}}/t_{\mathrm{l}} \leq 1.6$, $n(0, \pi)$ decreases rapidly and $S(\boldsymbol{q}_{\max})$ is strongly suppressed as $t_{\mathrm{r}}/t_{\mathrm{l}}$ increases. The interchain spin correlation is strongly suppressed when one of bands gets away from the Fermi level. Thus, the incipient-band regime is estimated to be in a range of $1.2 \leq t_{\mathrm{r}}/t_{\mathrm{l}} \leq 1.6$. The incipient band is caused by the correlation effect since larger $t_{\mathrm{r}}/t_{\mathrm{l}}(> 2)$ is required for the bare antibonding band to go above the Fermi level at half-filling. In the incipient-band regime, $\overline{P}_d$ is maximized. Further, we find the dome structure of the partial d-wave superconducting correlation around $t_{\mathrm{r}}/t_{\mathrm{l}} \sim 1.5$, which is reminiscent of a previous FLEX result of the two-leg ladder Hubbard model without t' [105]. For $t'/t_{\mathrm{l}} = 0.4$, where wide and narrow bands coexist, the inter-chain hopping dependence of several physical properties are basically similar to those for $t'/t_{\mathrm{l}} = 0$ as shown in Fig. 5.2b. For a larger interaction value of $U/t_\mathrm{l} = 8$, the variation of $n(0, \pi)$ against $t_\mathrm{r}/t_\mathrm{l}$ becomes broad due to correlation effects as shown in Figs. 5.2c and 5.2d. In the hole-doped two-leg Hubbard ladder, as U increases, $n(0, \pi)$ decreases while $n(\pi, \pi)$ increases, and the momentum distribution function of the antibonding band becomes faint. On the other hand, a clear suppression of $S(\boldsymbol{q}_\mathrm{max})$ indicates the Lifshitz transition. Thus, superconductivity is optimized when one of bands becomes incipient also in the strongly correlated regime.

Further, Figure 5.3 shows $t_\mathrm{r}/t_\mathrm{l}$ dependence of the superconducting correlation $\overline{P}_d$ for various values of U/t_l. Both for $t'/t_\mathrm{l} = 0$ and $t'/t_\mathrm{l} = 0.4$, the regime in which the superconducting correlation is enhanced extends to smaller $t_\mathrm{r}/t_\mathrm{l}$ as U/t_l increases, probably due to band narrowing caused by U. In general, Hubbard U can narrow bands near the Fermi level and induce the Lifshitz transition [2]. We also verified that the parameter dependence of various physical quantities is qualitatively similar between the system with two system sizes, namely, 2x30 and 2x60 sites.

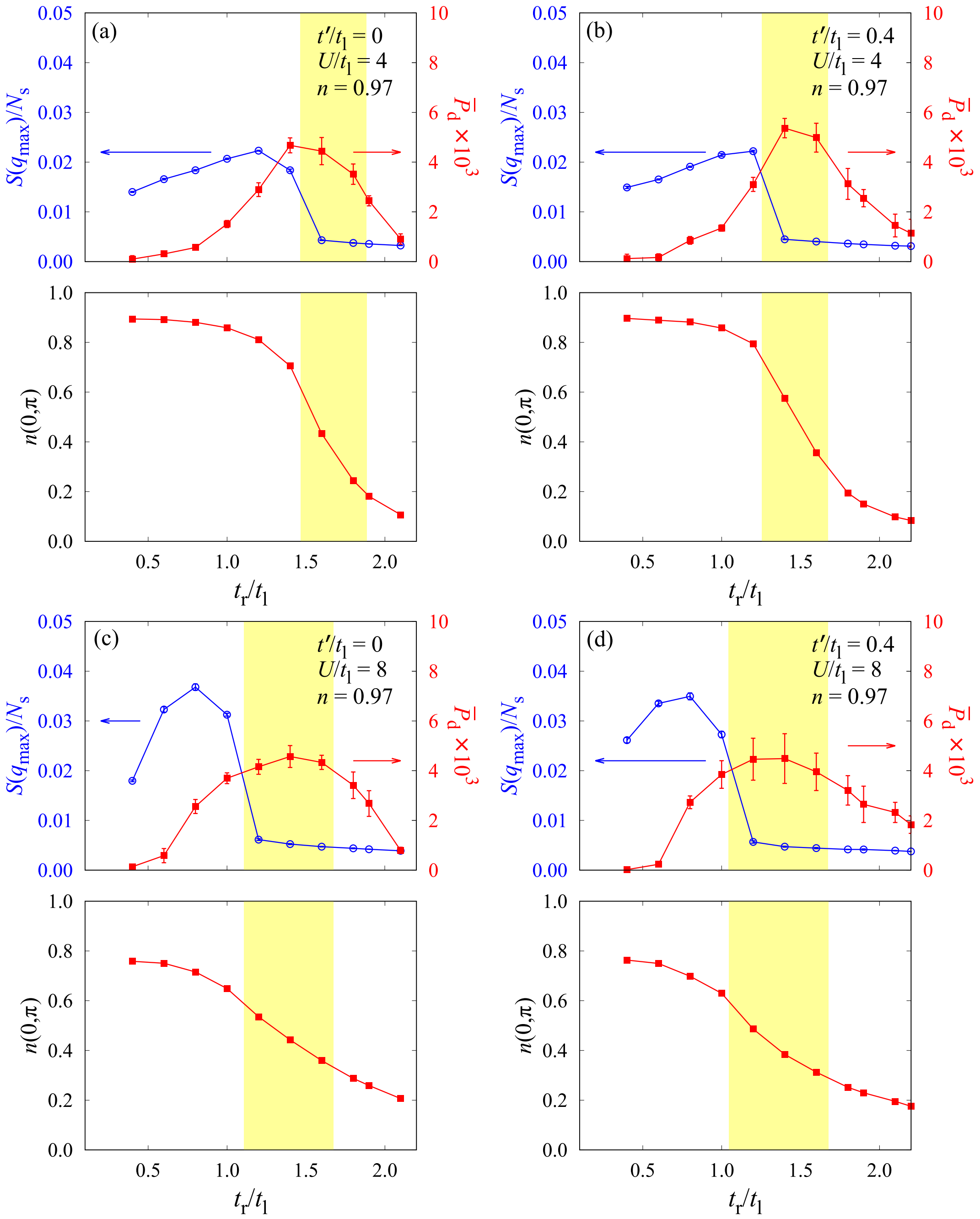

Fig. 5.2: (color online). Inter-chain hopping $t_\mathrm{r}/t_\mathrm{l}$ dependence of the averaged partial d-wave superconducting correlation $\overline{P}_d$ and the peak value of the spin structure factor $S(\boldsymbol{q}_\mathrm{max})$ (upper panels), the momentum distribution function of the anti-bonding band minimum $n(0,\pi)$ (lower panels) for the two-leg ladder model with (a) $t'/t_\mathrm{l} = 0$ and $U/t_\mathrm{l} = 4$, (b) $t'/t_\mathrm{l} = 0.4$ and $U/t_\mathrm{l} = 4$, (c) $t'/t_\mathrm{l} = 0$ and $U/t_\mathrm{l} = 8$, (d) $t'/t_\mathrm{l} = 0.4$ and $U/t_\mathrm{l} = 8$. The band filling is $n = 0.97$. The yellow region denotes the incipient-band regime. In the present plots and the plots in the later figures, the error bars indicate the estimated statistical errors of the Monte Carlo sampling.

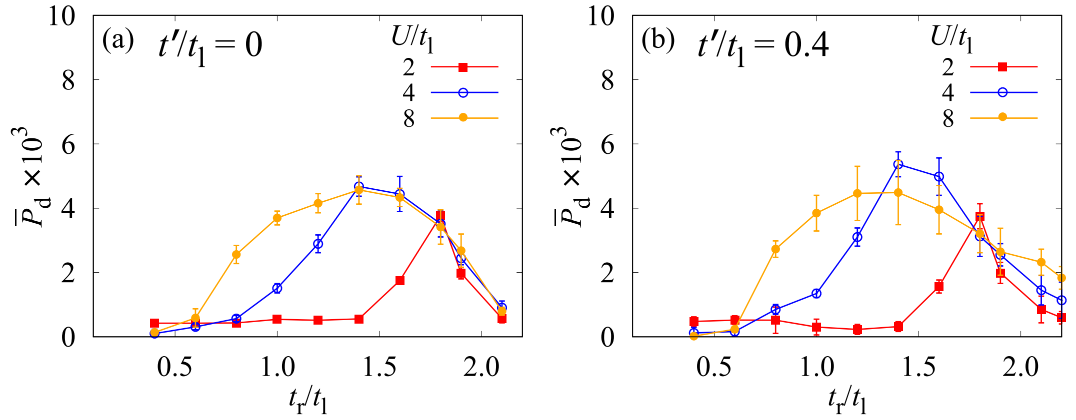

Fig. 5.3: (color online). $t_\mathrm{r}/t_\mathrm{l}$ dependence of $\overline{P}_d$ for the two-leg ladder model with various values of U/t_l and (a) $t'/t_\mathrm{l} = 0$, (b) $t'/t_\mathrm{l} = 0.4$. The band filling is $n = 0.97$.

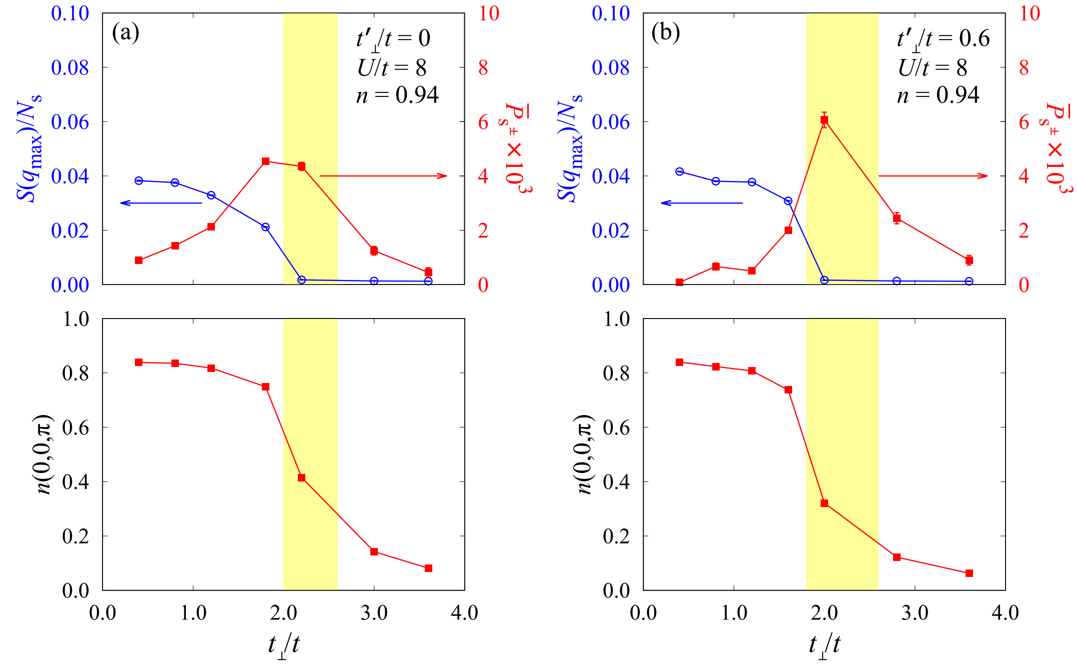

Fig. 5.4: (color online). Inter-layer hopping $t_\perp/t$ dependence of the averaged $s^\pm$-wave superconducting correlation $\overline{P}_{s^\pm}$ and the peak value of the spin structure factor $S(\boldsymbol{q}_\mathrm{max})$ (upper panels), the momentum distribution function of the anti-bonding minimum $n(0,0,\pi)$ (lower panels) for the bilayer model with (a) $t'_\perp/t = 0$ and $U/t = 8$, (b) $t'_\perp/t = 0.6$ and $U/t = 8$. The band filing is $n = 0.94$.

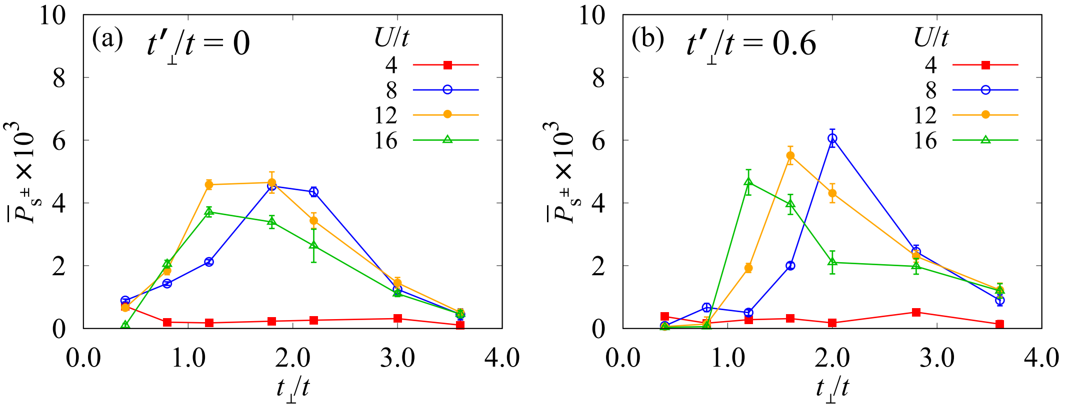

Fig. 5.5: (color online). $t_\perp/t$ dependence of $\overline{P}_{s^\pm}$ for the bilayer model with various values of U/t and (a) $t'_\perp/t = 0$, (b) $t'_\perp/t = 0.6$. The band filling is $n = 0.94$.

5.4 Results of bilayer Hubbard models

We next move on to the bilayer Hubbard model with/without diagonal hopping. Figure 5.4a shows the inter-layer hopping dependence of physical properties for $t'_\perp/t = 0$ and $U/t = 8$; the peak value of the spin structure factor $S(\boldsymbol{q}_{\max})$ and the average value of the superconducting correlation $\overline{P}_{s^\pm}$ at long distances with the s$^\pm$ symmetry. We also plot the momentum distribution function at the anti-bonding band minimum $n(0,0,\pi)$. For $t_\perp/t > 1.8$, $n(0,0,\pi)$ decreases steeply, and $S(\boldsymbol{q}_{\max})$ is strongly suppressed as $t_\perp/t$ increases. Thus, the incipient-band regime is estimated to be in a range of $1.8 \leq t_\perp/t \leq 2.4$. The incipient band is caused by the correlation effect since larger $t_\perp/t (> 4)$ is required for the bare antibonding band to go above the Fermi level at half-filling. Around the incipient-band regime, $\overline{P}_{s^\pm}$ is enhanced. We find a dome structure of the $s^\pm$-wave superconducting correlation around $t_\perp/t \sim 2.0$ [106], which resembles FLEX [52] and fRG [56], DCA [57] studies. For $t'_\perp/t = 0.6$, $t_\perp/t$ dependence of the physical properties are basically similar to those for $t'_\perp/t = 0$ as shown in Fig. 5.4b.

As in the two-leg ladder, we also study $t_\perp/t$ dependence of superconducting correlation $\overline{P}_{s^\pm}$ for various values of U/t as shown in Fig. 5.5. Both for $t'_\perp/t = 0$ and $t'_\perp/t = 0.6$, the regime of enhanced superconducting correlation extends to smaller $t_\perp/t$ as U/t increases in the same manner as the two-leg Hubbard ladder.

We note that $n(0,0,\pi)$ of the $U = 8t$ bilayer Hubbard model decreases steeper than $n(0,\pi)$ of the $U = 8t_{\mathrm{l}}$ two-leg Hubbard ladder, and in fact resembles that of $U = 4t_{\mathrm{l}}$ ladder. Because the broadness of the momentum distribution variation around the Lifshitz transition is presumably attributed to the correlation effect, the present result indicates the strength of the electron correlation is roughly determined by U/W, where W is the band width. We also verified that the parameter dependence of various physical quantities is qualitatively similar between the system with two system sizes, namely, 6x6x2 and 12x12x2 sites.

5.5 Discussion

These results demonstrate that superconductivity is enhanced in the incipient band regime regardless of whether the system is one- or two-dimensional, or whether one of the bare bands is narrow or not. Actually, there is resemblance between the present mVMC study and the recent FLEX studies [62, 68, 107]. In this section, we further discuss the commonalities and differences between the bilayer and two-leg ladder Hubbard models, referring previous studies. As mentioned in section 3.3, the low-lying spin fluctuation leads to strong renormalization and hence is "pair breaking", while the finite-energy spin fluctuation enhances T_c [69]. Thus, when the low-energy spin fluctuation is suppressed while the finite energy spin fluctuation is enhanced, superconductivity can be enhanced. Refs. [58, 59, 68] pointed out that the finite-energy spin fluctuations can enhance superconductivity in the bilayer Hubbard model. Moreover, quite recently, in ref. [68], the role played by the spin fluctuations in various energy ranges in two-band Hubbard models has been discussed as follows. In multi-band systems, as one of the bands moves away from the Fermi level, the spin-fluctuation spectral weight is transferred to higher energies. When the spin-fluctuation spectral weight is away from the critical frequency of spin fluctuations, but is within the paring cutoff energy, the pairing interaction can be strong without strong renormalization of quasiparticles. On the other hand, when the spin fluctuation is concentrated at very low or too high energies, superconductivity is degraded. From this viewpoint, we discuss the relation between the superconducting correlation calculated using the mVMC and the shape of the DOS of the antibonding band, based on results of the previous FLEX studies [62, 68] (see section 3).

One difference between the bilayer and the two-leg ladder observed in the present study is the U dependence of superconductivity. Namely, in the two-leg ladder, the superconducting correlation is enhanced even for $U/t_l = 2$ when the antibonding band is incipient, while such an enhancement is not obtained for the bilayer model for $U/t = 4$. Note that here we compare two cases where U normalized by the bare band width are the same. Actually, a similar result was obtained in the recent FLEX calculation (see Fig. 3.8 in section 3.3 [68]). There, it has been pointed out that in the bilayer model, the correlation effect reduces the width of the incipient band [2], which makes more spin fluctuation weight lie within the energy regime effective for pairing. In the two-leg ladder, such effect is not necessary for the superconductivity to be enhanced when the antibonding band is incipient because in a one-dimensional system, DOS is diverging at the band edge (see Fig. 5.6).

Another point that we notice, if we look closely, is that in the two-leg ladder, the superconducting correlation, maximized around the incipient-band regime, is reduced as t_r/t_l decreases and the antibonding band intersects the Fermi level, but does so rather mildly and smoothly especially for $U = 8t_l$, whereas the reduction of the superconducting correlation in the bilayer model upon reducing $t_\perp$ occurs rapidly after the antibonding band intersects the Fermi level. If we compare in more detail the two cases for the bilayer model, the reduction of the superconducting correlation is more abrupt for the

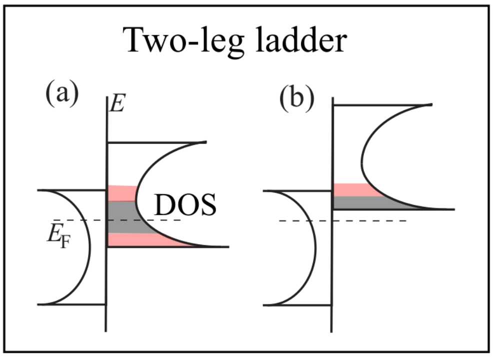

Fig. 5.6: Typical density of states of the two-leg ladder Hubbard model. In each figure, the left (right) side of the vertical line depicts the DOS of the bonding (antibonding) band. The gray area denotes the portion of the bonding band DOS which gives rise to the low-lying pair breaking spin fluctuations, and the red area is the portion of the antibonding band DOS contributing to the spin fluctuations which mediate pairings. (a) when both bands intersect the Fermi level, and (b) when the antibonding band is incipient.

case with $t'_\perp = 0.6$. These differences can again be understood from the shape of the DOS (see Figs. 5.6 and 5.7). Namely, in the two-leg ladder, where the DOS at the band edge is diverging, the DOS at the Fermi level decreases (rapidly, especially for large U because the band width shrinks due to renormalization) as t_r is reduced after the antibonding band intersects the Fermi level, so that the pair-breaking low-energy spin fluctuations become weaker. By contrast, in the bilayer model, where the DOS is diverging around the middle of the antibonding band, the DOS at the Fermi level increases upon reducing $t_\perp$ after the antibonding Fermi surface is formed, resulting in an increase of the pair-breaking spin fluctuations. The diverging DOS of the antibonding band approaches the Fermi level "faster" when $t'_\perp$ is finite, so that the superconducting correlation is rapidly suppressed for the case of $t'_\perp = 0.6$ as $t_\perp$ is reduced. A similar analysis has been performed in ref. [68], not for the $t_\mathrm{r}, t_\perp$ variation, but for the $t'(t'_\perp)$ variation of superconductivity as was mentioned in section 3 (comparison between Figs. 3.5 and 3.6).

5.6 Summary

To summarize, we have studied superconductivity in the Hubbard model on the two-leg ladder and bilayer square lattices. In both systems, superconductivity can be optimized in a region around the Lifshitz point, where one of the bands is (nearly) incipient. The parameter dependence of the superconducting correlation function is reminiscent of the FLEX results obtained in ref. [68]. What is noteworthy is the important role played by an incipient band in the occurrence of superconductivity in the strong coupling regime.

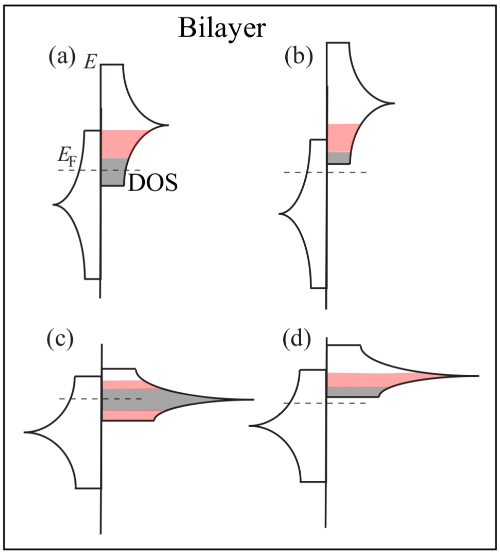

Fig. 5.7: Typical density of states for the bilayer Hubbard model. (a)(b) when $t'_{\perp}/t$ is (nearly) zero, and (c)(d) when $t'_{\perp}/t$ is finite. (a)(c) when both bands intersect the Fermi level, and (b)(d) when the antibonding band is incipient.

The present result suggests that the following view holds not only in the weak coupling regime but also in the strong coupling regime as well: superconductivity is enhanced by an incipient band due to the suppression of the near-zero-energy spin fluctuations and enhanced finite energy spin fluctuations working as an effective pairing glue. We also stress that the resemblance between the two approaches is highly nontrivial because FLEX is based on a weak coupling perturbational theory, which takes into account the spin fluctuations (in momentum space) explicitly in the effective interaction, whereas the present mVMC method takes into account the electron correlation effect in a real-space-based manner, which is expected to be more appropriate in the strong coupling regime. Since it has been shown that incipient bands enhance superconductivity in other models [2, 62–67], it is an interesting future problem to study those models using the mVMC method.

6 Two-orbital Hubbard models on one-dimensional chain and square lattices

6.1 Motivation

In the previous section, motivated by the iron-based superconductors with "incipient bands" [18, 31, 33, 35–40], we studied superconductivity in two-band systems, such as the two-leg ladder and bilayer Hubbard models. The bilayer Hubbard model can be regarded as a single-orbital analogue of the iron-based superconductors. In this section, we revisit superconductivity in two-orbital systems with the incipient band. In multi-orbital systems, interorbital interactions can induce charge orders and exotic quantum states, such as a spin-triplet pairing (e.g. [108–110]) and orbital selective Mott phase (e.g. [111]). Further, the hybridization effect significantly changes the band structure and the Fermi surface, the orbital weights. Thus, the nature of multi-orbital systems generally differs from that of single-orbital systems. However, there is a possible similarity between multi-orbital systems and single-orbital systems with multi bands caused by multi sites within a unit cell. For example, in some of the iron-based superconductors, the d-wave and $s^{\pm}$-wave pairings may be closely competing, which is also the case with the single-orbital analogue, namely, the bilayer Hubbard model. Moreover, some theoretical studies suggest that there are two orbitals near the Fermi level in a unique type of cuprate superconductors, such as a $\mathrm{CuO_2}$ monolayer on Bi2212 superconductors [112], $\mathrm{Sr_2CuO_{3+\delta}}$ [113–115], $\mathrm{Ba_2CuO_{3+\delta}}$ [116], and so on (cf. [117]). Motivated by these materials, weak-coupling studies showed significant pairing strength in the $d_{x^2-y^2}$-wave and $s^{\pm}$-wave channels in a two-orbital Hubbard model on square [110, 118, 119] and Lieb [120] lattices, which are possible models of the unique type of cuprate superconductors. These pairing symmetries are also the same as those in the iron-based superconductors and the bilayer Hubbard model. In this section, we study two-orbital Hubbard models on the one-dimensional chain and two-dimensional square lattices using a mVMC method [70, 71] in order to discuss the commodities and differences between the multi-orbital systems and single-orbital systems with multi sites.

6.2 Models

The two-orbital Hubbard model is defined as

$$\begin{aligned}\hat{H} = &\sum_{\boldsymbol{k},\alpha,\beta,\sigma} \varepsilon_{\alpha\beta}(\boldsymbol{k}) c^{\dagger}_{\boldsymbol{k}\alpha\sigma} c_{\boldsymbol{k}\beta\sigma} + U \sum_{i\alpha} n_{i\alpha\uparrow} n_{i\alpha\downarrow} \\ &+ \sum_{i,\alpha<\beta,\sigma} \left[U' n_{i\alpha\sigma} n_{i\beta\bar{\sigma}} + (U' - J) n_{i\alpha\sigma} n_{i\beta\sigma} \right] \\ &+ J \sum_{i,\alpha<\beta} (c^{\dagger}_{i\alpha\uparrow} c^{\dagger}_{i\beta\downarrow} c_{i\alpha\downarrow} c_{i\beta\uparrow} + c^{\dagger}_{i\alpha\uparrow} c^{\dagger}_{i\alpha\downarrow} c_{i\beta\downarrow} c_{i\beta\uparrow} + \text{H.c.}). \end{aligned} \tag{6.2.1}$$

Here $c^{\dagger}_{i\alpha\sigma}/c_{i\alpha\sigma}$ creates/annihilates a fermion with spin $\sigma(=\uparrow,\downarrow)$ and $\alpha^{\text{th}}(= 0 : x^2 - y^2, 1 : z^2)$ orbital, $n_{i\alpha\sigma} = c^{\dagger}_{i\alpha\sigma} c_{i\alpha\sigma}$, and $c^{\dagger}_{\boldsymbol{k}\alpha\sigma}$ is the Fourier transformation of $c^{\dagger}_{i\alpha\sigma}$. U and U' denote the intra and inter orbital Coulomb repulsions, respectively. J denotes the spin-flip and pair-hopping interaction, called Hund's coupling (see Fig. 6.1). We employ the following kinetic term

$$\hat{H}_{\text{kin}}(\boldsymbol{k}) = \begin{pmatrix} \varepsilon_{00}(\boldsymbol{k}) & \varepsilon_{01}(\boldsymbol{k}) \\ \varepsilon_{10}(\boldsymbol{k}) & \varepsilon_{11}(\boldsymbol{k}) \end{pmatrix} = \begin{pmatrix} \varepsilon_{\boldsymbol{k}} & \varepsilon'_{\boldsymbol{k}} \\ \varepsilon'_{\boldsymbol{k}} & \varepsilon_{\boldsymbol{k}} + \Delta \end{pmatrix}, \tag{6.2.2}$$

where $\varepsilon_{\boldsymbol{k}}$ and $\varepsilon'_{\boldsymbol{k}}$ denote band dispersion originating from intra and inter orbital hopping integrals, respectively. Δ is the energy difference between two-orbitals.

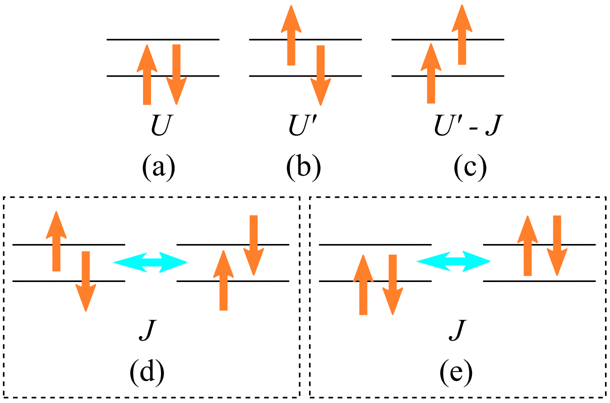

Fig. 6.1: Electron-electron interactions in multiorbital systems; (a) intraorbital Coulomb interaction, (b)(c) interorbital Coulomb interactions, (d) spin-flip process, (e) pair-hopping process.

After diagonalizing $\hat{H}_{\text{kin}}(\boldsymbol{k})$, the band dispersion is given by

$$\begin{cases} \varepsilon_b(\boldsymbol{k}) = \varepsilon_{\boldsymbol{k}} + \dfrac{\Delta}{2} - \sqrt{{\varepsilon'_{\boldsymbol{k}}}^2 + \dfrac{\Delta^2}{4}} \\ \varepsilon_a(\boldsymbol{k}) = \varepsilon_{\boldsymbol{k}} + \dfrac{\Delta}{2} + \sqrt{{\varepsilon'_{\boldsymbol{k}}}^2 + \dfrac{\Delta^2}{4}} \end{cases}. \tag{6.2.3}$$

The operators $\{d^\dagger_{\boldsymbol{k}b\sigma}, d^\dagger_{\boldsymbol{k}a\sigma}\}$ ($\{d_{\boldsymbol{k}b\sigma}, d_{\boldsymbol{k}a\sigma}\}$) are creation (annihilation) operators for the electrons on bonding and antibonding bands, respectively. These operators are given by using an unitary transformation $d_{\boldsymbol{k}p\sigma} = [\Lambda_{\boldsymbol{k}}]_{p\alpha} c_{\boldsymbol{k}\alpha\sigma}, d^\dagger_{\boldsymbol{k}\alpha\sigma} = [\Lambda^\dagger_{\boldsymbol{k}}]_{\alpha p} c_{\boldsymbol{k}\alpha\sigma}$ $(p = b, a)$ as follows,

$$\begin{cases} d^\dagger_{\boldsymbol{k}b\sigma} = u_{\boldsymbol{k}} c^\dagger_{\boldsymbol{k}0\sigma} + v_{\boldsymbol{k}} c^\dagger_{\boldsymbol{k}1\sigma} \\ d^\dagger_{\boldsymbol{k}a\sigma} = -v_{\boldsymbol{k}} c^\dagger_{\boldsymbol{k}0\sigma} + u_{\boldsymbol{k}} c^\dagger_{\boldsymbol{k}1\sigma} \end{cases}, \tag{6.2.4}$$

with

$$u^2_{\boldsymbol{k}} = \frac{1}{2}\left(1 + \frac{\Delta/2}{\sqrt{{\varepsilon'_{\boldsymbol{k}}}^2 + \Delta^2/4}}\right) \tag{6.2.5}$$

$$v^2_{\boldsymbol{k}} = \frac{1}{2}\left(1 - \frac{\Delta/2}{\sqrt{{\varepsilon'_{\boldsymbol{k}}}^2 + \Delta^2/4}}\right). \tag{6.2.6}$$

Further, $u_{\boldsymbol{k}}$ and $v_{\boldsymbol{k}}$ are assumed to satisfy the following relations:

$$u^2_{\boldsymbol{k}} + v^2_{\boldsymbol{k}} = 1, \quad u_{\boldsymbol{k}} = u_{-\boldsymbol{k}}, \quad v_{\boldsymbol{k}} = v_{-\boldsymbol{k}}. \tag{6.2.7}$$

In the limit $\Delta \to \infty$, the operators $d^\dagger_{\boldsymbol{k}b\sigma}$ and $d^\dagger_{\boldsymbol{k}a\sigma}$ are reduced to $c^\dagger_{\boldsymbol{k}0\sigma}$ and $c^\dagger_{\boldsymbol{k}1\sigma}$, respectively. We employ a two-orbital Hubbard model on the one-dimensional chain, in which the band dispersion is defined as

$$\begin{cases} \varepsilon(k) = -2t\cos k \\ \varepsilon'(k) = -2t'\cos k \end{cases}, \tag{6.2.8}$$

where t and t' denote the nearest intra and inter orbital hopping integrals. We also employ a two-orbital Hubbard model on the square lattice, in which the band dispersion is defined as

$$\begin{cases} \varepsilon(\boldsymbol{k}) = -2t(\cos k_x + \cos k_y) \\ \varepsilon'(\boldsymbol{k}) = -2t'(\cos k_x - \cos k_y) \end{cases}, \tag{6.2.9}$$

where t and t' denote the nearest intra and inter orbital hopping integrals (see Fig. 6.2). Due to the d-wave symmetry of the hybridization between $d_{x^2-y^2}$ and d_{z^2} orbitals, the sign of the interorbital hopping integral is reversed between the x and y directions.

In order to demonstrate the hopping dependence of the band structure of two-orbital systems, we begins with two special cases, namely, when the on-site energy is zero ($\Delta = 0$), and when the interorbital nearest neighbor hopping is zero ($t' = 0$). For $\Delta = 0$, the two orbital states are mixed at a ratio of one-to-one for each band. In the case of the two-orbital one-dimensional chain, as t' increases, one of the bands becomes wider than the other as shown in Fig. 6.3. The definition of the bonding and antibonding bands is then given in Fig. 6.3. On the other hand, in the case of the two-orbital square lattice, the anisotropy of the bands is induced, which affects the shape of the DOS as shown in Fig. 6.4. Especially, for $t' = 1$, the band structure is one-dimensional. In this

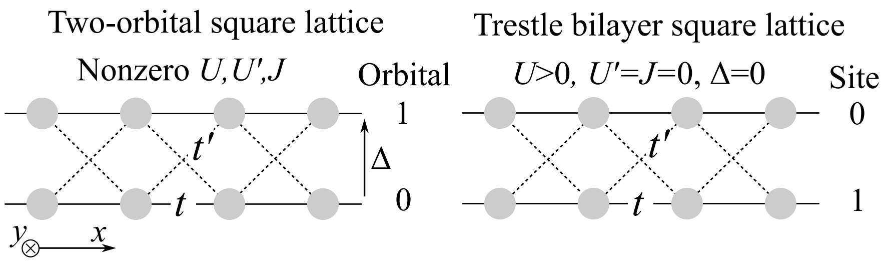

Fig. 6.2: The two-orbital square lattice (left panel) and the trestle bilayer square lattice (right panel) on the xz-plane, where "z" are the orbital and site indexes, respectively.

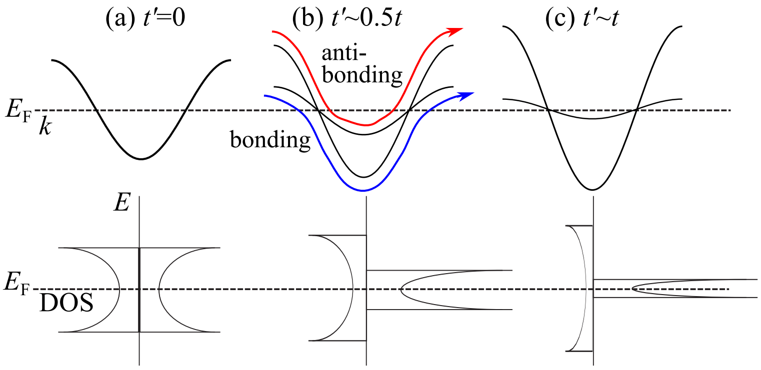

Fig. 6.3: Typical band structures (upper panels) and density of states (lower panels) of the two-orbital one-dimensional Hubbard chain without the on-site energy ($\Delta = 0$) for various values of t'; (a) $t' = 0$, (b) $t' \sim 0.5t$, (c) $t' \sim t$, for half filling. The dashed line represents the Fermi level. In each lower panel, the left (right) side of the vertical line depicts the DOS of the wide (narrow) band. The red (blue) arrow indicates the antibonding (bonding) band.

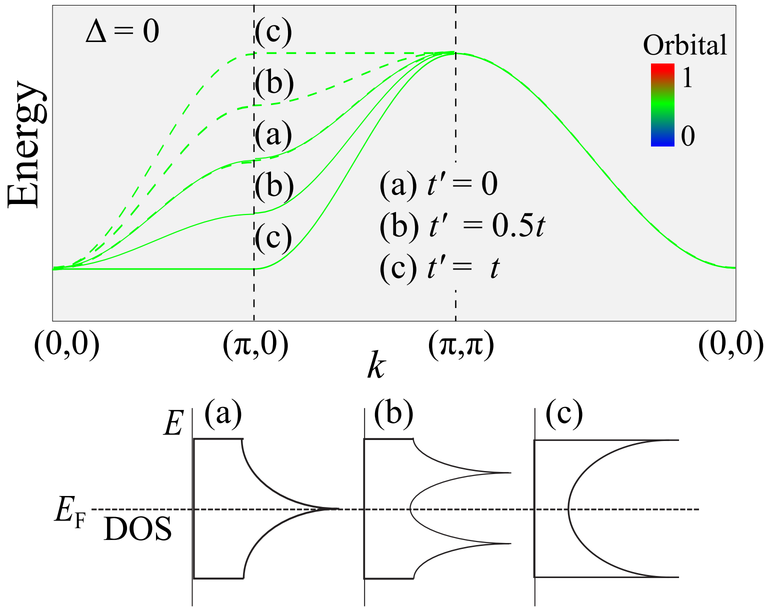

Fig. 6.4: (color online). Typical band structures (upper panel) and density of states (lower panels) of the two-orbital Hubbard model on the square lattice without the on-site energy ($\Delta = 0$) for various values of t'; (a) $t' = 0$, (b) $t' = 0.5t$, (c) $t' = t$, for half filling. In the upper panel, the solid (dashed) line represents the bonding (antibonding) band. The definition of the bonding and antibonding bands is explained in the main text.In each lower panel, the vertical line depicts the DOS of both the bonding and antibonding band. The color band indicates the orbital weights for orbital 0 and 1.

case, the bonding and antibonding bands are not defined since both two bands have the same shape of the DOS and different momentum dependencies. Only in this case, the antibonding (bonding) band means the band which mainly depends on $k_x(k_y)$ rather than $k_y(k_x)$.Further, $n_\mathrm{a}(k,k) = n_\mathrm{b}(k,k)$. Next, we consider the case of $t' = 0$, where both of bands are isotropic. In the case of the two-orbital models on the square (one-dimensional chain) lattice at half filling, the bare antibonding band gets away from the Fermi level for $\Delta > 8t(4t)$ as shown in Fig. 6.5. Further, we consider the two-orbital system on the square lattice with $\Delta > 0$ and $t' > 0$, where the bands are anisotropic and the orbital states are mixed around momentums $\boldsymbol{k} = (0,\pi),(\pi,0)$ (see Fig. 6.6). In the two-leg ladder and bilayer square lattices, if the site index is regarded as the orbital index, the two orbital (site) states are mixed for each band while in the two-orbital one-dimensional chain and square lattices, the bonding (antibonding) band is mainly originating from orbital 0 (1). The several nestings among disconnected pieces of the electron-like and hole-like Fermi surfaces made of the “same orbitals”, combined with “intraorbital” Coulomb repulsion U, induces interband spin fluctuations, which can lead to pairing interactions around certain wave vectors. This possible pairing mechanism is also the case with the iron-based superconductors [17, 121–123]. Thus, when one of the bands is incipient, superconductivity can be enhanced in the same way as the bilayer Hubbard model.

Particularly noteworthy is the case with $U' = J = 0$ and $\Delta \ll t$, where the two-orbital system corresponds to the trestle two-leg ladder (bilayer) Hubbard model with the nearest-intra and next-nearest-inter chain (layer) hopping integrals t and t', respectively (see Fig. 6.2). Studying these trestle lattices allows us to investigate the relation between the two-orbital systems and the two-band systems with multi-sites.

We take $N_\mathrm{s} = 2 \times 2L$ $(2 \times 2L \times 2L)$ sites for the two-orbital one-dimensional chain (square lattice) Hubbard model with the antiperiodic-periodic boundary condition in x (y) direction. The band filling is defined as number of electrons per orbital, namely, $n = N_\mathrm{e}/N_\mathrm{s}$ where $N_\mathrm{e} = \sum_{i\alpha\sigma} n_{i\alpha\sigma}$. The half filling corresponds to $n = 1$ in the present study.

6.3 Method

To study the ground state of these Hubbard models, we employ a mVMC method [70, 71], which can describe the strong correlation and various ordering fluctuations accurately. Our variational wave function is defined as

$$|\phi\rangle = \mathcal{P}_\mathrm{G}\mathcal{P}_\mathrm{J}|\phi_\mathrm{pair}\rangle, \tag{6.3.1}$$

where $\mathcal{P}_\mathrm{G}, \mathcal{P}_\mathrm{J}$ are the multi-orbital Gutzwiller and Jastrow correlation factors, respectively. The Gutzwiller factor is defined as

$$\mathcal{P}_\mathrm{G} = \exp\left(-\frac{1}{2}\sum_{i\alpha} g_{i\alpha} n_{i\alpha\uparrow} n_{i\alpha\downarrow}\right). \tag{6.3.2}$$

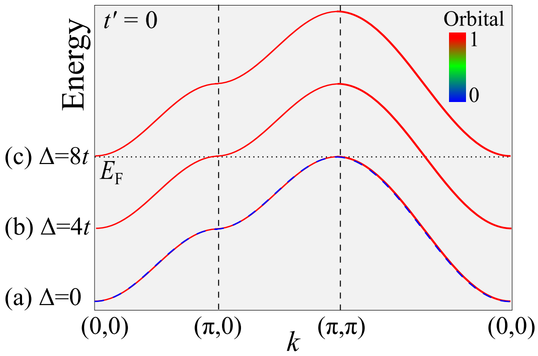

Fig. 6.5: (color online). Typical band structures of the two-orbital Hubbard model on the square lattice without interorbital nearest neighbor hopping ($t' = 0$) for various values of the on-site energy; (a) $\Delta = 0$, (b) $\Delta = 4t$, (c) $\Delta = 8t$. The band originating from orbital 0 (1) is depicted by the dashed blue (solid red) line.

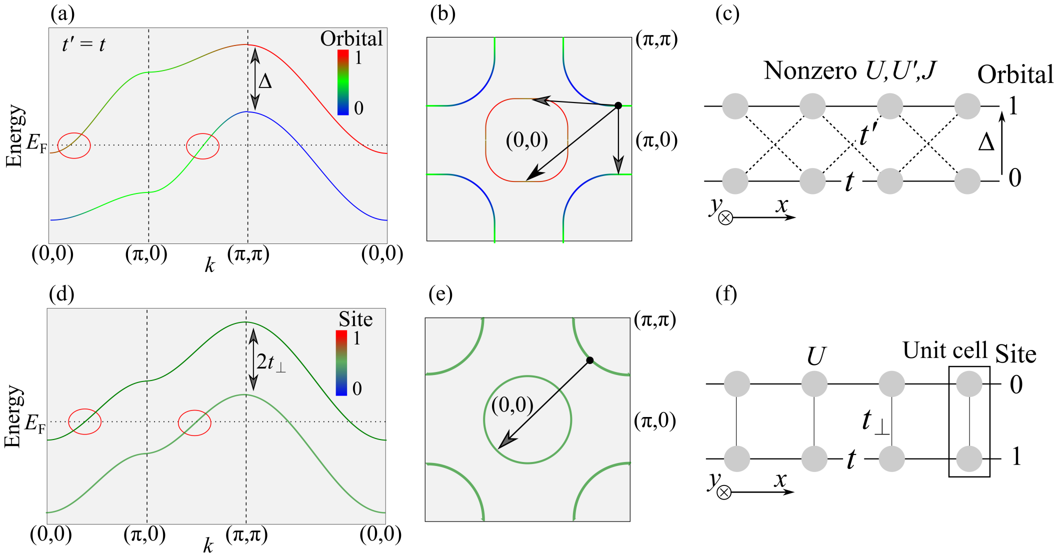

Fig. 6.6: (color online). Upper panels: (a) Typical band structure and (b) Fermi surface, (c) lattice structure of the two-orbital Hubbard model on the square lattice. In panel (a), The red circles depicts the portion of the bands presumably contributing to the interband pairing. In panel (b), the black arrows are nesting vectors. Lower panels: (d) Typical band structure and (e) Fermi surface, (f) lattice structure of the bilayer Hubbard model on the square lattice.

The Jastrow factor is defined as

$$\mathcal{P}_{\mathrm{J}} = \exp\left(-\frac{1}{2} \sum_{i\alpha} \sum_{j\beta} v_{i\alpha,j\beta} n_{i\alpha} n_{j\beta} \right), \tag{6.3.3}$$

where $n_{i\alpha} = \sum_{\sigma} n_{i\alpha\sigma}$. To study a possible superconducting state, we consider the following BCS-type Hamiltonian,

$$\begin{aligned} \hat{H}_{\mathrm{BCS}} =& \sum_{\boldsymbol{k}} \left(d^{\dagger}_{\boldsymbol{k}a\uparrow}, d^{\dagger}_{\boldsymbol{k}b\uparrow}, d_{-\boldsymbol{k}a\downarrow}, d_{-\boldsymbol{k}b\downarrow} \right) \\ & \times \begin{pmatrix} \xi_a(\boldsymbol{k}) & 0 & \Delta_{aa}(\boldsymbol{k}) & \Delta_{ab}(\boldsymbol{k}) \\ 0 & \xi_b(\boldsymbol{k}) & \Delta_{ba}(\boldsymbol{k}) & \Delta_{bb}(\boldsymbol{k}) \\ \Delta^*_{aa}(\boldsymbol{k}) & \Delta^*_{ba}(\boldsymbol{k}) & -\xi_a(\boldsymbol{k}) & 0 \\ \Delta^*_{ab}(\boldsymbol{k}) & \Delta^*_{bb}(\boldsymbol{k}) & 0 & -\xi_b(\boldsymbol{k}) \end{pmatrix} \begin{pmatrix} d_{\boldsymbol{k}a\uparrow} \\ d_{\boldsymbol{k}b\uparrow} \\ d^{\dagger}_{-\boldsymbol{k}a\downarrow} \\ d^{\dagger}_{-\boldsymbol{k}b\downarrow} \end{pmatrix}, \end{aligned} \tag{6.3.4}$$

where the operators $\{d^{\dagger}_{\boldsymbol{k}b\sigma}, d^{\dagger}_{\boldsymbol{k}a\sigma}\}$ ($\{d_{\boldsymbol{k}b\sigma}, d_{\boldsymbol{k}a\sigma}\}$) are creation (annihilation) operators for the electrons on bonding and antibonding bands respectively. $\xi_p(\boldsymbol{k})$ is the band dispersion measured from the chemical potential μ ($\xi_p(\boldsymbol{k}) = \varepsilon_p(\boldsymbol{k}) - \mu$) and $\Delta_{pq}(\boldsymbol{k})$ are the gap functions ($p, q = a, b$). After diagonalizing $\hat{H}_{\mathrm{BCS}}$, the ground state of the superconducting state is given by

$$|\phi_{\mathrm{BCS}}\rangle = \left(\sum_{\boldsymbol{k}\in\mathrm{BZ}} \sum_{p,q} \varphi_{pq}(\boldsymbol{k}) d^{\dagger}_{\boldsymbol{k}p\uparrow} d^{\dagger}_{-\boldsymbol{k}q\downarrow} \right)^{N_{\mathrm{e}}/2} |0\rangle. \tag{6.3.5}$$

For actual calculations, the following real space representation is employed,

$$|\phi_{\mathrm{pair}}\rangle = \left[\sum_{i,j=1}^{N_{\mathrm{c}}} \sum_{\alpha,\beta} f_{i\alpha,j\beta} c^{\dagger}_{i\alpha\uparrow} c^{\dagger}_{j\beta\downarrow} \right]^{N_{\mathrm{e}}/2} |0\rangle, \tag{6.3.6}$$

with

$$f_{i\alpha,j\beta} = \frac{1}{N_{\mathrm{c}}} \sum_{\boldsymbol{k}} \tilde{\varphi}_{\alpha\beta}(\boldsymbol{k}) \exp\left[i\boldsymbol{k} \cdot (\boldsymbol{r}_i - \boldsymbol{r}_j) \right] \tag{6.3.7}$$

$$\tilde{\varphi}_{\alpha\beta}(\boldsymbol{k}) = \sum_{p,q} \varphi_{pq}(\boldsymbol{k}) [\Lambda^{\dagger}_{\boldsymbol{k}}]_{p\alpha} [\Lambda^{\dagger}_{-\boldsymbol{k}}]_{q\beta}, \tag{6.3.8}$$

where $\Lambda^{\dagger}_{\boldsymbol{k}}$ are shown in Eqs. 6.2.4 and 6.2.6. N_{c} is the total number of cells in a supercell and N_{s} is the total number of sites ($N_{\mathrm{s}} = 2N_{\mathrm{c}}$). $f_{i\alpha,j\beta}$ is assumed to have 2 (2x2) sublattice structure or equivalently $2 \times N_{\mathrm{s}}$ ($4 \times N_{\mathrm{s}}$) independent variational parameters for one-body part in the two-orbital one-dimensional chain (square lattice) systems. The variational parameters are simultaneously optimized to minimize the variational energy by using the stochastic reconfiguration method [73].

6.4 Definition of physical quantities

To investigate the ground state properties of these Hubbard models, we calculate the momentum distribution function and spin-structure factor, equal-time superconducting correlation. The momentum distribution function is defined as

$$n_{\alpha\beta\sigma}(\boldsymbol{q}) = \frac{1}{N_{\mathrm{s}}}\sum_{i,j}\langle c^{\dagger}_{i\alpha\sigma}c_{j\beta\sigma}\rangle \exp\left[i\boldsymbol{q}\cdot(\boldsymbol{r}_{i\alpha\sigma}-\boldsymbol{r}_{j\beta\sigma})\right], \tag{6.4.1}$$

$$\tag{6.4.2}$$

where α and β denote orbital indexes. The momentum distribution functions of the bonding and antibonding bands are

$$n_{\boldsymbol{k}b\sigma}(\boldsymbol{q}) = u_{\boldsymbol{k}}^2 c^{\dagger}_{\boldsymbol{k}0\sigma}c_{\boldsymbol{k}0\sigma} + v_{\boldsymbol{k}}^2 c^{\dagger}_{\boldsymbol{k}1\sigma}c_{\boldsymbol{k}1\sigma} + u_{\boldsymbol{k}}v_{\boldsymbol{k}}(c^{\dagger}_{\boldsymbol{k}0\sigma}c_{\boldsymbol{k}1\sigma} + c^{\dagger}_{\boldsymbol{k}1\sigma}c_{\boldsymbol{k}0\sigma}), \tag{6.4.3}$$

$$n_{\boldsymbol{k}a\sigma}(\boldsymbol{q}) = v_{\boldsymbol{k}}^2 c^{\dagger}_{\boldsymbol{k}0\sigma}c_{\boldsymbol{k}0\sigma} + u_{\boldsymbol{k}}^2 c^{\dagger}_{\boldsymbol{k}1\sigma}c_{\boldsymbol{k}1\sigma} - u_{\boldsymbol{k}}v_{\boldsymbol{k}}(c^{\dagger}_{\boldsymbol{k}0\sigma}c_{\boldsymbol{k}1\sigma} + c^{\dagger}_{\boldsymbol{k}1\sigma}c_{\boldsymbol{k}0\sigma}). \tag{6.4.4}$$

The spin-structure factor is defined as

$$S^z_{\alpha\beta}(\boldsymbol{q}) = \frac{1}{N_{\mathrm{s}}}\sum_{i,j}\langle S^z_{i\alpha}S^z_{j\beta}\rangle \exp\left[i\boldsymbol{q}\cdot(\boldsymbol{r}_{i\alpha\sigma}-\boldsymbol{r}_{j\beta\sigma})\right], \tag{6.4.5}$$

$$S^{\pm}_{\alpha\beta}(\boldsymbol{q}) = \frac{1}{N_{\mathrm{s}}}\sum_{i,j}\langle S^+_{i\alpha}S^-_{j\beta}\rangle \exp\left[i\boldsymbol{q}\cdot(\boldsymbol{r}_{i\alpha\sigma}-\boldsymbol{r}_{j\beta\sigma})\right], \tag{6.4.6}$$

$$S_{\alpha\beta}(\boldsymbol{q}) = \frac{1}{3N_{\mathrm{s}}}\sum_{i,j}\langle \boldsymbol{S}_{i\alpha}\cdot\boldsymbol{S}_{j\beta}\rangle \exp\left[i\boldsymbol{q}\cdot(\boldsymbol{r}_{i\alpha\sigma}-\boldsymbol{r}_{j\beta\sigma})\right], \tag{6.4.7}$$

with

$$\boldsymbol{S}_{i\alpha}(\boldsymbol{q}) = \frac{1}{2}\sum_{\sigma\sigma'} c^{\dagger}_{i\alpha\sigma}\boldsymbol{\sigma}_{\sigma\sigma'}c_{i\alpha\sigma'}.$$

Further, the equal-time superconducting correlations are defined as

$$P_{\mu,\alpha\beta}(\boldsymbol{r}) = \frac{1}{2N_{\mathrm{s}}}\sum_{\boldsymbol{r}_i}\langle \Delta^{\dagger}_{\mu,\alpha\beta}(\boldsymbol{r}_i)\Delta_{\mu,\alpha\beta}(\boldsymbol{r}_i+\boldsymbol{r}) + \Delta_{\mu,\alpha\beta}(\boldsymbol{r}_i)\Delta^{\dagger}_{\mu,\alpha\beta}(\boldsymbol{r}_i+\boldsymbol{r})\rangle.$$

where μ denotes the pairing symmetry. In actual calculations, the summation with respect $\boldsymbol{r}_i$ is restricted to $\boldsymbol{r}_i = 0$ to reduce the numerical cost. Superconducting order parameters $\Delta_{\mu}(\boldsymbol{r}_i)$ are defined as

$$\Delta_{\mu,\alpha\beta}(\boldsymbol{r}_i) = \frac{1}{\sqrt{2}}\sum_{\boldsymbol{r}} f_{\mu,\alpha\beta}(\boldsymbol{r})(c_{\boldsymbol{r}_i\alpha\uparrow}c_{\boldsymbol{r}_i+\boldsymbol{r}\beta\downarrow} - c_{\boldsymbol{r}_i\alpha\downarrow}c_{\boldsymbol{r}_i+\boldsymbol{r}\beta\uparrow}).$$

Here $f_{\mu,\alpha\beta}(\boldsymbol{r})$ is the form factor that describes the symmetry of the superconductivity. For the d-wave superconductivity in the two-orbital one-dimensional chain, we define

$$f_{d,\alpha\beta}(x) = \delta_{x,1} + \delta_{x,-1},$$

where δ_{ij} denotes the Kronecker's delta. For the s-wave superconductivity in the two-orbital one-dimensional chain, we define

$$f_{s,\alpha\beta}(x) = \delta_{x,0}.$$

For the $d_{x^2-y^2}$-wave superconductivity in the two-orbital square lattice, we define

$$f_{d,\alpha\beta}(x,y) = \delta_{x,0}(\delta_{y,1} + \delta_{y,-1}) - \mathrm{sgn}_{\alpha\beta}\delta_{y,0}(\delta_{x,1} + \delta_{x,-1}),$$

where $\mathrm{sgn}_{\alpha\beta}$ denotes the sign change caused by the d-wave symmetry of the hybridization between orbital 0 and orbital 1, namely, $\mathrm{sgn}_{\alpha\beta} = +1$ for $\alpha = \beta$ and $\mathrm{sgn}_{\alpha\beta} = -1$ otherwise. For the extended s-wave superconductivity in the two-orbital square lattice, we define

$$f_{s^*,\alpha\beta}(x,y) = \delta_{x,0}(\delta_{y,1} + \delta_{y,-1}) + \mathrm{sgn}_{\alpha\beta}\delta_{y,0}(\delta_{x,1} + \delta_{x,-1}).$$

We calculate long-range average of the superconducting correlation, which is defined as

$$\overline{P}_{\mu,\alpha\beta} = \frac{1}{M} \sum_{2<|\boldsymbol{r}|<r_{\max}} P_{\mu,\alpha\beta}(\boldsymbol{r}),$$

where $r_{\max}$ is L $(\sqrt{2}L)$ for the two-orbital one-dimensional chain (square lattice) model and M is the number of vectors satisfying $2 < r < r_{\max}$.

6.5 Results of two-orbital Hubbard models on the one-dimensional chain

We begin with the two-orbital Hubbard model on the one-dimensional chain with $U = t, U' = J = 0$ and $\Delta = 0$, which corresponds to the trestle two-leg Hubbard ladder (see Fig. 6.3). Figure 6.8 shows the intrachain next-nearest hopping t' dependence of several physical properties at around half filling $n = 0.875$; the spin structure factor $S_{\alpha\beta}(\pi)$ and average value of superconducting correlation $\overline{P}_{\mu,\alpha\beta}$ at long distance with the d and s symmetries. We also plot the momentum distribution function at the antibonding band minimum $n_a(0)$ and that at the bonding band maximum $n_b(\pi)$, which monitor whether or not the bonding and antibonding bands intersect the Fermi level. For $0.6 \leq t'/t \leq 0.9$, as t'/t increases, $n_a(0)$ and $n_b(\pi)$, $S_{\alpha\beta}(\pi)$ slightly change, and both intrachain and interchain d-wave superconducting correlation functions $\overline{P}_{d,\alpha\beta}$ are enhanced while s-wave superconducting correlation functions $\overline{P}_{s,\alpha\beta}$ are relatively small. For $0.9 < t'/t$, as t'/t increases, $n_a(0)$ and $n_b(\pi)$ decrease rapidly but remain finite and both intra and inter chain $S_{\alpha\beta}(\pi)$ are strongly enhanced. Thus, both the bonding and antibonding bands barely intersect the Fermi level. Just before this t'/t regime, superconductivity is optimized. In the trestle two-leg ladder with large t', the interchain and diagonal pairings are enhanced (see Fig. 6.7), while in the two-leg ladder with the large interchain hopping t_{r}, only the interchain pairing is enhanced. If the site index is regarded as the orbital index, the intra and inter chain pairings correspond to the intra and inter orbital pairings, respectively. In fact, the interorbital pairing is not

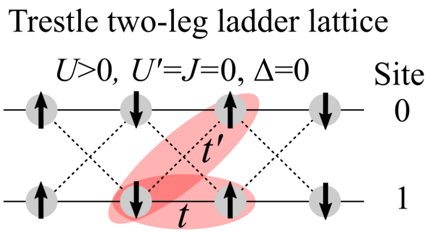

Fig. 6.7: Diagonal and interchain pairings in the trestle two-leg ladder Hubbard model ($\Delta = 0, U' = J = 0$)

common in unconventional superconductivity. For example, in some of heavy fermions, an interorbital s-wave pairing between a conduction electron and a localized f electron can be induced by an intraorbital on-site hopping [124]. Thus, the interorbital pairing can be described in the context of the inter chain and layer pairing in the two-leg ladder and bilayer square lattices.

Next we study the effect of interorbital interactions U' and J in the two-orbital Hubbard model on the one-dimensional chain with $\Delta = 0$ at around half filling. For $U = t$ and $U' = 0.8t, J = 0.1t$, t' dependence of several physical quantities is similar to those for $U = t, U' = J = 0$ as shown in Fig. 6.9. Both the intra and inter orbital pairings develop for large t'/t. The regime of enhanced superconducting correlation slightly extends to smaller t'/t as U' and J are induced (see Fig. 6.10). Further, we tried to investigate the on-site energy dependence in order to make the antibonding band incipient, but the optimization failed possibly due to the open-shell problem caused by the narrow band (see section 4.14).

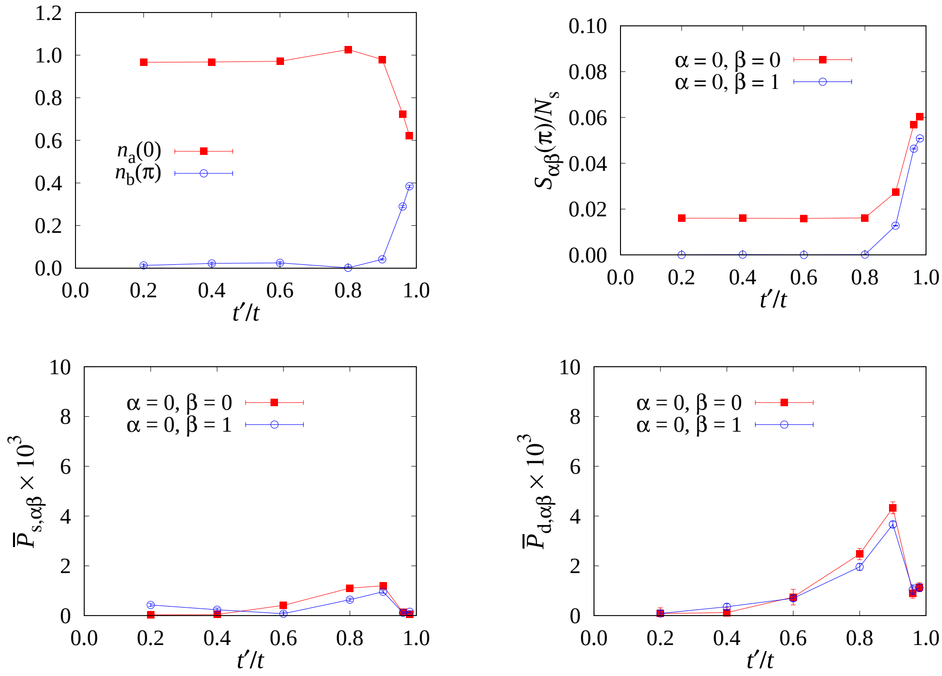

Fig. 6.8: (color online). t'/t dependences of the momentum distribution function at the narrow band minimum $n_a(0)$ and that at the narrow band maximum $n_b(\pi)$, the spin structure factor $S_{\alpha\beta}(\pi)$, the averaged s-wave superconducting correlation $\overline{P}_{\mu,\alpha\beta}$ and the averaged d-wave superconducting correlation $\overline{P}_{\mu,\alpha\beta}$ for the two-orbital one-dimensional chain system with $\Delta = 0$ and $U/t = 1, U'/t = 0, J/t = 0, n = 0.875$. The systems size is 2x48 sites and antiperiodic (AP) boundary condition is used. In the present plots and the plots in the later figures, the error bars indicate the estimated statistical errors of the Monte Carlo sampling.

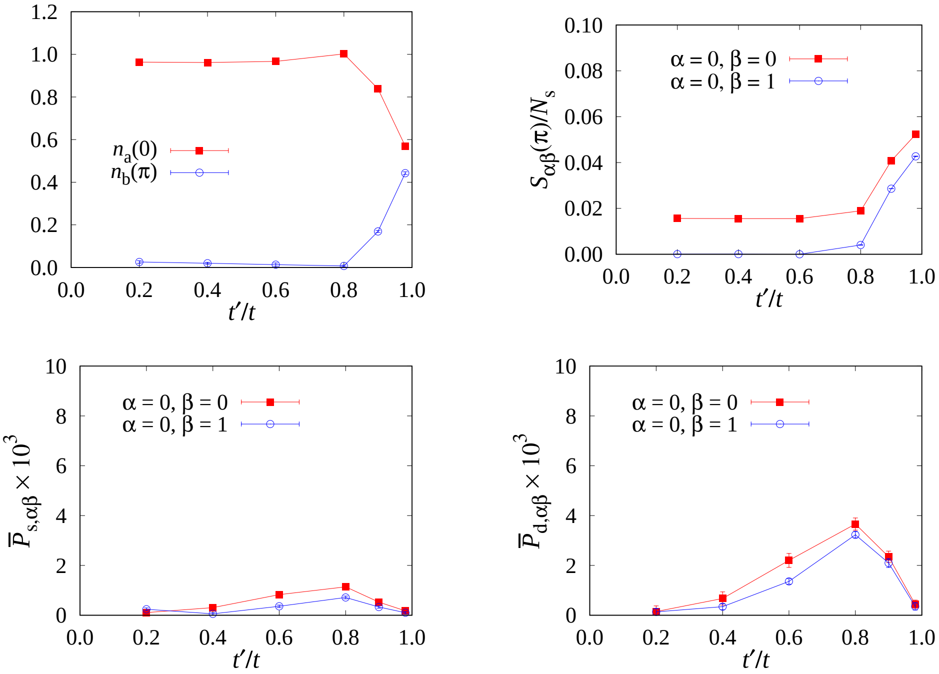

Fig. 6.9: t'/t dependences of $n_a(0)$ and $n_b(\pi)$, $S_{\alpha\beta}(\pi)$, $\overline{P}_{\mu,\alpha\beta}$ and $\overline{P}_{\mu,\alpha\beta}$ for the two-orbital one-dimensional chain system with $\Delta = 0$ and $U/t = 1, U'/t = 0.8, J/t = 0.1, n = 0.875$. The systems size is 2x48 sites and AP boundary condition is used.

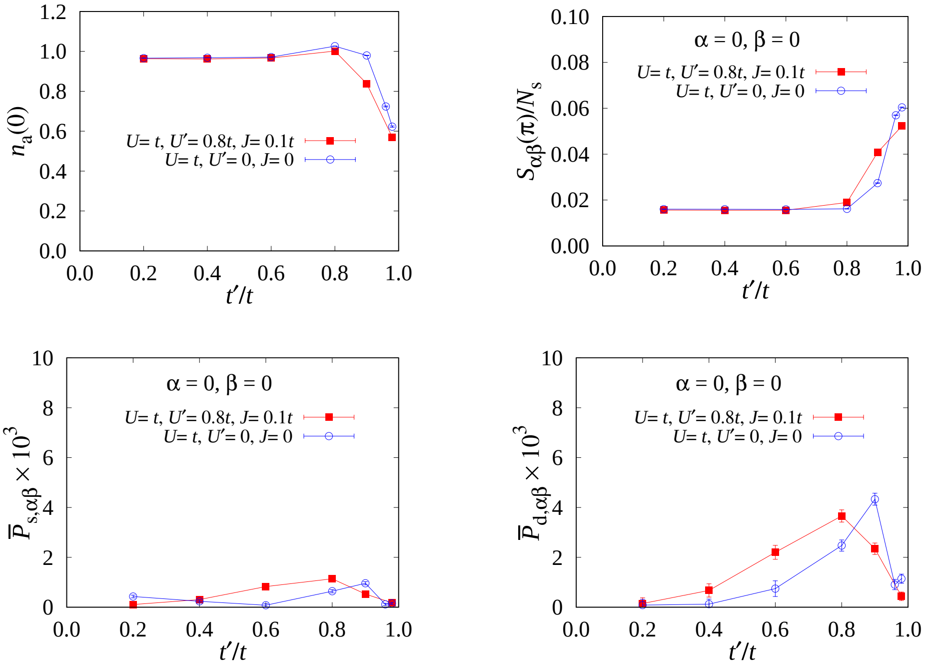

Fig. 6.10: t'/t dependences of $n_a(0)$ and $n_b(\pi)$, $S_{\alpha\beta}(\pi)$, $\overline{P}_{\mu,\alpha\beta}$ and $\overline{P}_{\mu,\alpha\beta}$ for the two-orbital one-dimensional chain system with $\Delta = 0$ and $n = 0.875$. The systems size is 2x48 sites and AP boundary condition is used.

6.6 Results of two-orbital Hubbard models on the square lattice

We next move on to the two-orbital Hubbard model on the square lattice with $U = 2t, U' = J = 0, \Delta = 0$, which corresponds to the trestle bilayer Hubbard model on the square lattice. Figure 6.11 shows the intraorbital nearest hopping t' dependence of several physical properties at around quarter filling $n \sim 0.889$; the spin structure factor $S_{\alpha\beta}(\pi)$ and average value of superconducting correlation $\overline{P}_{\mu,\alpha\beta}$ at long distance with extended s and $d_{x^2-y^2}$ symmetries. We also plot the momentum distribution function at the narrow band minimum $n_a(0)$. $n_a(0)$ does not change and intraorbital $S_{\alpha\beta}(\pi)$ decreases slightly as t'/t increases, because the DOS is finite near the Fermi level regardless of t'/t as shown in Fig. 6.4. For $t'/t \leq 0.4$, the intraorbital $d_{x^2-y^2}$-wave and extended s-wave superconducting correlations are enhanced, and the former one is larger than the latter one. Further, there are the "diamond" shaped Fermi surfaces, which can result in intraorbital $d_{x^2-y^2}$ and interorbital extended s-wave pairing For $t'/t > 0.4$, various superconducting correlations are close to each other. Thus, as in the trestle two-leg Hubbard ladder, both the intra and inter layer pairings are strongly enhanced for large t'/t, which are not seen in the bilayer Hubbard model with the strong interlayer nearest hopping. Moreover, there are the "sharp" (#) shaped Fermi surfaces (see Fig. 6.6), which can give rise to $d_{x^2-y^2}$ and extended s-wave superconducting gaps.

Further, unlike the trestle two-leg ladder lattice, the superconducting correlation functions do not rapidly change with respect to t'/t. These superconducting properties can be attributed to the shape of the DOS (see discussion). We also study the effect of interorbital interactions in the two-orbital Hubbard model on the square lattice with $\Delta = 0$ at around half filling. For $U = 2t, U' = 1.6t, J = 0.2t$ and $\Delta = 0$, t'/t dependence of several physical quantities is similar to those for $U = 2t, U' = J = 0$ at around half filling as shown in Fig. 6.12.

Next, we study on-site energy dependence of several physical properties at around quarter filling $n = 0.375$ and $t' = 0.8t, U = 2t, U' = J = 0$ as shown in Fig. 6.13. Actually, since the optimization becomes unstable for small t', we set large t'. Around $\Delta/t \sim 1$, $n_a(0,0)$ decreases rapidly and $S_{11}(\pi,\pi)$ is slowly suppressed as Δ/t increases. Thus, the incipient-band regime is estimated to be in a range of $1 \leq \Delta/t \leq 2$. Around the incipient band regime, $\overline{P}_{s^*,11}$ is maximized and favored over d-wave pairing. For $\Delta/t > 1$, $S_{00}(\pi,\pi)$ gradually increases and $\overline{P}_{d,00}$ is strongly enhanced as Δ/t increases. This is in fact reminiscent of the previous FLEX result of two-orbital systems [125–127]. Further, at around half filling $n = 0.781$ and $U = 2t, U' = J = 0$, $S_{11}(\pi)$ decreases slowly while $\overline{P}_{s^*,11}$ increases as Δ/t increases as shown in Fig. 6.14. For larger Δ/t, $n_a(0,0)$ should be suppressed by the Lifshitz transition but one faces the open-shell problem then. We also investigated the effect of intraorbital interactions in the two-orbital Hubbard model on the square lattice. For $U = 2t, U' = 1.6t, J = 0.2t$, Δ/t dependences of several physical properties are basically similar to those for $U = 2t, U' = J = 0$ as shown in Figs. 6.15 and 6.16. The regime where the superconducting correlation develops extends to lower Δ/t as interorbital interactions U', J are induced in the same as the two-orbital system

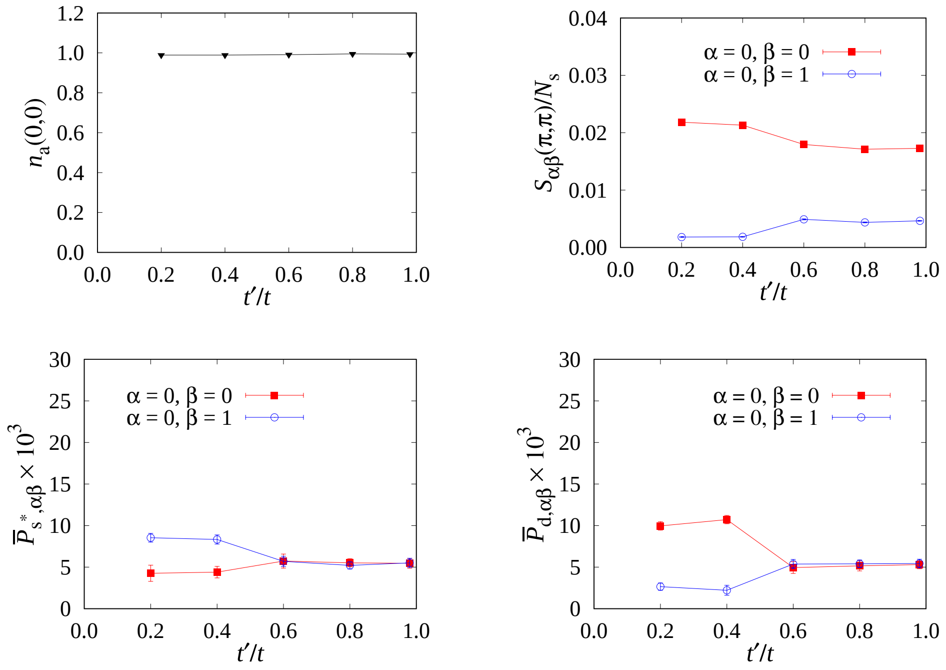

Fig. 6.11: (color online). t'/t dependences of $n_a(0,0)$ and $S_{\alpha\beta}(\pi,\pi)$, $\overline{P}_{s^*,\alpha\beta}$ and $\overline{P}_{d,\alpha\beta}$ for the two-orbital square lattice Hubbard model with $\Delta = 0$ and $U/t = 2, U'/t = 0, J/t = 0, n = 0.889$. The systems size is 6x6 sites and AP boundary condition is used.

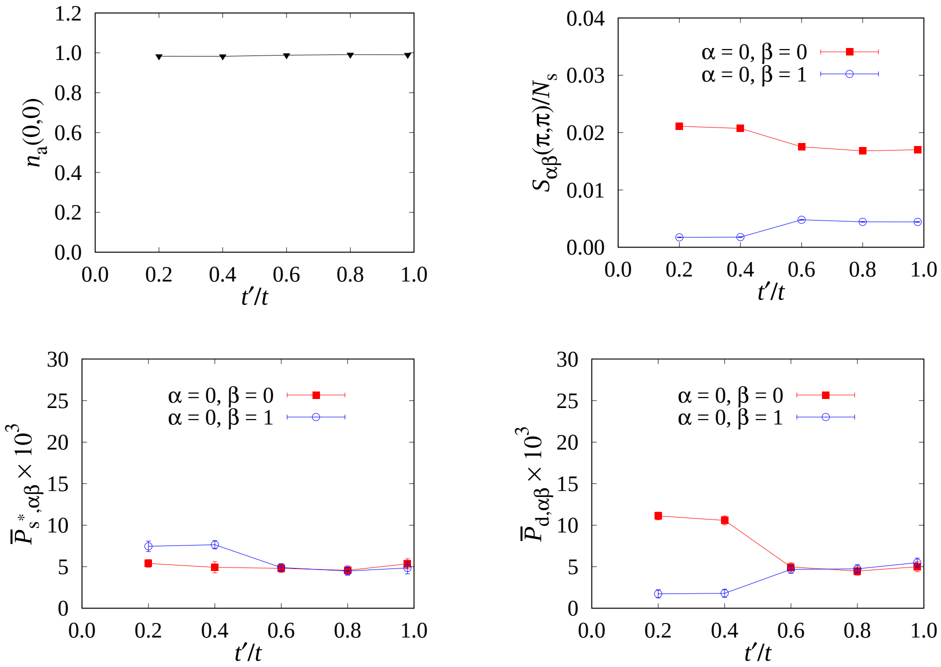

Fig. 6.12: (color online). t'/t dependences of $n_a(0,0)$ and $S_{\alpha\beta}(\pi,\pi)$, $\overline{P}_{s^*,\alpha\beta}$ and $\overline{P}_{d,\alpha\beta}$ for the two-orbital square lattice Hubbard model with $\Delta = 0$ and $U/t = 2, U'/t = 1.6, J/t = 0.2, n = 0.889$. The systems size is 6x6 sites and AP boundary condition is used.

on the one-dimensional chain. At $n = 0.781$, $n_a(0,0)$ decreases rapidly and $S_{11}(\pi,\pi)$ becomes close to zero as Δ/t increases for $4 \leq \Delta/t \leq 5$. Thus, the incipient band regime is estimated to be in a range of $4 \leq \Delta/t \leq 5$. Around the incipient band regime, $\overline{P}_{s^*,11}$ is maximized. We also verified that the parameter dependence of various physical quantities is qualitatively similar between the system with two system sizes, namely, 6x6 and 8x8 sites.In these calculations, we took relatively small U in order to circumvent the unstable optimization. Effect of stronger correlation on superconductivity in these two-orbital models is also left for future study [128].

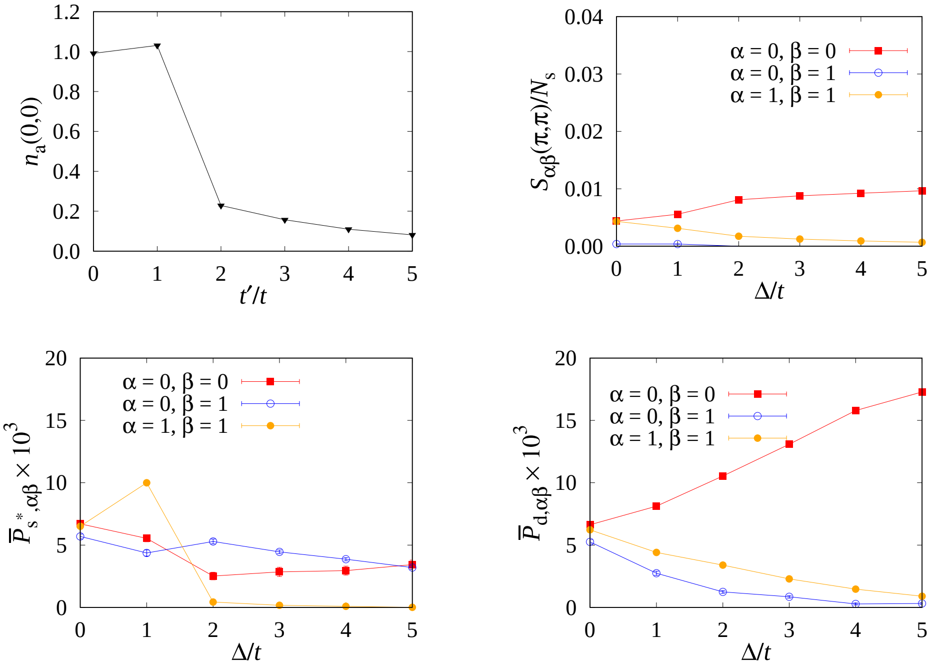

Fig. 6.13: (color online). Δ/t dependences of $n_a(0,0)$ and $S_{\alpha\beta}(\pi,\pi)$, $\overline{P}_{s^*,\alpha\beta}$ and $\overline{P}_{d,\alpha\beta}$ for the two-orbital square lattice Hubbard model with $t'/t = 0.8$ and $U/t = 2, U' = J = 0, n = 0.375$. The systems size is 8x8 sites and AP condition is used.

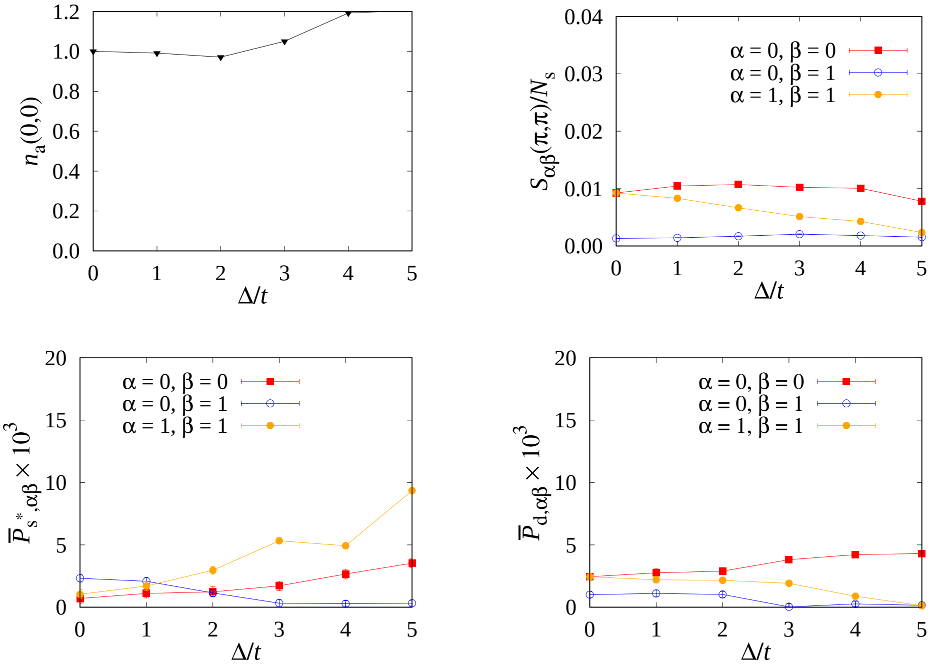

Fig. 6.14: (color online). Δ/t dependences of $n_a(0,0)$ and $S_{\alpha\beta}(\pi,\pi)$, $\overline{P}_{s^*,\alpha\beta}$ and $\overline{P}_{d,\alpha\beta}$ for the two-orbital square lattice Hubbard model with $t'/t = 0.8$ and $U/t = 2, U' = J = 0, n = 0.781$. The systems size is 8x8 sites and AP condition is used.

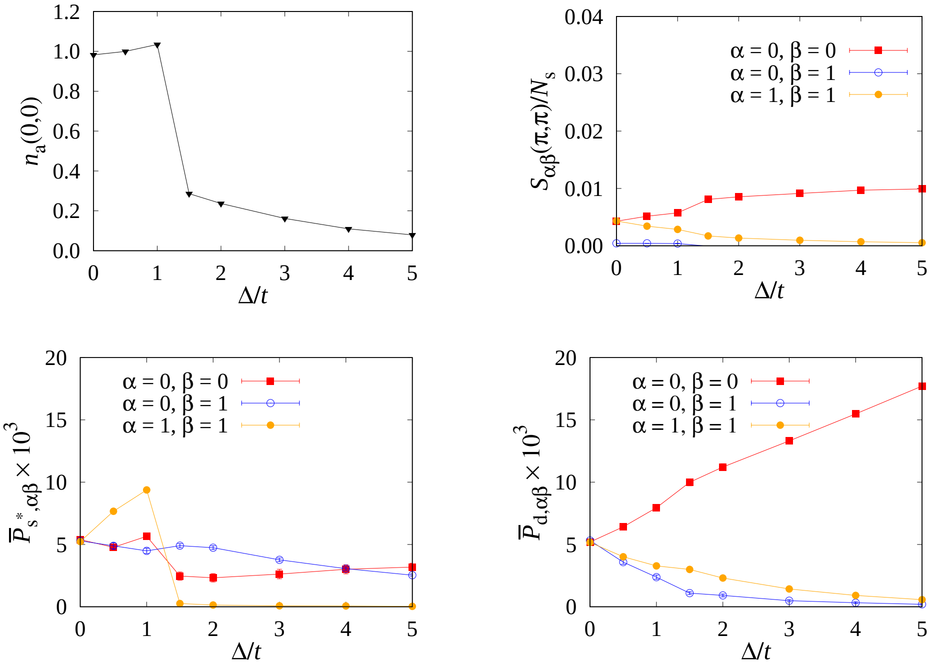

Fig. 6.15: (color online). Δ/t dependences of $n_a(0,0)$ and $S_{\alpha\beta}(\pi,\pi)$, $\overline{P}_{s^*,\alpha\beta}$ and $\overline{P}_{d,\alpha\beta}$ for the two-orbital square lattice Hubbard model with $t'/t = 0.8$ and $U/t = 2, U'/t = 1.6, J/t = 0.2, n = 0.375$. The systems size is 8x8 sites and AP condition is used.

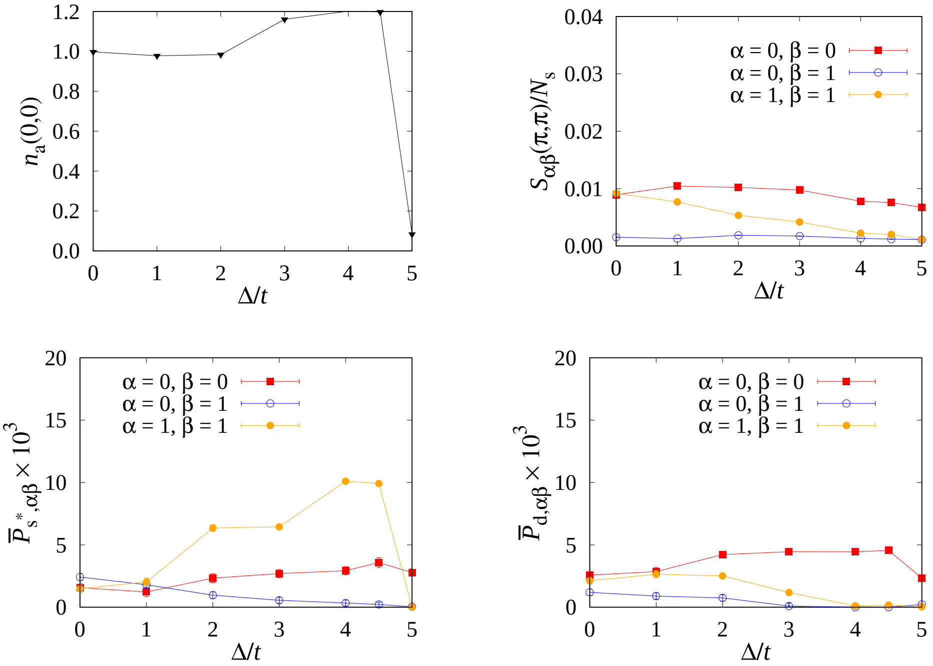

Fig. 6.16: (color online). Δ/t dependences of $n_a(0,0)$ and $S_{\alpha\beta}(\pi,\pi)$, $\overline{P}_{s^*,\alpha\beta}$ and $\overline{P}_{d,\alpha\beta}$ for the two-orbital square lattice Hubbard model with $t'/t = 0.8$ and $U/t = 2, U'/t = 1.6, J/t = 0.2, n = 0.781$. The systems size is 8x8 sites and AP condition is used.

6.7 Discussion

In this section, we will try to interpret the mVMC results for the two-orbital models from the viewpoint of the relation between spin fluctuation and the density of states, as in the case of the bilayer and two-leg Hubbard models discussed in section 3 [68]. In the two-orbital one-dimensional chain, the superconducting correlation is strongly enhanced for large $t'/t(\sim 0.8)$ when the edge of the narrow band is apart from, but close to the Fermi level, while such an enhancement is not observed for the two-orbital square lattice. These differences can be attributed to the shape of the DOS. In the two-orbital one-dimensional chain, the diverging DOS at the band edge approaches the Fermi level as t'/t increases, and when the diverging DOS is within a certain energy range, the finite energy spin fluctuations effective for pairing develops (see Fig. 6.3). When t'/t becomes too large, the diverging DOS comes too close to the Fermi level, resulting in a strong development of low-lying, pair-breaking, spin fluctuations and the suppression of superconductivity. This is a possible reason why superconductivity is optimized for large t'/t where the spin correlation is small in the two-orbital two-leg ladder. If the narrow band becomes incipient as Δ increases, superconductivity can be enhanced. The confirmation of this possibility is left for future study. By contrast, in the two-orbital square lattice, the diverging DOS is transferred to higher energies from the center of the band as t' increases as shown in Fig. 6.4. For small t'/t the diverging DOS is concentrated in the regime where it can contribute to the finite-energy spin fluctuations effective for pairing. On the other hand, for large t'/t, the DOS near the Fermi level is small, giving rise to relatively small superconducting correlations.

Further, we also discuss the relation between the two-orbital square lattice model and the bilayer square lattice model. We studied the on-site energy Δ dependence of various physical quantities in the two-orbital square lattice with the strong hybridization $t' = 0.8t$, where the DOS is diverging near the band edge as shown in 6.4. As Δ increases, the band bottom of the antibonding band approaches the Fermi level, and eventually, the antibonding band loses its Fermi surface. The nesting between electron and hole Fermi surfaces having orbital 1 weight, combined with the intraorbital Coulomb repulsion U, induces interband spin fluctuations, which result in the intraorbital extended s-wave Cooper pairs of electrons in orbital 1 [17, 121–123]. When the edge of the antibonding band is incipient, the intraorbital extended s-wave pairing is enhanced as in the bilayer Hubbard model. Thus, the hybridization effect is crucial to induce superconductivity in the present two-orbital systems on the square lattice, since it produces the different Fermi surfaces originating from the same orbital . We note that this enhancement of superconductivity is primarily caused by the intraorbital Hubbard U. By comparison with results for the case with/without interorbital interactions, we find that the interorbital interactions can make the bands narrower but they do not strongly affect the strength of the pairing. At around half filling, the antibonding band becomes incipient for larger Δ than the case at around quarter filling. For large band filling n, larger Δ is required to realize the incipient antibonding band because the Fermi level moves away from the antibonding band minimum when n increases. At around quarter filling, for sufficient large

Δ, where the two-orbital system can be approximated as the single orbital system on the square lattice, $\overline{P}_{s^*,11}$ is suppressed, and $\overline{P}_{d,00}$ is strongly enhanced, which is because the filling of orbital 0 becomes close to optimal filling for d-wave superconductivity.

Therefore, in the present study, we showed that in the two-orbital system on the square lattice with strong hybridization, the hybridization effect gives rise to the nesting between proportions of the Fermi surfaces with common orbital weights, which induces interband pair scattering. On the other hand, a FLEX study [120] reported that in the two-orbital Hubbard model with medium hybridization, the $s^{\pm}$ wave pairing is enhanced. There it has been argued that a "orbital site transformation" provides insight on the possible pairing mechanism.

Let us consider a special case with $U = U' = J \equiv U_0/2$, where the two-orbital model is transfered to the two-leg ladder or bilayer Hubbard models by using the following transformation [120]

$$\begin{cases} a^{\dagger}_{i0\sigma} = \dfrac{1}{\sqrt{2}}(c^{\dagger}_{i0\sigma} + c^{\dagger}_{i1\sigma}) \\ a^{\dagger}_{i1\sigma} = \dfrac{1}{\sqrt{2}}(-c^{\dagger}_{i0\sigma} + c^{\dagger}_{i1\sigma}) \end{cases}, \tag{6.7.1}$$

where $a^{\dagger}_{im\sigma}, a_{im\sigma}$ creates/annihilates a fermion with spin $\sigma(=\uparrow,\downarrow)$ and $m^{\text{th}}(=0,1)$ chain or layer. We call this the "orbital site transformation". Using Eq. 6.7.1, the interaction terms are rewritten as

$$\begin{aligned} &\frac{U_0}{2}\sum_{i,\alpha} n_{i\alpha\uparrow}n_{i\alpha\downarrow} + \frac{U_0}{2}\sum_{i,\alpha<\beta,\sigma} n_{i\alpha\sigma}n_{i\beta\bar{\sigma}}, \\ &+ \frac{U_0}{2}\sum_{i,\alpha<\beta}(c^{\dagger}_{i\alpha\uparrow}c^{\dagger}_{i\beta\downarrow}c_{i\alpha\downarrow}c_{i\beta\uparrow} + c^{\dagger}_{i\alpha\uparrow}c^{\dagger}_{i\alpha\downarrow}c_{i\beta\downarrow}c_{i\beta\uparrow} + \text{H.c.}) = U_0\sum_{i,m} n_{im\uparrow}n_{im\downarrow}, \end{aligned} \tag{6.7.2}$$

where $n_{im\sigma} = a^{\dagger}_{im\sigma}a_{im\sigma}$. This interaction term breaks spin and orbital rotational symmetries, namely, $U' = U - 2J$. The large Hund coupling J cancels out the effect of the intraorbital Coulomb repulsion U', resulting in the spin fluctuation. The kinetic term is

$$\begin{aligned} &\sum_{\boldsymbol{k},\alpha,\beta,\sigma} \varepsilon_{\alpha\beta}(\boldsymbol{k})c^{\dagger}_{\boldsymbol{k}\alpha\sigma}c_{\boldsymbol{k}\beta\sigma} \\ &= \sum_{\boldsymbol{k},\sigma}(a^{\dagger}_{\boldsymbol{k}0\sigma}, a^{\dagger}_{\boldsymbol{k}1\sigma}) \begin{pmatrix} \varepsilon_{\boldsymbol{k}} + \varepsilon'_{\boldsymbol{k}} & -\Delta \\ -\Delta & \varepsilon_{\boldsymbol{k}} - \varepsilon'_{\boldsymbol{k}} \end{pmatrix} \begin{pmatrix} a_{\boldsymbol{k}0\sigma} \\ a_{\boldsymbol{k}1\sigma} \end{pmatrix} && (6.7.3) \\ &\equiv \sum_{\boldsymbol{k},m,n,\sigma} \tilde{\varepsilon}_{mn}(\boldsymbol{k})a^{\dagger}_{\boldsymbol{k}m\sigma}a_{\boldsymbol{k}n\sigma}, && (6.7.4) \end{aligned}$$

where the constant term is omitted in the second equality. Therefore, for $\varepsilon'_{\boldsymbol{k}} = 0$, this two-orbital Hubbard model with specific interorbital interactions is equivalent to the bilayer and two-leg ladder Hubbard models, where $s^{\pm}$ pairing can be induced. Also in the present two-orbital model, as t' decreases, the $s^{\pm}$ pairing can be dominant.

The above observation suggests a possible new pairing mechanism in the moderate hybridization regime of the two-orbital model, where not only the intraorbital but also interorbital interactions play important roles. Since we have studied the bilayer Hubbard model using mVMC in this thesis, it is an interesting future study to pursue this possibility using mVMC.

6.8 Summary

To summarize, we have studied superconductivity in the two-orbital Hubbard model on the one-dimensional chain and square lattices. In both systems, we found the intra and inter orbital pairings with various symmetries, which can correspond to intra/inter chain and layer pairings in trestle two-leg ladder and bilayer square lattice systems. On the other hand, in the two-orbital Hubbard model on the square lattice, we also studied on-site energy Δ dependence of various quantities for near half and quarter fillings. For large Δ, extended s-wave superconductivity can be optimized in a region around the Lifshitz transition point, where one of the bands mainly originating from an orbital with higher energy is (nearly) incipient. For small Δ, both the intra/inter orbital and d (extended s/d)-wave pairings are enhanced for the two-orbital Hubbard model on the one-dimensional chain (square lattice) lattice. Further, at around quarter filling, d-wave superconductivity can be optimized for large Δ. The above results are reminiscent of previous FLEX studies. This nontrivial resemblance shows that the spin-fluctuation spectrum plays an important role regardless of the multiplicity of orbital of systems.

7 Concluding remarks

Motivated by previous studies on the two-leg ladder, bilayer, and two-orbital Hubbard models, which adopted FLEX, we have systematically investigated unconventional superconductivity in two-band systems using mVMC. The mVMC is alternative and supplmentary approach to weak coupling theories, which can describe strong correlation effects and order competitions accurately.

Implement and performance of the mVMC method

The VMC method does not have the negative sign problem unlike the auxiliary field quantum Monte-Carlo method, so that it can be applied to study relatively large system sizes even at large amplitude of electron interactions and geometrical frustration at reasonable computational cost. However, the result can be biased strongly depending on the form and initial value of variational wave functions. In the conventional VMC method, the number of variational parameters is several dozen. On the other hand, in the mVMC method, one can employ thousands of variational parameters, which enables us to describe various quantum fluctuations of order parameters and strong correlation effects accurately. However, the mVMC method is difficult to handle. I implemented the mVMC method by myself referring a previous work. Further, I mastered the method and performed the mVMC calculations successfully. Later, we transfered from my own program to an open software because it has the convenient flexible interface. We performed all calculations in this thesis by using the open software. The initial values of the variational wave functions are obtained from my own program.

Two-leg ladder and bilayer Hubbard models with an incipient band

We studied superconductivity in the Hubbard model on the two-leg ladder and bilayer square lattices. In both systems, superconductivity can be optimized in a region around the Lifshitz transition point, where one of bands is (nearly) incipient. The parameter dependence of the superconducting correlation function is reminiscent of the previous FLEX results. What is noteworthy is the important role played by an incipient band in the occurrence of superconductivity in the strong coupling regime. The present result suggests that the following view holds not only in the weak coupling regime but also in the strong coupling regime as well: superconductivity is enhanced by an incipient band due to the suppression of the near-zero-energy spin fluctuations and enhanced finite energy spin fluctuations working as an effective pairing glue. We also stress that the resemblance between these two approaches is nontrivial; FLEX takes into account the spin fluctuations (in momentum space) explicitly in the effective interaction, whereas the present mVMC method incorporates the electron correlation effect in a real-space-based manner, which is expected to be more appropriate in the strong coupling regime.Since it has been shown that incipient bands enhance superconductivity in other models, it is an intriguing future problem to study those models using the mVMC method.

Two-orbital Hubbard models on the one-dimensional and square lattices

The study on the two-leg ladder and bilayer Hubbard models was partially motivated by recent studies on the iron-based superconductors with incipient bands. The bilayer Hubbard model can be regarded as a single-orbital analogue of the iron-based superconductors. Thus, we have studied superconductivity in the two-orbital Hubbard model on the one-dimensional chain and square lattices. In both systems, we found the intra and inter orbital pairings with various symmetries, which can be regarded as intra/inter chain (layer) pairings in the trestle two-leg ladder (bilayer square) lattice. Further, in the two-orbital Hubbard model on the square lattice, superconductivity can be enhanced by the incipient band as in the bilayer Hubbard model. Also, near quarter filling, d-wave superconductivity can be enhanced as the energy difference between two orbitals increases. The above results are also reminiscent of previous FLEX studies of a unique type of cuprates and iron-based superconductors. We once again stress that the resemblance between these two approaches is a non-trivial problem. The above results showed that the spin-fluctuation spectrum plays an important role in the occurrence of unconventional superconductivity regardless of the multiplicity of orbital of systems.

We also discussed a possible new pairing mechanism where not only the intraorbital but also interorbital interactions play important roles. It is an interesting future study to pursue this possibility using mVMC. We have carried out these mVMC calculations on the two-orbital models for relatively small U, where the difficulty of the optimization is reduced. Effect of stronger correlation on superconductivity in these two-orbital models is also left for future study.

Bibliography

[1] A. Schilling, M. Cantoni, J. Guo, H. Ott, Superconductivity above 130 K in the Hg-Ba-Ca-Cu-O system, Nature **363**, 56 (1993).

[2] D. Ogura, Springer Theses: Theoretical Study of Electron Correlation Driven Superconductivity in Systems with Coexisting Wide and Narrow Bands, Springer, 2019.

[3] J. Bardeen, L. N. Cooper, J. R. Schrieffer, Theory of Superconductivity, Phys. Rev. **108**, 1175 (1957).

[4] W. L. McMillan, Transition Temperature of Strong-Coupled Superconductors, Phys. Rev. **167**, 331 (1968).

[5] A. P. Drozdov, M. I. Eremets, I. A. Troyan, V. Ksenofontov, S. I. Shylin, Conventional superconductivity at 203 kelvin at high pressures in the sulfur hydride system, Nature **525**, 73 (2015).

[6] A. P. Drozdov, P. P. Kong, V. S. Minkov, S. P. Besedin, M. A. Kuzovnikov, S. Mozaffari, L. Balicas, F. F. Balakirev, D. E. Graf, V. B. Prakapenka, E. Greenberg, D. A. Knyazev, M. Tkacz, M. I. Eremets, Superconductivity at 250 K in lanthanum hydride under high pressures, Nature **569**, 528 (2019).

[7] M. Somayazulu, M. Ahart, A. K. Mishra, Z. M. Geballe, M. Baldini, Y. Meng, V. V. Struzhkin, R. J. Hemley, Evidence for Superconductivity above 260 K in Lanthanum Superhydride at Megabar Pressures, Phys. Rev. Lett. **122**, 027001 (2019).

[8] N. W. Ashcroft, Hydrogen Dominant Metallic Alloys: High Temperature Superconductors?, Phys. Rev. Lett. **92**, 187002 (2004).

[9] Y. Wang, Y. Ma, Perspective: Crystal structure prediction at high pressure, J. Chem. Phys. **140**, 040901 (2014).

[10] Y. Li, J. Han, Y. Li, Y. Ma, The metallization and superconductivity of dense hydrogen sulfide, J. Chem. Phys. **140**, 174712 (2014).

[11] J. G. Bednorz, K. A. Muller, Possible high Tc superconductivity in the Ba-La-Cu-O system, Z. Phys. B **64**, 189 (1986).

[12] Y. Kamihara, T. Watanabe, M. Hirano, H. Hosono, Iron-Based Layered Superconductor La[O1-xFx]FeAs (x = 0.05-0.12) with Tc = 26 K, Journal of the American Chemical Society **130**, 3296 (2008).

[13] T. Moriya, K. Ueda, Spin fluctuations and high temperature superconductivity, Adv. Phys. **49**, 555 (2000).

[14] P. A. Lee, N. Nagaosa, X. G. Wen, Doping a Mott insulator: Physics of high-temperature superconductivity, Rev. Mod. Phys. **78**, 16 (2006).

[15] D. N. Basov, A. V. Chubukov, Manifesto for a higher Tc, Nature Physics **7**, 272 (2011).

[16] K. Momma, F. Izumi, VESTA 3 for three-dimensional visualization of crystal, volumetric and morphology data, Journal of Applied Crystallography **44**, 1272 (2011).

[17] K. Kuroki, S. Onari, R. Arita, H. Usui, Y. Tanaka, H. Kontani, H. Aoki, Unconventional pairing originating from the disconnected Fermi surfaces of superconducting $\mathrm{LaFeAsO}_{1-x}\mathrm{F}_x$, Phys. Rev. Lett. **101**, 087004 (2008).

[18] P. J. Hirschfeld, M. M. Korshunov, I. I. Mazin, Gap symmetry and structure of Fe-based superconductors, Reports on Progress in Physics **74**, 124508 (2011).

[19] K. Kuroki, in Iron-based Superconductors: Materials, Properties and Mechanisms Chapter 8, Pan Stanford Publishing, 2013.

[20] A. Chubukov, P. J. Hirschfeld, Iron-based superconductors, seven years later, Phys. Today **68(6)**, 46 (2015).

[21] H. Hosono, K. Kuroki, Iron-based superconductors: Current status of materials and pairing mechanism, Physica C **514**, 399 (2015).

[22] I. I. Mazin, D. J. Singh, M. D. Johannes, M. H. Du, Unconventional superconductivity with a sign reversal in the order parameter of $\mathrm{LaFeAsO}_{1-x}\mathrm{F}_x$, Phys. Rev. Lett. **101**, 057003 (2008).

[23] J. Guo, S. Jin, G. Wang, S. Wang, K. Zhu, T. Zhou, M. He, X. Chen, Superconductivity in the iron selenide $\mathrm{K}_x\mathrm{Fe}_2\mathrm{Se}_2$ ($0 \leq x \leq 1.0$), Phys. Rev. B **82**, 180520(R) (2010).

[24] T. Qian, X.-P. Wang, W.-C. Jin, P. Zhang, P. Richard, G. Xu, X. Dai, Z. Fang, J.-G. Guo, X.-L. Chen, et al., Absence of a holelike Fermi surface for the iron-based $\mathrm{K}_{0.8}\mathrm{Fe}_{1.7}\mathrm{Se}_2$ superconductor revealed by angle-resolved photoemission spectroscopy, Phys. Rev. Lett. **106**, 187001 (2011).

[25] Q.-Y. Wang, Z. Li, W.-H. Zhang, Z.-C. Zhang, J.-S. Zhang, W. Li, H. Ding, Y.-B. Ou, P. Deng, K. Chang, et al., Interface-induced high-temperature superconductivity in single unit-cell FeSe films on $SrTiO_3$, Chinese Physics Letters **29**, 037402 (2012).

[26] S. Tan, Y. Zhang, M. Xia, Z. Ye, F. Chen, X. Xie, R. Peng, D. Xu, Q. Fan, H. Xu, et al., Interface-induced superconductivity and strain-dependent spin density waves in FeSe/$SrTiO_3$ thin films, Nature materials **12**, 634 (2013).

[27] D. Liu, W. Zhang, D. Mou, J. He, Y.-B. Ou, Q.-Y. Wang, Z. Li, L. Wang, L. Zhao, S. He, et al., Electronic origin of high-temperature superconductivity in single-layer FeSe superconductor, Nat. Comm. **3**, 931 (2012).

[28] S. He, J. He, W. Zhang, L. Zhao, D. Liu, X. Liu, D. Mou, Y.-B. Ou, Q.-Y. Wang, Z. Li, et al., Phase diagram and electronic indication of high-temperature superconductivity at 65 K in single-layer FeSe films, Nature Materials **12**, 605 (2013).

[29] J. J. Lee, F. T. Schmitt, R. G. Moore, S. Johnston, Y.-T. Cui, W. Li, M. Yi, Z. K. Liu, M. Hashimoto, Y. Zhang, et al., Interfacial mode coupling as the origin of the enhancement of T_c in FeSe films on $SrTiO_3$, Nature **515**, 245 (2014).

[30] S. Iimura, S. Matsuishi, H. Sato, T. Hanna, Y. Muraba, S. W. Kim, J. E. Kim, M. Takata, H. Hosono, Two-dome structure in electron-doped iron arsenide superconductors, Nat. Comm. **3**, 943 (2012).

[31] H. Miao, T. Qian, X. Shi, P. Richard, T. Kim, M. Hoesch, L. Xing, X.-C. Wang, C.-Q. Jin, J.-P. Hu, et al., Observation of strong electron pairing on bands without Fermi surfaces in $LiFe_{1-x}Co_xAs$, Nat. Comm. **6**, 6056 (2015).

[32] X. H. Niu, R. Peng, H. C. Xu, Y. J. Yan, J. Jiang, D. F. Xu, T. L. Yu, Q. Song, Z. C. Huang, Y. X. Wang, et al., Surface electronic structure and isotropic superconducting gap in $(Li_{0.8}Fe_{0.2})OHFeSe$, Phys. Rev. B **92**, 060504(R) (2015).

[33] A. Charnukha, D. V. Evtushinsky, C. E. Matt, N. Xu, M. Shi, B. Büchner, N. D. Zhigadlo, B. Batlogg, S. V. Borisenko, High-temperature superconductivity from fine-tuning of Fermi-surface singularities in iron oxypnictides, Sci. Rep. **5**, 18273 (2015).

[34] Y. Miyata, K. Nakayama, K. Sugawara, T. Sato, T. Takahashi, High-temperature superconductivity in potassium-coated multilayer FeSe thin films, Nat. Materials **14**, 775 (2015).

[35] F. Wang, F. Yang, M. Gao, Z.-Y. Lu, T. Xiang, D.-H. Lee, The electron pairing of $K_xFe_{2-y}Se_2$, Europhysics Letters **93**, 57003 (2011).

[36] Y. Bang, A shadow gap in the over-doped $(Ba_{1-x}K_x)Fe_2As_2$ compound, New J. Phys. **16**, 023029 (2014).

[37] X. Chen, S. Maiti, A. Linscheid, P. J. Hirschfeld, Electron pairing in the presence of incipient bands in iron-based superconductors, Phys. Rev. B **92**, 224514 (2015).

[38] A. Linscheid, S. Maiti, Y. Wang, S. Johnston, P. J. Hirschfeld, High T_c via spin fluctuations from incipient bands: Application to monolayers and intercalates of FeSe, Phys. Rev. Lett. **117**, 077003 (2016).

[39] Y. Bang, Pairing mechanism of heavily electron doped FeSe systems: dynamical tuning of the pairing cutoff energy, New J. Phys. **18**, 113054 (2016).

[40] Y. Bang, Phonon boost effect on the $s^{\pm}$-wave superconductor with incipient band, Sci. Reports **9**, 3907 (2019).

[41] M. Sigrist, K. Ueda, Phenomenological theory of unconventional superconductivity, Rev. Mod. Phys. **63**, 239 (1991).

[42] L. F. Mattheiss, Electronic band properties and superconductivity in $\mathrm{La}_{2-y}\mathrm{X}_y\mathrm{CuO}_4$, Phys. Rev. Lett. **58**, 1028 (1987).

[43] M. S. Hybertsen, M. Schlüter, N. E. Christensen, Calculation of coulomb-interaction parameters for $\mathrm{La_2CuO_4}$ using a constrained-density-functional approach, Phys. Rev. B **39**, 1989 (9028).

[44] M. Imada, T. Miyake, Electronic Structure Calculation by First Principles for Strongly Correlated Electron Systems, J. Phys. Soc. Jpn. **79**, 112001 (2010).

[45] N. E. Bickers, D. J. Scalapino, S. R. White, Conserving Approximations for Strongly Correlated Electron Systems: Bethe-Salpeter Equation and Dynamics for the Two-Dimensional Hubbard Model, Phys. Rev. Lett. **62**, 961 (1989).

[46] T. Dahm, L. Tewordt, Quasiparticle and Spin Excitation Spectra in the Normal and d-Wave Superconducting State of the Two-Dimensional Hubbard Model, Phys. Rev. Lett. **74**, 793 (1995).

[47] N. Bulut, D. J. Scalapino, R. T. Scalettar, Nodeless d-wave pairing in a two-layer Hubbard model, Phys. Rev. B **45**, 5577 (1992).

[48] R. T. Scalettar, J. W. Cannon, D. J. Scalapino, R. L. Sugar, Magnetic and pairing correlations in coupled Hubbard planes, Phys. Rev. B **50**, 13419 (1994).

[49] R. E. Hetzel, W. von der Linden, W. Hanke, Pairing correlations in a two-layer Hubbard model, Phys. Rev. B **50**, 4159 (1994).

[50] R. R. dos Santos, Magnetism and pairing in Hubbard bilayers, Phys. Rev. B **51**, 15540 (1995).

[51] A. I. Liechtenstein, I. I. Mazin, O.K.Andersen, s-wave superconductivity from an antiferromagnetic spin-fluctuation model for bilayer materials, Phys. Rev. Lett. **74**, 2303 (1995).

[52] K. Kuroki, T. Kimura, R. Arita, High-temperature superconductivity in dimer array systems, Phys. Rev. B **66**, 184508 (2002).

[53] S. S. Kancharla, S. Okamoto, Band insulator to Mott insulator transition in a bilayer Hubbard model, Phys. Rev. B **75**, 193103 (2007).

[54] K. Bouadim, G. G. Batrouni, F. Hebert, R. T. Scalettar, Band insulator to Mott insulator transition in a bilayer Hubbard model, Phys. Rev. B **77**, 144527 (2008).

[55] N. Lanata, P. Barone, M. Fabrizio, Superconductivity in the doped bilayer Hubbard model, Phys. Rev. B **80**, 224524 (2009).

[56] H. Zhai, F. Wang, D.-H. Lee, Antiferromagnetically driven electronic correlations in iron pnictides and cuprates, Phys. Rev. B **80**, 064517 (2009).

[57] T. A. Maier, D. J. Scalapino, Pair structure and the pairing interaction in a bilayer Hubbard model, Phys. Rev. B **84**, 180513(R) (2011).

[58] V. Mishra, D. J. Scalapino, T. Maier, $s_\pm$ pairing near a Lifshitz transition, Sci. Rep. **6**, 32078 (2016).

[59] M. Nakata, D. Ogura, H. Usui, K. Kuroki, Finite-energy spin fluctuations as a pairing glue in systems with coexisting electron and hole bands, Phys. Rev. B **95**, 214509 (2017).

[60] T. A. Maier, V. Mishra, G. Balduzzi, D. J. Scalapino, Effective pairing interaction in a system with an incipient band, Phys. Rev. B **99**, 140504(R) (2019).

[61] K. Kuroki, T. Higashida, R. Arita, High-T_c superconductivity due to coexisting wide and narrow bands: A fluctuation exchange study of the Hubbard ladder as a test case, Phys. Rev. B **72**, 212509 (2005).

[62] K. Matsumoto, D. Ogura, K. Kuroki, Wide applicability of high-T_c pairing originating from coexisting wide and incipient narrow bands in quasi-one-dimensional systems, Phys. Rev. B **97**, 014516 (2018).

[63] K. Kobayashi, M. Okumura, S. Yamada, M. Machida, H. Aoki, Superconductivity in repulsively interacting fermions on a diamond chain: Flat-band-induced pairing, Phys. Rev. B **94**, 214501 (2016).

[64] T. Misumi, H. Aoki, New class of flat-band models on tetragonal and hexagonal lattices: Gapped versus crossing flat bands, Phys. Rev. B **96**, 155137 (2017).

[65] D. Ogura, H. Aoki, K. Kuroki, Possible high-T_c superconductivity due to incipient narrow bands originating from hidden ladders in Ruddlesden-Popper compounds, Phys. Rev. B **96**, 184513 (2017).

[66] S. Sayyad, E. Huang, M. Kitatani, M.-S. Vaezi, Z. Nussinov, A. Vaezi, H. Aoki, Pairing and non-Fermi liquid behavior in partially flat-band systems, arXiv:1903.09888v3 (2019).

[67] H. Aoki, Theoretical possibilities for flat-band superconductivity, arXiv:1912.04469v1 (2019).

[68] K. Matsumoto, D. Ogura, K. Kuroki, Strongly enhanced superconductivity due to finite energy spin flucutations induced by an incipient band : a FLEX study on the bilayer Hubbard model with vertical and diagonal interlayer hoppings, arXiv:1912.11331v1 (2019).

[69] A. J. Millis, S. Sachdev, C. M. Varma, Inelastic scattering and pair breaking in anisotropic and isotropic superconductors, Phys. Rev. B **37**, 4975 (1988).

[70] D. Tahara, M. Imada, Variational Monte Carlo method combined with quantum-number projection and multi-variable optimization, J. Phys. Soc. Jpn. **77**, 114701 (2008).

[71] T. Misawa, S. Motira, K. Yoshimi, M. Kawamura, Y. Motoyama, K. Ido, T. Ohgoe, M. Imada, T. Kato, mVMC-open-source software for many-variable variational Monte Carlo method, Computer Physics Communications **235**, 447 (2019).

[72] D. Ceperley, G. V. Chester, M. H. Kalos, Monte Carlo simulation of a many-fermion study, Phys. Rev. B **16**, 3081 (1977).

[73] S. Sorella, Generalized lanczos algorithm for variational quantum Monte Carlo, Phys. Rev. B **64**, 024512 (2001).

[74] S. Sorella, Wave function optimization in the variational Monte Carlo method, Phys. Rev. B **71**, 241103(R) (2005).

[75] C. J. Umrigar, J. Toulouse, C. Filippi, S. Sorella, R. G. Hennig, Alleviation of the Fermion-Sign Problem by Optimization of Many-Body Wave Functions, Phys. Rev. Lett. **98**, 110201 (2007).

[76] M. Capello, F. Becca, M. Fabrizio, S. Sorella, E. Tosatti, Variational Description of Mott Insulators, Phys. Rev. Lett. **94**, 026406 (2005).

[77] M. Takahiro, I. Masatoshi, Origin of high-T_c superconductivity in doped hubbard models and their extensions: Roles of uniform charge fluctuations, Phys. Rev. B **90**, 115137 (2014).

[78] K. Ido, T. Ohgoe, M. Imada, Competition among various charge-inhomogeneous states and d-wave superconducting state in Hubbard models on square lattices, Phys. Rev. B **97**, 045138 (2018).

[79] T. Misawa, K. Nakamura, M. Imada, Ab *initio* evidence for strong correlation associated with Mott proximity in iron-based superconductors, Phys. Rev. Lett. **108**, 177007 (2012).

[80] T. Misawa, M. Imada, Superconductivity and its mechanism in an ab *initio* model for electron-doped LaFeAsO, Nature Commn. **5**, 5738 (2014).

[81] A. S. Darmawan, Y. Nomura, Y. Yamaji, M. Imada, Stripe and superconducting order competing in the Hubbard model on a square lattice studied by a combined variational Monte Carlo and tensor network method, Phys. Rev. B **98**, 205132 (2018).

[82] M. Hirayama, Y. Yamaji, T. Misawa, M. Imada, Ab *initio* effective Hamiltonians for cuprate superconductors, Phys. Rev. B **98**, 134501 (2018).

[83] T. Ohgoe, M. Hirayama, T. Misawa, K. Ido, Y. Yamaji, M. Imada, Ab *Initio* Study on Superconductivity and Inhomogeneity in Hg-based Cuprate Superconductor, arXiv:1902.00122v2 (2019).

[84] M. Hirayama, T. Misawa, T. Ohgoe, Y. Yamaji, M. Imada, Effective Hamiltonian for cuprate superconductors derived from multiscale ab *initio* scheme with level renormalization, Phys. Rev. B **99**, 245155 (2019).

[85] M. Matsumoto, T. Nishimura, Mersenne Twister: A 623-dimensionally equidistributed uniform pseudorandom number generator, ACM Trans. on Modeling and Computer Simulation **8**, 3 (1998).

[86] H. Yokoyama, H. Shiba, Variational Monte-Carlo Studies of Hubbard Model. I, J. Phys. Soc. Jpn. **56**, 1490 (1987).

[87] M. C. Gutzwiller, Effect of Correlation on the Ferromagnetism of Transition Metals, Phys. Rev. Lett. **10**, 159 (1963).

[88] P. Ring, P. Schuck, The Nuclear Many-Body Problem, Springer-Verlag, 1980.

[89] T. Mizusaki, M. Imada, Quantum-number projection in the path-integral renormalization group method, Phys. Rev. B **69**, 125110 (2004).

[90] R. Jastrow, Many-Body Problem with Strong Forces, Phys. Rev. **98**, 1479 (1955).

[91] T. Giamarchi, C. Lhuillier, Phase diagrams of the two-dimensional Hubbard and t-J models by a variational Monte Carlo method, Phys. Rev. B **43**, 12943 (1991).

[92] A. Himeda, M. Ogata, Spontaneous Deformation of the Fermi Surface due to Strong Correlation in the Two-Dimensional t-J Model, Phys. Rev. Lett. **85**, 4345 (2000).

[93] J. P. Bouchaud, A. Georges, C. Lhuillier, Pair wave functions for strongly correlated fermions and their determinantal representation, J. Phys. (Paris) **49**, 553 (1988).

[94] T. A. Kaplan, P. Horsch, P. Fulde, Close Relation between Localized-Electron Magnetism and the Paramagnetic Wave Function of Completely Itinerant Electrons, Phys. Rev. Lett. **49**, 889 (1982).

[95] H. Yokoyama, H. Shiba, Variational Monte-Carlo Studies of Hubbard Model. III. Intersite Correlation Effects, J. Phys. Soc. Jpn. **59**, 3669 (1990).

[96] W. H. Press, S. A. Teukolsky, W. T. Vetterling, B. P. Flannery, NUMERICAL RECIPES in C, Cambridge University Press,, 1993.

[97] K. Ido, T. Ohgoe, M. Imada, Time-dependent many-variable variational Monte Carlo method for nonequilibrium strongly correlated electron systems, Phys. Rev. B **92**, 245106 (2015).

[98] K. Takai, K. Ido, T. Misawa, Y. Yamaji, M. Imada, Finite-Temperature Variational Monte Carlo Method for Strongly Correlated Electron Systems, J. Phys. Soc. Jpn. **85**, 034601 (2016).

[99] M. Casula, C. Attaccalite, S. Sorella, Correlated geminal wave function for molecules: An efficient resonating valence bond approach, J. Chem. Phys. **121**, 7110 (2004).

[100] S. Sorella, M. Casula, D. Rocca, Weak binding between two aromatic rings: Feeling the van der Waals attraction by quantum Monte Carlo methods, J. Chem. Phys. **127**, 014105 (2007).

[101] X. Lin, H. Zhang, A. M. Rappe, Optimization of quantum Monte Carlo wave functions using analytical energy derivatives, J. Chem. Phys. **112**, 2650 (2000).

[102] C. J. Umrigar, C. Filippi, Energy and Variance Optimization of Many-Body Wave Functions, Phys. Rev. Lett. **94**, 150201 (2005).

[103] A. Cayley, Sur les déterminants gauche, J. reine angew. Math. **38**, 93–96 (1849), reprinted in The collected mathematical papers of Arthur Cayley, Cambridge [Eng.] The University Press, Cambridge, vol. 1, pp. 410-413 (1889).

[104] J. Sherman, W. J. Morrison, Adjustment of an inverse matrix corresponding to a change in one element of a given matrix (abstract), Ann. Math. Stat. **20**, 621 (1949).

[105] K. Kuroki, R. Arita, Possible high-T_{c} superconductivity mediated by antiferromagnetic spin fluctuations in systems with Fermi surface pockets, Phys. Rev. B **64**, 024501 (2001).

[106] The $d_{x^2-y^2}$ pairing dominates over the $s^{\pm}$ pairing only for small $t_{\perp}(\leq 0.8t)$ if d-wave states are employed as initial states.

[107] Some notations used in the present study are different from those in ref. [68]. t' and $t'_{\perp}$ in the present study correspond to $-t'$ in ref. [68]. Therefore, in the present study, the antibonding band is the narrow band, whereas in ref. [68], the bonding band is the narrow band. To make the narrow band incipient with band fillings close to half filling, in the present study, band fillings smaller than half-filling are taken to consider cases where the narrow antibonding band lies above the Fermi level in the incipient band situation. On the other hand, in ref. [68], band fillings larger than half-filling were taken so as to make the narrow bonding band lie below the Fermi level. In short, the cases considered here and those in ref. [68] are equivalent and connected by electron-hole transformation. Also, the definition of the band filling is different ; n in the present study corresponds to $n/2$ in ref. [68].

[108] J. E. Han, Spin-triplet s-wave local pairing induced by Hund's rule coupling, Phys. Rev. B **70**, 054513 (2004).

[109] S. Sakai, R. Arita, H. Aoki, Numerical algorithm for the double-orbital Hubbard model: Hund-coupled pairing symmetry in the doped case, Phys. Rev. B **70**, 172504 (2004).

[110] K. Kubo, Pairing symmetry in a two-orbital Hubbard model on a square lattice, Phys. Rev. B **75**, 224509 (2007).

[111] L. de' Medici, S. R. Hassan, M. Caponne, X. Dai, Orbital-Selective Mott Transition out of Band Degeneracy Lifting, Phys. Rev. Lett. **102**, 126401 (2009).

[112] Y. Zhong, Y. Wang, S. Han, Y.-F. Lv, W.-L. Wang, D. Zhang, H. Ding, Y.-M. Zhang, L. Wang, K. He, R. Zhong, J. A. Schneeloch, G.-D. Gu, C.-L. Song, X.-C. Ma, Q.-K. Xue, Nodeless pairing in superconducting copper-oxide monolayer films on $Bi_2Sr_2CaCu_2O_{8+\delta}$, Sci. Bull. **61**, 1239 (2016).

[113] T. H. Geballe, M. Marezio, Enhanced superconductivity in Sr_2CuO_{4-v}, Physica C **469**, 680 (2009).

[114] Q. Q. Liu, H. Yang, X. M. Qin, Y. Yu, L. X. Yang, F. Y. Li, R. C. Yu, C. Q. Jin, S. Uchida, Enhancement of the superconducting critical temperature of $Sr_2CuO_{3+\delta}$ up to 95 K by ordering dopant atoms, Phys. Rev. B **74**, 100506(R) (2006).

[115] Z. Hiroi, M. Takano, M. Azuma, Y. Takeda, A new family of copper oxide superconductors $Sr_{n+1}Cu_nO_{2n+1+\delta}$ stabilized at high pressure, Nature (London) **364**, 315 (1993).

[116] W. M. Li, J. F. Zhao, L. P. Cao, Z. Hu, Q. Z. Huang, X. C. Wang, Y. Liu, G. Q. Zhao, J. Zhang, Q. Q. Liu, R. Z. Yu, Y. W. Long, H. Wu, H. J. Lin, C. T. Chen, Z. Li, Z. Z. Gong, Z. Guguchia, J. S. Kim, G. R. Stewart, Y. J. Uemura, S. Uchida,

C. Q. Jin, Superconductivity in a unique type of copper oxide, Proc. Natl. Acad. Sci. USA **116**, 12156 (2019).

[117] A. M. Olés, K. Wohlfeld, G. Khaliullin, Orbital Symmetry and Orbital Excitations in High-Tc Superconductors, Condens. Matter **4(2)**, 46 (2019).

[118] K. Jiang, X. Wu, J. Hu, Z. Wang, Nodeless High-Tc Superconductivity in the Highly Overdoped CuO2 Monolayer, Phys. Rev. Lett. **121**, 227002 (2018).

[119] T. A. Maier, T. Berlijn, D. J. Scalapino, Two pairing domes as Cu^{2+} varies to Cu^{3+}, Phys. Rev. B **99**, 224515 (2019).

[120] K. Yamazaki, M. Ochi, D. Ogura, K. Kuroki, H. Eisaki, S. Uchida, H. Aoki, Model Construction and Fluctuation Exchange Study of a New Cuprate Superconductor $\mathrm{Ba_2CuO}_{3+\delta}$, in: The 32nd International Symposium on Superconductivity, Miyako Messe, Kyoto, Japan, 2019.

[121] K. Kuroki, H. Usui, S. Onari, R. Arita, H. Aoki, Pnictogen height as a possible switch between high-Tc nodeless and low-Tc nodal pairings in the iron-based superconductors, Phys. Rev. B **79**, 224511 (2009).

[122] S. Graser, T. A. Maier, P. J. Hirschfeld, D. J. Scalapino, Near-degeneracy of several pairing channels in multiorbital models for the Fe pnictides, New J. Phys. **11**, 025016 (2009).

[123] T. A. Maier, S. Graser, D. J. Scalapino, P. J. Hirschfeld, Origin of gap anisotropy in spin fluctuation models of the iron pnictides, Phys. Rev. B **79**, 224510 (2009).

[124] K. Masuda, D. Yamamoto, Formation of Cooper pairs between conduction and localized electrons in heavy-fermion superconductors, Phys. Rev. B **87**, 014516 (2013).

[125] H. Sakakibara, H. Usui, K. Kuroki, R. Arita, H. Aoki, Two-Orbital Model Explains the Higher Transition Temperature of the Single-Layer Hg-Cuprate Superconductor Compared to That of the La-Cuprate Superconductor, Phys. Rev. Lett. **105**, 057003 (2010).

[126] H. Sakakibara, H. Usui, K. Kuroki, R. Arita, H. Aoki, Origin of the material dependence of Tc in the single-layered cuprates, Phys. Rev. B **85**, 064501 (2012).

[127] H. Sakakibara, K. Suzuki, H. Usui, S. Miyao, I. Maruyama, K. Kusakabe, R. Arita, H. Aoki, K. Kuroki, Orbital mixture effect on the Fermi-surface-Tc correlation in the cuprate superconductors: Bilayer vs. single layer, Phys. Rev. B **89**, 224505 (2014).

[128] As the on-site energy is large, the orbital with higher energy level becomes empty. Especially for large U, the empty orbital gives rise to nearly-zero stochastic weights in the MC method because electrons can not move due to U, so that the SR

method becomes unstable. In this way, unfortunately, the VMC method appears not to deal with multi-orbital systems with strong interactions and large on-site energies, where two-orbital systems can be regarded as bilayer and two-leg ladder systems.

Acknowledgments

First and foremost, I would like to express my gratitude to my supervisor, Professor Kazuhiko Kuroki, who provided helpful comments and suggestions throughout my doctoral course. I appreciate Takahiro Misawa and Kota Ido for providing us guidance in the mVMC method. I would like to thank Professor Yasuhiro Akutsu, Professor Keith Slevin, and Professor Mikito Koshino, Professor Jobu Matsuno for being members of my committee. I also thank Masayuki Ochi, Karin Matsumoto, and Daisuke Ogura for fruitful discussions. The numerical calculations were performed at the following institutions; the Supercomputer Center, Institute for Solid State Physics, University of Tokyo and Yukawa Institute Computer Facility, Kyoto University, the Cybermedia Center, Osaka University. Last but not least, I would like to thank my family and friends for giving me constant encouragements and supports.

Achievements

Publications related to the present theis

Submitted

1. Daichi Kato and Kazuhiko Kuroki, “Many-variable variational Monte-Carlo study of superconductivity in two-band Hubbard models with an incipient band”, arXiv:1912.11983

Conference presentations related to the present thesis

International conferences

Poster

1. Daichi Kato and Kazuhiko Kuroki, “Many-variable variational Monte-Carlo studies of superconductivity with incipient bands in two-band Hubbard models”, The 32nd International Symposium on Superconductivity (ISS2019), Kyoto, Japan (2019).

2. Daichi Kato and Kazuhiko Kuroki, “Variational Monte-Carlo Study of the Bilayer Hubbard Model”, The 12th International Conference on Materials and Mechanisms of Superconductivity (M2S2018), Beijing, China (2018).

3. Daichi Kato and Kazuhiko Kuroki, “Variational Monte Carlo analysis on the potential for high Tc superconductivity in the 2-leg Hubbard ladder model”, The

28th International Conference on Low Temperature Physics (LT28), Gothenburg, Sweden (2017).

4. Daichi Kato and Kazuhiko Kuroki, “Variational Monte Carlo study on the possibility of high Tc superconductivity in the 2-leg Hubbard ladder model”, Interdisciplinary Symposium for Up-and-coming Materials Scientists (ISUMS2017), Osaka, Japan (2017).
5. Daichi Kato and Kazuhiko Kuroki, “Potential for high-temperature superconductivity in ladder compounds”, The 2nd International Symposium on Interactive Materials Science Cadet Program (iSIMSC-2), Osaka, Japan (2015).
6. Daichi Kato and Kazuhiko Kuroki, “Multi-Variable Monte-Carlo Study of the Hubbard Ladder Model”, Materials and Mechanisms of Superconductivity (M2S2015), Geneva, Switzerland (2015).

Domestic conferences

Oral

1. 加藤大智, 黒木和彦, “多変数変分モンテカルロ法を用いた二層ハバード模型における超伝導の研究”, 京都大学基礎物理学研究所研究会 “電子相関が生み出す超伝導現象の未解決問題と新しい潮流”, 京都 (2019).
2. 加藤大智, 黒木和彦, “多変数変分モンテカルロ法を用いた梯子系における超伝導の研究”, 第1回 SiMSxCadet 合同シンポジウム, 大阪 (2016).
3. 加藤大智, 黒木和彦, “Variational Monte-Carlo studies of the Hubbard ladder model”, 超伝導ウィンターセミナー SIS2016, 山形 (2016).
4. 加藤大智, 黒木和彦, “Variational Monte Carlo in Hubbard Ladder Model”, 超伝導サマーセミナー SSS2014, 静岡 (2014).

Poster

1. 加藤大智, 黒木和彦, “多変数変分モンテカルロ法を用いた二バンド・ハバード模型における超伝導機構の研究”, 日本物理学会 2019 年秋季大会, 岐阜 (2019).
2. 加藤大智, 黒木和彦, “変分モンテカルロ法による二本鎖型や二層型のハバード模型における超伝導の研究”, 京都大学基礎物理学研究所研究会 “電子相関が生み出す新規な秩序と超伝導現象：トポロジー、液晶状態、動的現象”, 京都 (2018).
3. 加藤大智, 黒木和彦, “梯子型ハバード模型における超伝導の多変数変分モンテカルロ法を用いた解析”, 日本物理学会第 72 回年次大会, 大阪 (2017).
4. 加藤大智, 黒木和彦, “梯子型ハバード模型の多変数変分モンテカルロ法による解析”, 日本物理学会 2016 年秋季大会, 金沢 (2016).

Other publications

Submitted

1. Haruno Kunioka, Kunihiro Kihou, Daichi Kato, Hidetomo Usui, Tsutomu Iida, Hirotaka Nishiate, Kazuhiko Kuroki, Atsushi Yamamoto, and Chul-Ho Lee, "Thermoelectric properties of (Ba,K)Zn_2As_2 crystallized in the $ThCr_2Si_2$-type structure"

Other conference presentations

International conferences

Poster

1. Haruno Kunioka, Kato Daichi, Kunihiro Kihou, Hirotaka Nishiate, Atsushi Yamamoto, Tsutomu Iida, and Chul-Ho Lee, "Thermoelectric properties of $Ba_{1-x}K_xZn_2As_2$ crystallized in the $ThCr_2Si_2$-type structure", 38th International Conference on Thermoelectrics (ICT2019), Gyeongju, South Korea (2019).

2. D. Kato, M. Ochi, K. Kuroki, H. Kunioka, K. Kihou, H. Nishiate, C. H. Lee, "Analysis of the thermoelectric property of $Ba_{1-x}K_xZn_2As_2$ with the $ThCr_2Si_2$-type structure", The 2nd Workshop on Functional Materials Science, Busan, South Korea (2018).

Domestic conferences

Oral

1. 國岡春乃, 木方邦宏, 加藤大智, 西当弘隆, 黒木和彦, 李哲虎, "(Ba,K)Zn_2As_2の熱電特性", 日本物理学会2019年秋季大会, 京都 (2019).

2. 加藤大智, 坂本拓矢, 椋田秀和, 八島光晴, 北岡良雄, 浅野駿, 鈴木謙介, 藤田全基, Y.Krockenberger, 山本秀樹, "Cu-NMRによる銅酸化物Pr_2CuO_4の電子構造測定", 日本物理学会第71回年次大会, 宮城 (2016).

Poster

1. 坂本拓矢, 加藤大智, 椋田秀和, 八島光晴, 北岡良雄, 浅野駿, 鈴木謙介, 藤田全基, Y. Krockenberger, 山本秀樹, "Cu-NMRによる銅酸化物Pr_2CuO_4におけるアニール効果", 日本物理学会2015年秋季大会, 大阪 (2014).

Prize & Internship

1. 大阪大学理学部日本EGF協会奨励賞 (理学部250名中3名受賞).

2. 研修先: KAIST(韓国科学技術院) M. J. Han 研究室, 研修期間: 2018年9-11月, 研究課題名: ラクナスピネル$GaTa_4Se_8$におけるスピンと軌道のもつれた分子基底状態の研究.

3. 研修先: 産業技術総合研究所, つくば中央第二事業所, 省エネルギー部門熱電変換グループ, 研修期間: 2017年6-8月, 研修課題名: 熱電材料開発及び特性評価技術の習得.

4. 研修先: 大阪大学大学院基礎工学研究科物質創成専攻北岡研究室, 研修期間: 2015年4-10月, 研究課題名: Cu-NMRによる銅酸化物Pr_2CuO_4の電子構造測定.